


Summer 2017

High Resolution Spectra of Carbon Monoxide, Propane and Ammonia for Atmospheric Remote Sensing

Christopher Andrew Beale
Old Dominion University

Follow this and additional works at: https://digitalcommons.odu.edu/oeas_etds

 Part of the [Atmospheric Sciences Commons](#), [Physical Chemistry Commons](#), and the [Remote Sensing Commons](#)

Recommended Citation

Beale, Christopher A.. "High Resolution Spectra of Carbon Monoxide, Propane and Ammonia for Atmospheric Remote Sensing" (2017). Doctor of Philosophy (PhD), dissertation, Ocean/Earth/Atmos Sciences, Old Dominion University, DOI: 10.25777/ev91-0796
https://digitalcommons.odu.edu/oeas_etds/7

This Dissertation is brought to you for free and open access by the Ocean, Earth & Atmospheric Sciences at ODU Digital Commons. It has been accepted for inclusion in OEAS Theses and Dissertations by an authorized administrator of ODU Digital Commons. For more information, please contact digitalcommons@odu.edu.

HIGH RESOLUTION SPECTRA OF CARBON MONOXIDE, PROPANE AND

AMMONIA FOR ATMOSPHERIC REMOTE SENSING

By

Christopher Andrew Beale

B.Sc. July 2010, University of York, UK

M.Sc. July 2012, University of York, UK

A Dissertation Submitted to the Faculty of
Old Dominion University in Partial Fulfillment of the
Requirements for the Degree of

DOCTOR OF PHILOSOPHY

OCEANOGRAPHY

OLD DOMINION UNIVERSITY
August 2017

Approved by:

Peter F. Bernath (Director)

John Klinck (Member)

Charles I. Sukenik (Member)

ABSTRACT

HIGH RESOLUTION SPECTRA OF CARBON MONOXIDE, PROPANE AND AMMONIA FOR ATMOSPHERIC REMOTE SENSING

Christopher Andrew Beale
Old Dominion University, 2017
Director: Dr. Peter F. Bernath

Spectroscopy is a critical tool for analyzing atmospheric data. Identification of atmospheric parameters such as temperature, pressure and the existence and concentrations of constituent gases via remote sensing techniques are only possible with spectroscopic data. These form the basis of model atmospheres which may be compared to observations to determine such parameters. To this end, this dissertation explores the spectroscopy of three molecules: ammonia, propane and carbon monoxide.

Infrared spectra have been recorded for ammonia in the region $2400\text{-}9000\text{ cm}^{-1}$. These spectra were recorded at elevated temperatures (from $293\text{-}973\text{ K}$) using a Fourier Transform Spectrometer (FTS). Comparison between the spectra recorded at different temperatures yielded experimental lower state energies. These spectra resulted in the measurement of roughly 30000 lines and about 3000 quantum assignments. In addition spectra of propane were recorded at elevated temperatures ($296\text{-}700\text{ K}$) using an FTS. Atmospheres with high temperatures require molecular data at appropriate conditions. This dissertation describes collection of such data and the potential application to atmospheres in our solar system, such as auroral regions in Jupiter, to

those of planets orbiting around other stars and cool sub-stellar objects known as brown dwarfs. The spectra of propane and ammonia provide the highest resolution and most complete experimental study of these gases in their respective spectral regions at elevated temperatures. Detection of ammonia in an exoplanet or detection of propane in the atmosphere of Jupiter will most likely rely on the work presented here.

The best laboratory that we have to study atmospheres is our own planet. The same techniques that are applied to these alien atmospheres originated on Earth. As such it is appropriate to discuss remote sensing of our own atmosphere. This idea is explored through analysis of spectroscopic data recorded by an FTS on the Atmospheric Chemistry Experiment satellite of carbon monoxide. The effect of the atmosphere's chemistry and physics on this molecule is measured through its isotopologues, primarily ^{13}CO (carbon-13 substituted carbon monoxide). Isotopic chemistry allows a key analysis of the atmosphere as it may be used as a tracer for chemical reactions and dynamical processes. The carbon monoxide fractionation results in Chapter IV present the first global measurements of isotopic fractionation of CO, showing significant fractionation in the upper atmosphere (60-80 km) as a result of the photolysis of carbon dioxide (CO_2).

For my family

ACKNOWLEDGEMENTS

My journey through graduate school has not been a short one. Throughout the seven years from starting my M.Sc. at York to finishing my Ph.D. at Old Dominion University I have been indebted to my advisor, Professor Peter Bernath. My development as a scientist is primarily due to being part of the Bernath group. It has been a privilege to be a part of a diverse and entertaining team!

Many of the methods used for my research were first developed by Dr. Robert Hargreaves and having him in the group helped my professional progression. For much of the ACE research, the constant back and forth between Eric Buzan and me helped me immensely and I hope this was reciprocated! Other members of the group who deserve thanks are Mike Dulick for organizing the lab and making things run smoothly, the postdocs who have come and gone during my time here, Drs. Dan Frohman, Andy Wong, Jamie Hodges and Dror Bittner. Even though my research and that of other students in the group may have not always overlapped, I'm thankful to have had Anton Fernando and Mehdi Yousefi as well as Eric for making the group a great place to work. I also thank Professor Hans-Peter Plag for the significant edits suggested after the first draft.

For life outside of work and study I thank all of the graduate students in the Ocean. Earth and Atmospheric Sciences Department, especially Bonnie, Will, Malee and Brittany as well as Rob, Andy and Dan from the group for their friendship and for enabling me to take some well needed time from the office. I am immensely grateful to the Torrillo family for being a real home away from home, being so far away from my own family was never easy and to be extended the kind of love and care that I was means a great deal to me and certainly made this journey of mine possible.

As for my own family, I cannot express my gratitude easily. As difficult as my time at ODU has been for me, my family have always been there for me, in every capacity possible. For family members lost and for those gained, I dedicate this dissertation to you.

TABLE OF CONTENTS

| | Page |
|--|------|
| LIST OF TABLES | x |
| LIST OF FIGURES | xii |
| Chapter | |
| I. INTRODUCTION | 1 |
| II. ATMOSPHERIC CHEMISTRY BACKGROUND | 4 |
| VERTICAL STRUCTURE OF THE ATMOSPHERE | 4 |
| COMPOSITION OF THE ATMOSPHERE | 6 |
| METHODS OF ATMOSPHERIC MEASUREMENT | 7 |
| SATELLITE REMOTE SENSING | 7 |
| THE ATMOSPHERIC CHEMISTRY EXPERIMENT | 8 |
| ATMOSPHERIC MODELS | 11 |
| ASTRONOMICAL ATMOSPHERES | 12 |
| SOLAR SYSTEM PLANETS | 13 |
| BROWN DWARFS | 14 |
| EXOPLANET ATMOSPHERES | 18 |
| III. SPECTROSCOPY BACKGROUND | 21 |
| INTRODUCTION | 21 |
| ROTATIONAL SPECTROSCOPY | 22 |
| VIBRATIONAL SPECTROSCOPY | 24 |
| FUNDAMENTAL, OVERTONE, HOT BAND AND COMBINATION TRANSITIONS | 25 |
| SELECTION RULES | 27 |
| SPECTRAL LINESHAPE | 29 |
| LINELISTS | 31 |

| | Page |
|---|------|
| FOURIER TRANSFORM SPECTROSCOPY..... | 32 |
| IV. ISOTOPIC FRACTIONATION OF CARBON MONOXIDE | 41 |
| INTRODUCTION | 41 |
| EXPERIMENTAL..... | 45 |
| ISOTOPIC EFFECTS ON INFRARED SPECTRA..... | 52 |
| WACCM..... | 55 |
| RESULTS FOR ^{13}CO | 58 |
| ISOTOPIC FRACTIONATION OF C^{17}O AND C^{18}O | 65 |
| CONCLUSION..... | 69 |
| V. PROPANE CROSS-SECTIONS IN THE 3 μm REGION..... | 70 |
| INTRODUCTION | 70 |
| SPECTROSCOPY OF PROPANE..... | 73 |
| EXPERIMENTAL..... | 77 |
| RESULTS | 79 |
| DISCUSSION | 83 |
| CONCLUSION..... | 85 |
| VI. INFRARED SPECTRA OF AMMONIA..... | 86 |
| INTRODUCTION | 87 |
| AMMONIA IN BROWN DWARFS..... | 87 |
| AMMONIA IN EXOPLANETS..... | 89 |
| SPECTROSCOPY OF AMMONIA..... | 91 |
| EXPERIMENTAL..... | 94 |

| | Page |
|--|------|
| TRANSMISSION SPECTRA OF NH ₃ IN THE 2400-5500 CM ⁻¹ REGION | 96 |
| FREQUENCY CALIBRATION | 98 |
| INTENSITY CALIBRATION..... | 98 |
| EFFECT OF TEMPERATURE ON INTENSITY | 100 |
| RESULTS FOR LOW FREQUENCY REGION | 102 |
| LOWER STATE ENERGIES..... | 109 |
| TRANSMISSION SPECTRA OF NH ₃ IN THE 4800-9000 CM ⁻¹ REGION | 112 |
| EXPERIMENTAL..... | 113 |
| RESULTS FOR HIGH FREQUENCY REGION | 116 |
| CONCLUSION..... | 120 |
| | |
| VII. CONCLUSIONS AND FURTHER WORK | 122 |
| | |
| VIII. REFERENCES | 125 |
| | |
| IX. VITA..... | 144 |

LIST OF TABLES

| Table | Page |
|--|------|
| 1. Stellar classifications based on color, temperature and mass. | 15 |
| 2. Estimates of sources and sinks of carbon monoxide | 42 |
| 3. List of microwindows used for ^{12}CO retrievals (ACE-FTS version 3.5 data product)..... | 49 |
| 4. List of microwindows used for ^{13}CO retrievals (ACE-FTS version 3.5 data product) | 51 |
| 5. Vibrational band centers of ^{12}CO and ^{13}CO | 53 |
| 6. The fractionation effects of the four main tropospheric CO sources | 55 |
| 7. List of major reactions for CO in the atmosphere with their related kinetic isotope effects k_{12}/k_{13} | 56 |
| 8. Summary of C^{17}O and C^{18}O abundance and retrieval ranges..... | 66 |
| 9. The 27 fundamental modes of propane..... | 74 |
| 10. Experimental conditions and setup of the Bruker IFS 125 HR | 78 |
| 11. Propane integrated cross-section calibration | 79 |
| 12. Summary of the fundamental modes of ammonia | 92 |
| 13. Experimental conditions for NH_3 low wavenumber region..... | 97 |
| 14. Total number lines, the number of added lines, partition functions and tentative assignments made via comparison with each line list at each temperature..... | 97 |

| Table | Page |
|---|------|
| 15. Linear calibration factors for experimental line positions and intensities for each temperature in the low wavenumber region..... | 100 |
| 16. Partition function for NH ₃ (low wavenumber range) | 101 |
| 17. Experimental conditions for NH ₃ high wavenumber region | 113 |
| 18. Partition function for NH ₃ (high wavenumber range) | 115 |
| 19. Calibration factors for experimental line positions and intensities for each temperature and pressure in the high wavenumber region | 116 |

LIST OF FIGURES

| Figure | Page |
|--|------|
| 1. Mean pressure (red) and temperature (black) profiles of the atmosphere. | 5 |
| 2. Composition of the atmosphere at the Earth's surface. | 6 |
| 3. Two main geometries of passive satellite remote sensing of the Earth's atmosphere..... | 8 |
| 4. Solar occultation measurements through different atmospheric layers | 9 |
| 5. The ACE satellite..... | 10 |
| 6. A sample of the ACE-FTS spectrum with HCl and CH ₄ lines in the stratosphere and lower mesosphere..... | 11 |
| 7. The Hertzsprung-Russell diagram | 16 |
| 8. Near-infrared spectra of three cool M-class stars and two hot L-dwarfs..... | 17 |
| 9. Spectra of L- and T-dwarfs compared to those of Jupiter and an M-class star | 18 |
| 10. The transit method of exoplanet detection..... | 19 |
| 11. Two dimensional representation of the harmonic and Morse oscillators | 25 |
| 12. Energy level diagram showing fundamental (1-0), overtone (2-0, 3-0, 4-0) and hot band (2-1, 3-1, 4-1) transitions..... | 27 |
| 13. Schematic of P, Q and R transitions. | 28 |
| 14. Transmission spectra of ammonia at both 10 Torr (red) and 100 Torr..... | 30 |
| 15. Gaussian (black), Lorentzian (blue) and Voigt (green) lineshapes..... | 31 |

| Figure | Page |
|--|------|
| 16. Layout of a Michelson interferometer, the fundamental component of a Fourier transform spectrometer | 33 |
| 17. Schematic of the tube furnace used as a source | 35 |
| 18. Schematic of the Bruker IFS 125HR FTS with labels of main components | 36 |
| 19. Photograph of the tube furnace (on the right with exhaust hood over it) and the Bruker IFS 125HR FTS (center) in the Bernath laboratory at ODU | 37 |
| 20. Water line removal, the sample is shown in the blue trace, initial water removal in red and the cut spectrum in gray | 38 |
| 21. The sample spectrum includes signal from the sample (NH ₃) and other gases, mainly water in the air gap between the furnace and the spectrometer | 39 |
| 22. Global distribution of carbon monoxide by season as measured by the ACE-FTS | 44 |
| 23. Locations of 25855 ACE-FTS occultations between March 2004 and October 2010 | 47 |
| 24. Latitudinal coverage of SCISAT for one year | 48 |
| 25. The vibrational mode for carbon monoxide | 53 |
| 26. Seasonal variation of $\delta^{13}\text{CO}$ as a function of latitude between 8 and 90 km from the ACE-FTS..... | 60 |
| 27. Seasonal variation of $\delta^{13}\text{CO}$ as a function of latitude between 0 and 90 km from WACCM | 62 |
| 28. Difference between ACE measurements of $\delta^{13}\text{CO}$ and WACCM output | 63 |
| 29. Total CO concentrations from 6-30 km as measure by the ACE-FTS | 65 |

| Figure | Page |
|---|------|
| 30. Isotopic fractionation of C ¹⁷ O from 9-25 km. | 67 |
| 31. Isotopic fractionation of C ¹⁸ O from 6-30 km. | 68 |
| 32. Detection of propene (unlabeled peak at 912.5 cm ⁻¹ in left panel) in Titan | 72 |
| 33. Stick and ball figure of propane..... | 75 |
| 34. Comparison of high resolution spectra of propene (C ₃ H ₈) at high resolution (0.005 cm ⁻¹ , blue trace) and medium resolution (0.08 cm ⁻¹ , orange trace) | 76 |
| 35. Cross-sections (0.005 cm ⁻¹ resolution) for increasing temperatures in the range 2700-3100 cm ⁻¹ | 80 |
| 36. A more detailed view of each spectrum (2971.5-2974.5 cm ⁻¹) where the strong features are seen to weaken with increasing temperature. | 81 |
| 37. A more detailed view of the ν ₃ and ν ₁₆ modes centered at 2887 cm ⁻¹ | 82 |
| 38. Spectra of 5 different T dwarfs | 87 |
| 39. Bottom: opacity calculations for NH ₃ , CH ₄ and H ₂ O at 600 K. Top: H-band spectra of several T-type dwarfs | 89 |
| 40. Calculation of cross-sections of a number of molecules predicted to exist in exoplanetary atmospheres..... | 90 |
| 41 Energy level diagram of ammonia demonstrating the inversion doubling of the energy levels of ammonia | 94 |
| 42. Intensity calibration plot for 500 K at 10 Torr for the higher wavenumber region | 99 |

| Figure | Page |
|---|------|
| 43. Overview of spectra of NH ₃ showing experimental data (top panel) and simulated spectra created to match the conditions of the experiment from the BYTe (center panel) and HITRAN (lower panel) line lists at 296 K..... | 105 |
| 44. Overview of spectra of NH ₃ showing experimental data (top panel) and simulated spectra created to match the conditions of the experiment from the BYTe (center panel) and HITRAN (lower panel) line lists at 773 K..... | 106 |
| 45. Detailed spectra of NH ₃ showing experimental data (top panel) and simulated spectra created to match the conditions of the experiment from the BYTe (center panel) and HITRAN (lower panel) line lists at 296 K..... | 107 |
| 46. Detailed spectra of NH ₃ showing experimental data (top panel) and simulated spectra created to match the conditions of the experiment from the BYTe (center panel) and HITRAN (lower panel) line lists at 773 K..... | 108 |
| 47. Comparison of lower state energies from the HITRAN line list (top panel) and from the experimental line list (lower panel) as a function of line position..... | 111 |
| 48. Comparison of matched lower state energies obtained from experiment (x-axis) and the HITRAN re-analysis of Down <i>et al.</i> (y-axis)..... | 112 |
| 49. Transmission spectrum of 100 Torr of NH ₃ at 700 K in the high wavenumber region..... | 114 |
| 50. Spectrum of NH ₃ at a temperature of 293 K and pressure of 10 Torr | 117 |
| 51. Comparison of calibrated intensities from both pressures and a 1:1 trend line | 118 |

| Figure | Page |
|--|------|
| 52. Lower state energy plot of the high wavenumber region (lower) as compared to HITRAN (upper)..... | 119 |

CHAPTER I

INTRODUCTION

The complexity of the Earth system cannot be overstated. Humans have always had an influence on the planet; however, in recent history, with the advent of industrialization and huge population growth, the effect of humans on the planet has increased dramatically (*Steffen et al., 2007*). The effects of human activity are now being felt across the planet with increased extreme weather, sea level rise, changes in wildlife patterns and human health problems (*Hansen, 1998*). The constant changes in the environment are now accelerating and understanding the environment in which we live is important for mitigating the effects of global and localized climate change.

The interaction between the atmosphere and oceans is significant. For example, higher carbon dioxide concentrations in the atmosphere lead to a change in the carbon chemistry of the oceans, making them more acidic (*Sabine et al., 2004*). This affects the biota of the oceans (*Hughes et al., 2003*). Indeed the effect of the oceans on the atmosphere is just as significant in that much of the oxygen in the atmosphere comes from oceanic plankton (*Falkowski and Oliver, 2007*). The changing biodiversity of the oceans has a direct effect on our atmosphere.

The understanding of the origins of the Earth is also important. The origins of planet Earth and the Solar System as a whole are unknown. Previous explanations of planetary formation have been called into question with the discovery of other planetary systems that do not conform to the models of Solar System formation (*Ida and Lin, 2005*). Studies of planets outside of our Solar System, known as extrasolar planets or exoplanets, help us to explain the origins of planet Earth.

Equally, the Earth provides an excellent laboratory with which planetary physics and chemistry in general and the potential existence of life on other planets can be better understood.

Measurements of the atmosphere are important because of its constantly changing composition. Sources of atmospheric gas vary in both space and time as do the physical effects in the atmosphere which lead to the transport of air masses. Laboratory studies of the constituent gases in the atmosphere allow better determination of the concentrations of individual species. Measurement of a spectrum provides a chemical signature of the molecule in question which may be compared to observations. The concentration of a gas in the atmosphere determines the amount of absorption or emission of the lines recorded in the observed spectrum. The technique of infrared spectroscopy (detailed in Chapter III) is frequently used in satellite measurements of the atmosphere. Atmospheric spectra are complex and higher resolution laboratory measurements at appropriate conditions (temperature and pressure) allow more precise quantification of atmospheric constituents.

Chapter II provides an introduction to atmospheric chemistry and detection techniques for determining the atmospheric conditions of Earth and astronomical objects. Chapter III discusses the basic spectroscopic theory used to measure the spectra recorded in this dissertation. The infrared region of the spectrum is generally used to measure vibration-rotation transitions of molecules. Electronic spectroscopy will not be discussed. Importantly, the effect of temperature on a spectrum is discussed.

Chapter IV describes results from the first global measurements of isotopic fractionation of carbon monoxide (CO). The ACE-FTS (Atmospheric Chemistry Experiment-FTS) satellite instrument was used to record spectra (analyzed by Chris Boone at the University of Waterloo) of the atmosphere from 2004-2012. Following retrieval, ACE data are available as volume mixing ratios

of gases and other atmospheric parameters. These were used by me to measure fractionation effects of CO and compared to a comprehensive numerical model (model results obtained from Eric Buzan at Old Dominion University). The results and much of the text and figures from this chapter have been previously published in *Beale et al.* (2016a).

Chapter V discusses the measurement of the spectrum of propane (C_3H_8) in the 3000 cm^{-1} region at high temperatures. These elevated temperatures are appropriate for measuring C_3H_8 in auroral regions of Jupiter and exoplanets. As the spectrum of propane is complex, many of the individual lines ‘blend’ in to each other. As a result the spectrum is presented as an infrared absorption cross-section which is the amount of absorption of all constituent lines at a given frequency. The results and much of the text and figures from this chapter have been previously published in *Beale et al.* (2016b).

Chapter VI presents high resolution spectra of ammonia (NH_3) in the $2500\text{-}9000\text{ cm}^{-1}$ region at elevated temperatures suitable for characterization of exoplanets and brown dwarfs. Also presented are lower state energies as calculated from experimental lines. The lower state energy of a line allows extrapolation of observed absorption for a particular line with temperature. As such, with the line positions, intensities and lower state energies provided as a result of this work, spectra can be predicted outside of the temperature range measured. For one region of the NH_3 spectra recorded ($2500\text{-}5500\text{ cm}^{-1}$), the experimental linelist was compared to lines from other NH_3 linelists containing quantum number assignments. This allows some of the lines measured to be matched and given a full quantum mechanical description. The results and much of the text and figures from this chapter have been previously published in *Beale et al.* (2017).

Chapter VII presents the overall conclusions and future work from this dissertation.

CHAPTER II

ATMOSPHERIC CHEMISTRY BACKGROUND

VERTICAL STRUCTURE OF THE ATMOSPHERE

The Earth's atmosphere is made up of four layers: the troposphere, the stratosphere, the mesosphere and the thermosphere, the boundaries of which are defined by the change of temperature with altitude. The typical vertical profiles of both the temperature and pressure of the atmosphere up to 80 km are shown in Figure 1.

The troposphere is the bottom layer of the atmosphere, ranging from the surface of the Earth up to approximately 8-18 km, and is characterized by decreasing temperature with increasing altitude caused by adiabatic cooling of air as the pressure decreases. The variation in the altitude of the troposphere-stratosphere boundary, known as the tropopause, is dependent on the latitude, with the troposphere being thinnest at the poles and thickest at the Equator, and also the season, being higher in the warmer months and lower in the cooler months. The chemical distribution of the troposphere is relatively consistent for long-lived molecules as it is well mixed (*Ehhalt, 1999*) and despite being the thinnest layer of the atmosphere, the troposphere contains 75-80% of the total atmospheric mass (*Charlson et al., 1992*).

The stratosphere extends from the tropopause to around 50 km and is marked by increasing temperature with altitude, caused by absorption of UV radiation by ozone. Increasing temperature with altitude reduces vertical mixing in this layer, resulting in the stratification of this part of the atmosphere. When the density of ozone is no longer high enough to absorb enough energy to heat

the atmosphere, the temperature once again begins to decrease with altitude. This point is known as the stratopause and marks the start of the mesosphere which extends up to approximately 80 km where absorption of solar energy by nitrogen and oxygen again cause increase in atmospheric temperature; this layer is known as the thermosphere.

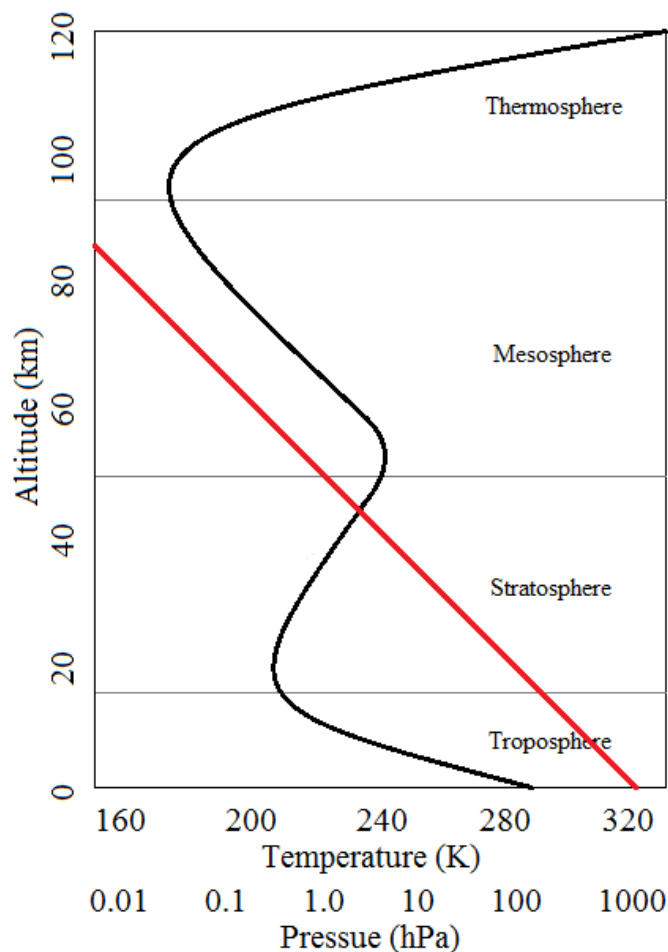


Figure 1. Mean pressure (red) and temperature (black) profiles of the atmosphere. Adapted from *Jacob (1999)*.

The mesosphere and thermosphere contain, on average, the coldest and hottest parts of the atmosphere respectively.

COMPOSITION OF THE ATMOSPHERE

Figure 1 shows how the pressure of the atmosphere decreases with altitude. The amount of various gases in the atmosphere are frequently given as volume mixing ratios (VMR) which relates the number density of a particular gas to the number density of the atmosphere at a particular altitude. The major constituents of the dry atmosphere (Figure 2) are nitrogen (78%), oxygen (21%) and argon (1%). Of the remaining fraction of one percent, carbon dioxide is notable as its VMR is increasing due to anthropogenic emissions, from pre-industrial levels of 280 ppm (parts per million) (*Etheridge et al.*, 1996) to a year-long average of over 400.9 ppm for the first time in 2015 (*Betts et al.*, 2016). These surface averages differ through the vertical column due to chemical reactions, dynamics and photolytic reactions from solar radiation.

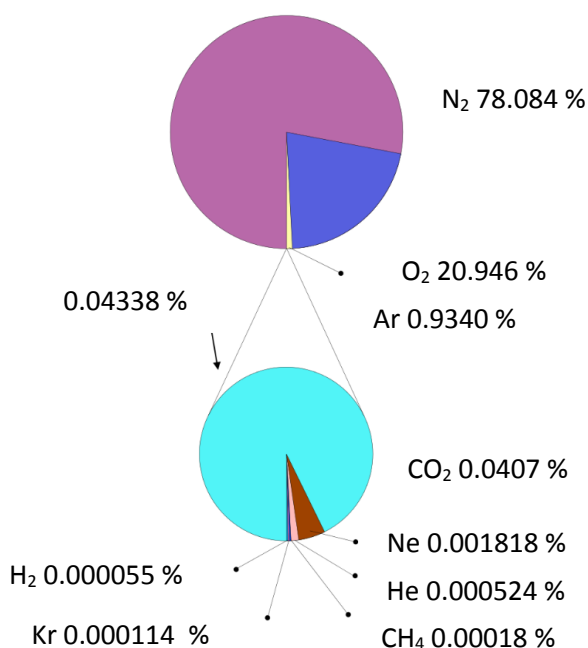


Figure 2. Composition of the dry atmosphere at the Earth's surface. The upper chart represents the major constituents. The lower chart represents the trace gases with the highest concentrations. Figure adapted from https://commons.wikimedia.org/wiki/File:Atmosphere_gas_proportions.svg, accessed June 15 2017.

METHODS OF ATMOSPHERIC MEASUREMENT

Measurement of the chemical composition of the atmosphere can be accomplished in two ways: *in situ* and via remote sensing. *In situ* measurement requires collection of a sample, which may be ground based (*Kato et al.*, 2000), from a balloon (*Lämmerzahl et al.*, 2002), an aircraft (*Thiemens et al.*, 1995a) or a rocket (*Thiemens et al.*, 1995b). The sample is then measured, either at the point of collection or in a laboratory, usually with a mass spectrometer. Remote sensing platforms can be ground based, airborne or via satellite. Ground based remote sensing platforms are relatively cheap, although they give limited spatial coverage as the measurement is restricted to the geographic location of the instrument. Airborne platforms can more easily resolve vertical differences in atmospheric composition, but are less stable than either ground based or satellite measurements. Satellite remote sensing offers much broader coverage of the globe, on a very stable platform, although the costs of such missions are much higher than other methods and repairs to space-borne instruments are often not possible.

SATELLITE REMOTE SENSING

There are two main geometries of remote sensing from satellites: nadir and limb views. Nadir observations measure radiation emitted from the surface of the Earth and the atmosphere itself. In the limb geometry, the line of sight views across the edge of the atmosphere (Figure 3). Nadir measurements generally provide better horizontal resolution than limb measurements whereas limb view measurements generally have better vertical resolution and have a higher sensitivity to trace species as this view has a longer path length through the atmosphere.

A type of limb viewing technique, known as solar occultation, uses the Sun as a light source, allowing absorption measurements to be made whenever the geometry allows, i.e. the Sun, atmosphere and instrument are aligned (Figure 4). Using the Sun as a source provides high signal to noise ratios and as the satellite moves in its orbit, the geometry changes and allows measurement through the atmosphere, giving the high vertical resolution of this measurement type.

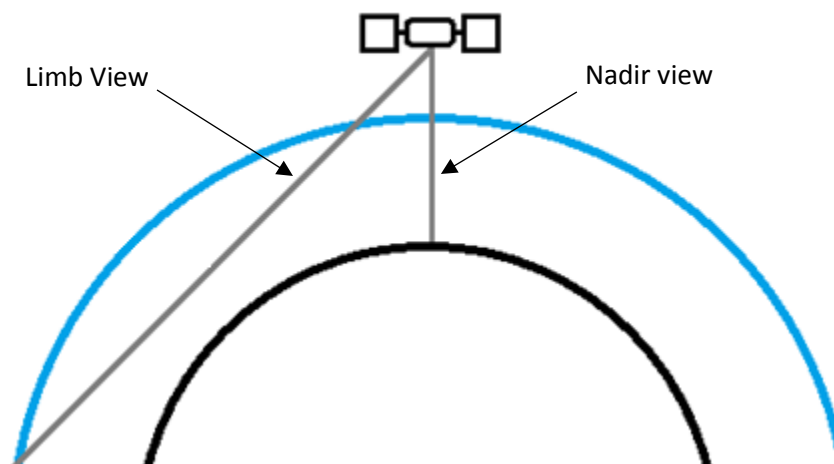


Figure 3. Two main geometries of passive satellite remote sensing of the Earth's atmosphere. Nadir-viewing instruments measure radiation emitted from the surface of the Earth while the limb viewing instruments measure radiation emitted from the limb of the atmosphere.

THE ATMOSPHERIC CHEMISTRY EXPERIMENT

The Atmospheric Chemistry Experiment (ACE) is a Canadian scientific satellite which was launched in August 2003. The satellite has two instruments, the ACE-FTS and MAESTRO. MAESTRO is a UV-visible spectrophotometer, which shall not be discussed here for the sake of brevity. The primary instrument is the ACE-FTS: a high-resolution Fourier Transform Spectrometer (FTS), designed to study the chemical and physical processes that affect the

distribution of ozone in the stratosphere above the Arctic (Bernath *et al.*, 2005). The 74° orbital inclination of the satellite allows near global coverage (85° S to 85° N) providing the capability to study processes in the tropical, subtropical, mid-latitude and polar regions of Earth.

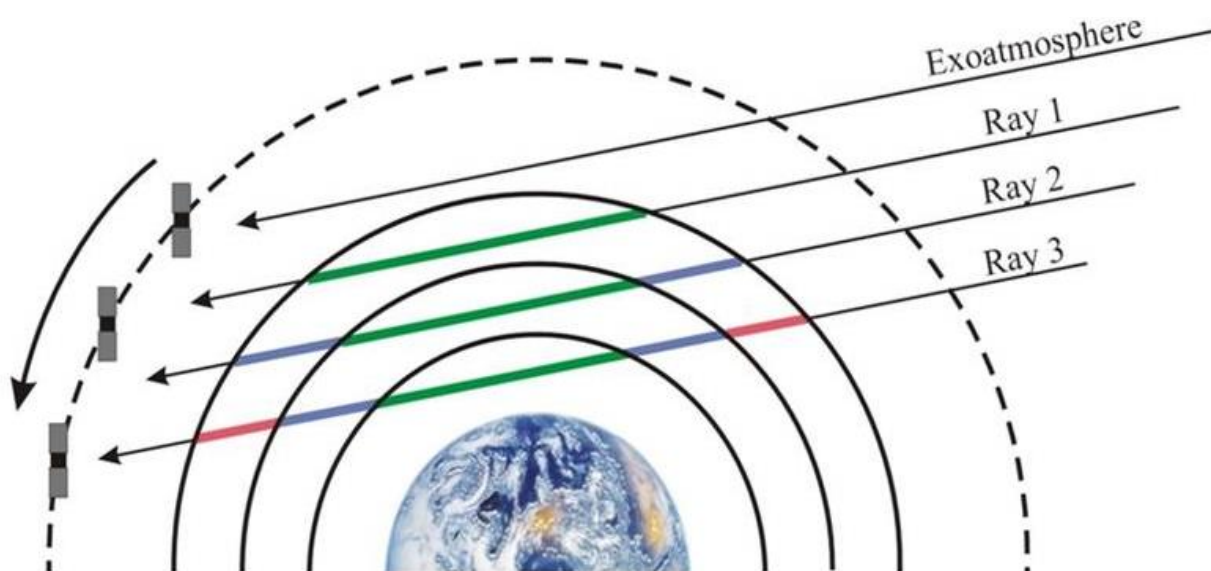


Figure 4. Solar occultation measurements through different atmospheric layers. Figure courtesy of Randall Skelton.

The ACE-FTS instrument (Figure 5) was built by ABB-Bomem and operates in the infrared, in the region ($750\text{--}4400\text{ cm}^{-1}$) at high resolution (0.02 cm^{-1}). Measurements of the vertical profiles of Earth's atmosphere are achieved using the solar occultation technique. The limb view through the exoatmosphere (Figure 4) measures solar radiation without atmospheric attenuation. As the viewing geometry changes and the atmosphere begins to be in the line of sight of the satellite, the chemicals in the atmosphere absorb radiation and attenuate the signal. Measurement of the solar

spectrum through the different layers of the atmosphere gives the chemical composition of the atmosphere as a function of altitude.

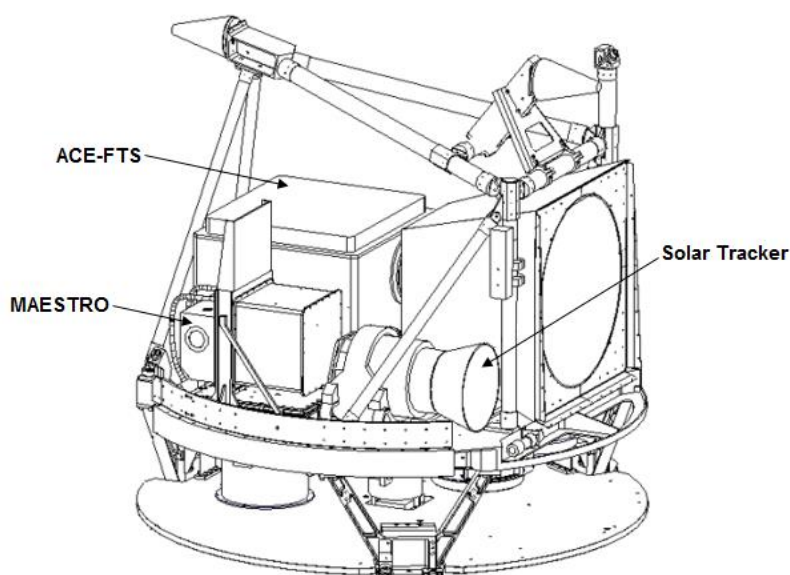


Figure 5. The ACE satellite. Adapted from a schematic from Bristol Aerospace (*Walkty and Kohut, 2013*).

Spectra (Figure 6) are compared to a model of an atmospheric spectrum with certain concentrations. The forward model parameters are then changed until the spectra match. The retrievals of the concentrations of gases in the atmosphere from ACE observations were performed by Chris Boone at the Science Operations Center at the University of Waterloo in Canada. The list of volume mixing ratios (VMRs) of each molecule as a function of altitude are provided by Boone as the ACE data product. These data can then be analyzed by the end user. All retrieval of ACE-FTS data in this dissertation (and for most end users) was performed by Boone. ACE data are validated by comparison to available *in situ* or remote sensing measurements. Validation has been

achieved for total CO (Clerbaux *et al.*, 2008); however, no validation exists for the minor isotopologues of CO.

ATMOSPHERIC MODELS

Each of the measurement techniques described above have limitations. *In situ* measurements suffer from a lack of spatial or temporal coverage and satellite remote sensing measurements lack precision and accuracy for single measurements. Atmospheric chemical models can be used to predict the chemical composition of the atmosphere at any given location. The accuracy of such predictions is restricted only by the completeness of the chemical model and the boundary conditions used to create it.

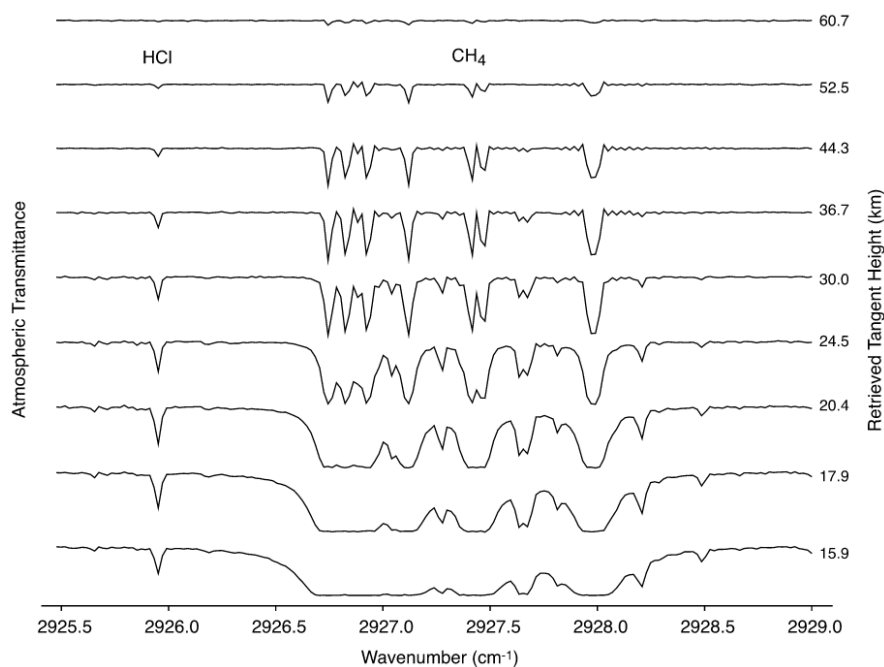


Figure 6. A sample of the ACE-FTS spectrum with HCl and CH₄ lines in the stratosphere and lower mesosphere (Bernath *et al.* 2005).

The Whole Atmosphere Community Climate Model (WACCM) is a component of the Community Earth System Model, primarily developed by the National Center for Atmospheric Research (*Marsh et al.*, 2013). WACCM analysis for comparison to ACE data for this research was performed by Eric Buzan (Department of Chemistry & Biochemistry, Old Dominion University). WACCM uses 66 vertical levels up to 140 km and a horizontal grid of 4° latitude by 5° longitude. This grid spacing is sufficient for comparison with the 10° latitudinal bins of the observed satellite results. There is no native support for isotopologues in WACCM, although equations for particular reactions can be added with the rate constants that control the speed of reactions for different isotopologues added. Comparison between the model and observational results may be used to improve each other. Differences may be due to errors in the retrieval process or as a result of chemical reactions or dynamics not included in the model. For example, the comparison of ^{13}CO discussed in Chapter IV shows the need for improved hydrocarbon isotopic chemistry in the stratosphere of the WACCM model. Differences between the model and observations may also show errors in the retrieval process which can then be improved.

ASTRONOMICAL ATMOSPHERES

Many of the techniques used to study the Earth's atmosphere may be similarly applied to astronomical objects. Interstellar space is continually enriched by atoms and molecules expelled by stellar explosions. The regions in which material has been ejected from stars are higher in density than the interstellar medium and this increases the probability of collisions leading to the creation of more complex molecules and perhaps, even planets. The study of molecules in the interstellar medium is known as astrochemistry and this field has discovered 194 different

molecules in the interstellar medium or the circumstellar shells of stars (as of October 2015) and 61 different molecules have been detected from sources outside of the Milky Way galaxy (<https://www.astro.uni-koeln.de/cdms/molecules>, accessed July 8th, 2017).

The study of astronomical molecules in planetary and stellar atmospheres is usually considered a separate field from astrochemistry. The low temperatures of the interstellar medium allow complex molecules to form, whereas the much higher temperatures of stellar atmospheres usually result in very simple molecules forming. In 1995, the discovery of the first brown dwarf (*Rebolo et al.*, 1995) and exoplanet (*Mayor and Queloz*, 1995) were the first in an ensuing large number of atmospheres outside of our Solar System with temperatures cool enough for the detection of molecules which would otherwise be dissociated in the hot atmospheres of stars.

SOLAR SYSTEM PLANETS

The planets in the solar system have a wide variety of atmospheres. Mercury, being so close to the Sun has almost no atmosphere (*Kabin et al.*, 2000). In comparison, Venus has a very thick atmosphere (*Lebonnois et al.*, 2010) of mostly carbon dioxide and sulfuric acid clouds (*Kolodner and Steffes*, 1998). Earth's atmosphere is mostly molecular oxygen and nitrogen (Figure 2) and Mars has a very thin carbon dioxide atmosphere (*Nier and McElroy*, 1977). The outer planets, Jupiter, Saturn, Uranus and Neptune are known as giant planets which make up most of the mass of the solar system outside of the Sun. The smallest, Uranus, has a mass of 15 times that of the Earth (*Thommes et al.*, 2002). The atmospheres of the outer planets are dominated by hydrogen and helium, but they also contain appreciable amounts of water, ammonia, methane and other hydrocarbons (*Weidenschilling and Lewis*, 1973; *Strobel*, 1975).

The atmospheres of the gas giants are generally cool compared to that of Earth; however, there are wide temperature variations within the different atmospheric layers. The auroral regions (areas of light emission caused by charged particles generally at high altitudes near the magnetic poles) of Jupiter, for example, can reach temperatures of up to 1000 K. In such regions, strong hydrocarbon emissions have been detected and models predict the possibility of a wider variety of hydrocarbons (*Kim et al.*, 2009).

BROWN DWARFS

Brown dwarfs are sub-stellar objects defined by their inability to fuse hydrogen in their cores. However both deuterium and lithium may be fused (*Burrows et al.*, 2001). As such, they emit almost no visible light, although they may be detected in the infrared. These objects range in size from 13 to around 90 Jupiter masses; this upper limit being roughly 0.08 Solar masses.

Brown dwarfs are similarly characterized with the L, T and Y dwarfs representing objects in three approximate temperature ranges. L-type dwarfs are the hottest of the brown dwarfs and have surface temperatures of 1300-2400 K. In addition to temperature ranges, brown dwarfs are characterized by the molecules present in their atmospheres. Figure 8 shows the near-IR spectra of three cool M-class stars and two hot L-class dwarfs. The M-class stars have noticeable titanium oxide (TiO) and vanadium oxide (VO) features which are not present in the L-dwarfs; however, the strength of the metal hydride (FeH and CrH) features increase in the L-dwarfs.

Cooler than the L-dwarf stars are the T dwarfs, having an approximate temperature range of 700-1300 K. The main spectral feature of this class is methane absorption (Figure 9), hence the nickname for this class of ‘methane dwarf’. Cooler still are the Y-type dwarfs which have

temperatures of under 700 K. The Y-dwarfs, discovered in 2011 (*Cushing et al.*, 2011) are the coolest confirmed brown dwarfs, some of which have temperatures close to that of Earth's surface. Ammonia is apparent in these objects and may be the defining spectral characteristic of such objects. Accurate linelists of relevant molecules, including ammonia, at appropriate temperatures are required in order to determine the atmospheric properties of these dwarfs.

Table 1. Stellar classifications based on color, temperature and mass. Using this classification, the Sun would be classified as a G2-type star. (*Jaschek and Jaschek*, 1990; *Gray and Corbally*, 1994; *Brown et al.*, 2011)

| Class | Color | Effective Temperature (K) | Mass (solar masses) |
|--------------|--------------|----------------------------------|----------------------------|
| O | Blue | >30000 | >16 |
| B | Blue-white | 10000-30000 | 2.1-16 |
| A | White | 7500-10000 | 1.4-2.1 |
| F | Yellow-white | 6000-7500 | 1.04-1.4 |
| G | Yellow | 5200-6000 | 0.8-1.04 |
| K | Orange | 3700-5200 | 0.45-0.8 |
| M | Red | 2400-3700 | 0.08-0.45 |
| L | Maroon | 1300-2400 | 0.05-0.08 |
| T | Purple | 700-1300 | 0.01-0.06 |
| Y | Dark purple | <700 | 0.01-0.04 |

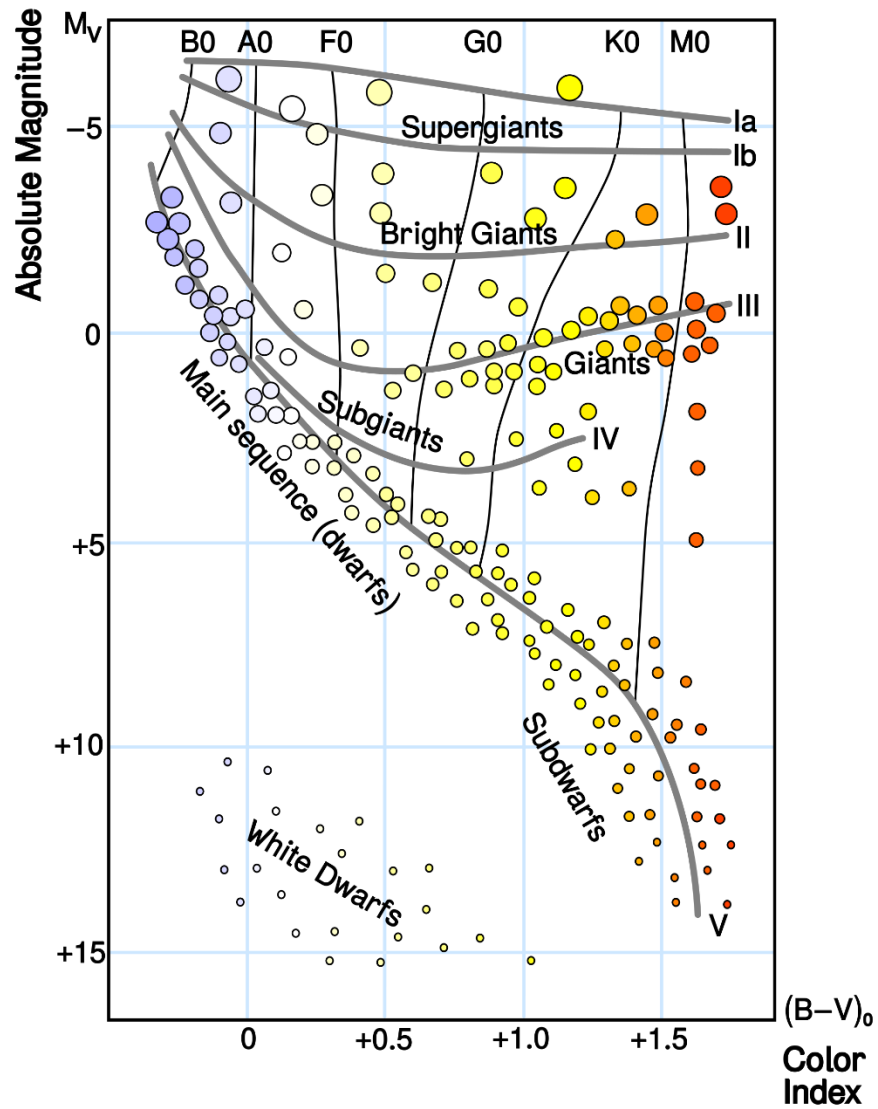


Figure 7. The Hertzsprung-Russell diagram plotting color of a star (x-axis) against its absolute magnitude (y-axis). The color of a star is an analog of temperature (see Table 1) and the absolute magnitude is related to luminosity or mass (*Freedman and Kauffmann, 2007*).

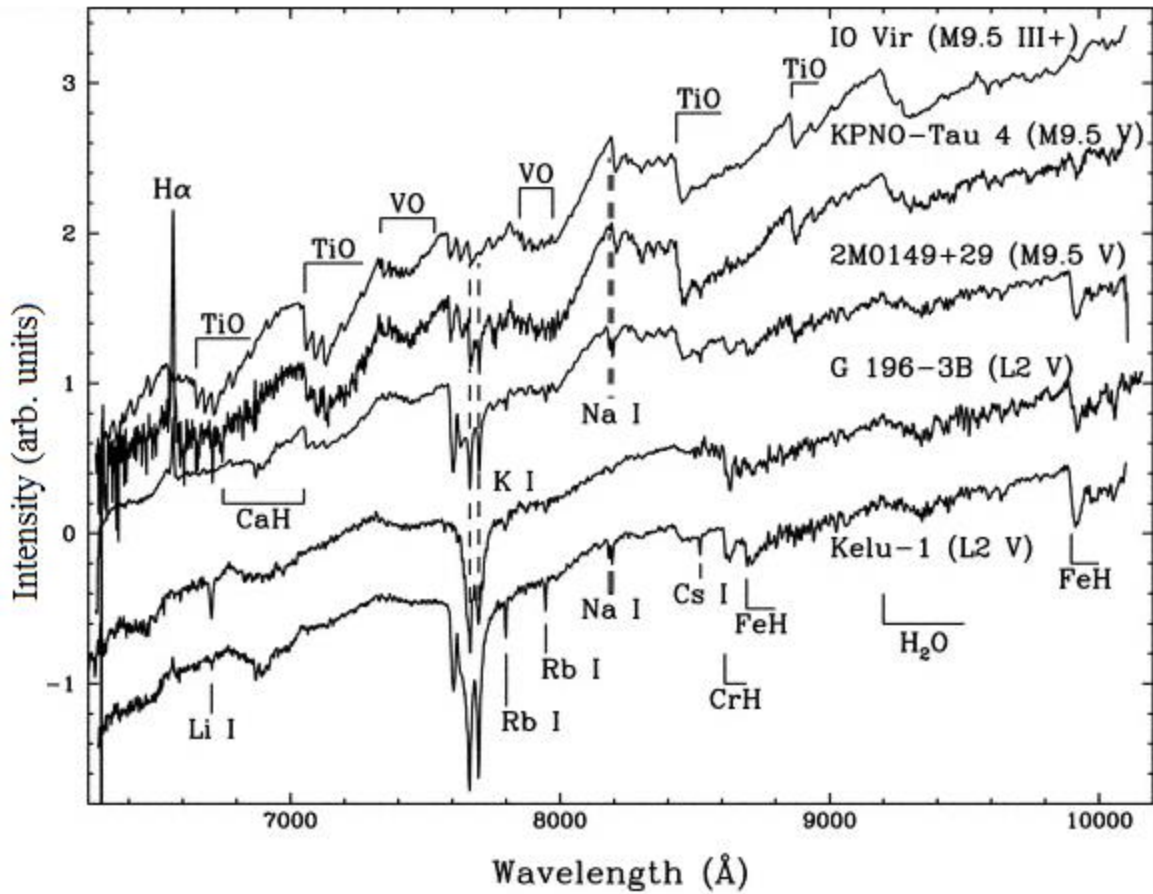


Figure 8. Near-infrared spectral energy distribution of three cool M-class stars and two hot L-dwarfs (*Mark et al., 2004*).

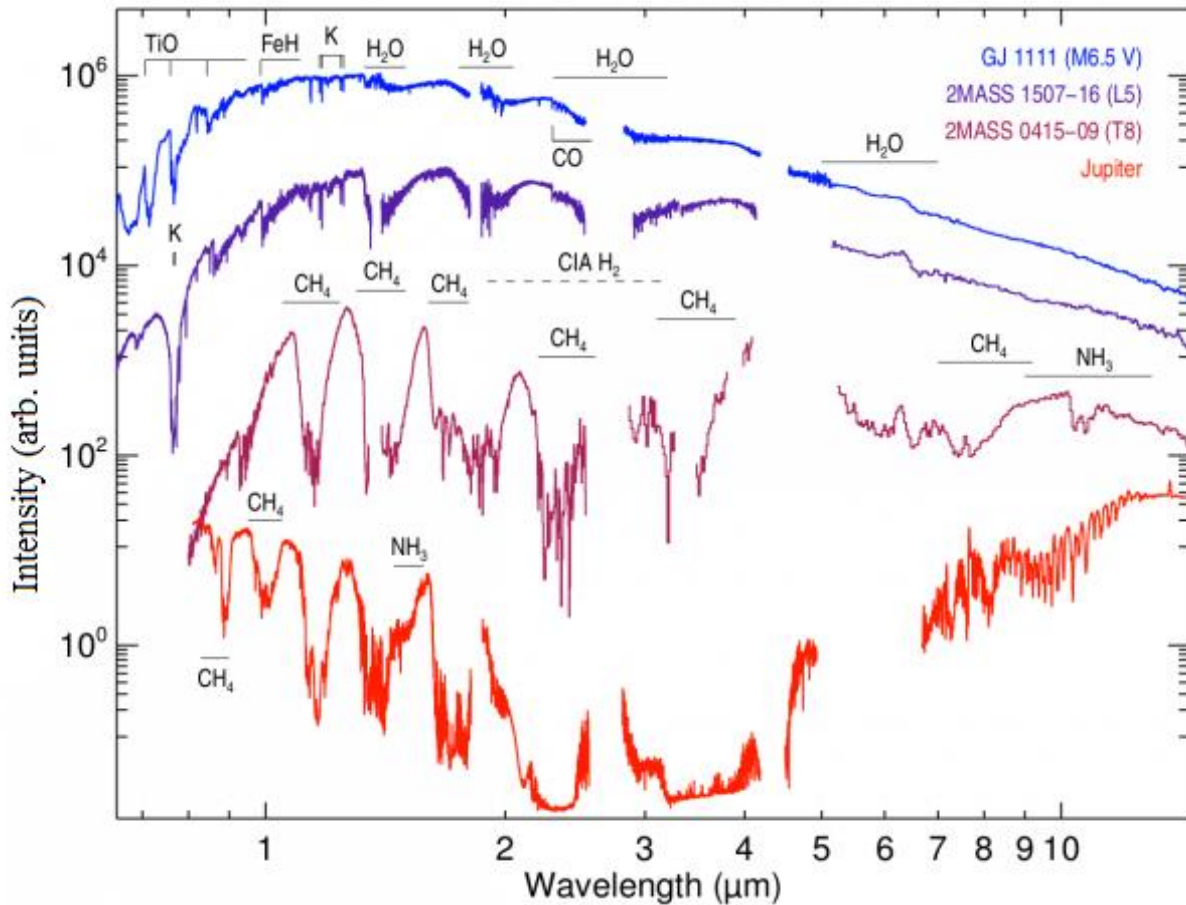


Figure 9. Spectra of L- and T-dwarfs compared to those of Jupiter and an M-class star. The strong methane features of the T-dwarf are defining features of this class. This specific cooler T-dwarf has the ammonia (NH₃) band at 10.5 μm ; this band is apparent in the spectra of Y dwarfs also (Marley and Leggett, 2009).

EXOPLANET ATMOSPHERES

In the same year as the discovery of brown dwarfs, the first planet outside of our solar system was discovered (Mayor and Queloz, 1995). Such planets are known as extrasolar planets or simply exoplanets. Since their discovery, the ubiquity of such objects has been established with almost

3500 confirmed planets as of May 2017 (the majority of which (2335), have been detected from NASA's Kepler mission (https://exoplanetarchive.ipac.caltech.edu/docs/counts_detail.html).

There are two main detection techniques for exoplanets: the radial velocity method and the transit method. The radial velocity method relies on the motion of the planet around the parent star perturbing the spectral lines of that star due to the Doppler effect as the parent star 'wobbles' around the common center of mass of the system. The second predominant method, the transit technique which is that used by the Kepler mission, observes the brightness of the star as an object passes in the line of sight between the Earth and the star (Figure 10). These methods of detection have inherent biases towards larger planets. The radial velocity technique is biased to more massive planets while the transit method is biased towards planets with larger radii. As a result, many of the planets discovered are of the 'hot Jupiter' type although there have been a number of rocky Earth-like exoplanets discovered (*Lauren and Geoffrey, 2014*).

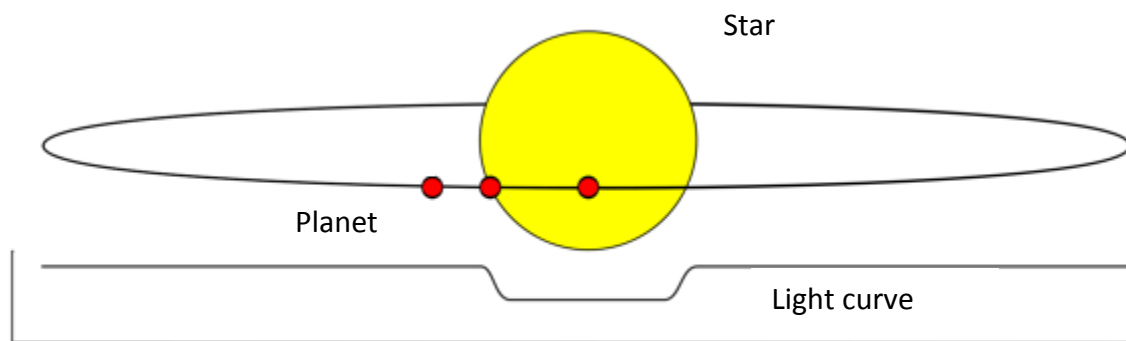


Figure 10. The transit method of exoplanet detection. Periodic dips in the brightness of the star can demonstrate the presence of a planet. The magnitude of this dip is representative of the size of the object transiting the star. Figure adapted from

https://commons.wikimedia.org/wiki/File:Planetary_transit.svg, accessed June 15 2017.

As the planet transits the star, the light passes through the atmosphere of the planet if it is not opaque. The opacity of the atmosphere as a function of wavelength gives a spectrum of the atmosphere and from this spectrum, the physical and chemical properties of the atmosphere may be determined. The first such detection of an exoplanet's atmosphere was that of Charbonneau *et al.* in 2002 (Charbonneau *et al.*, 2002); since then the atmospheres of exoplanets have been probed to discover water (Barman, 2008), methane (Swain *et al.*, 2008), carbon dioxide (Swain *et al.*, 2009) and carbon monoxide (Swain *et al.*, 2009).

Detection of a molecule using any remote sensing technique relies on observations being compared to a radiative transfer model. These models require molecular data as an input. Molecular linelists at high resolution and at appropriate temperatures produce models most capable of reproducing observations. Atmospheric models may be used to predict a spectrum of an atmosphere based on the radiative transfer code in that model. For the radiative transfer calculations to be optimal, accurate molecular data is needed, namely the position (frequency or wavelength of an absorption or emission line), the observed absorption of that line at a given concentration and how the observed absorption or shape of the line changes with conditions such as temperature and pressure. The conditions (temperature, pressure, composition) of the predictive model (generally known as a forward model) are then altered to optimally match the observations.

CHAPTER III

SPECTROSCOPY BACKGROUND

INTRODUCTION

Atmospheric remote sensing is an application of spectroscopy, the science of the interaction between light and matter. Whether spectroscopy is being used to make a measurement of an atmosphere or to record laboratory spectra with which remote sensing measurements can be understood, the principles are the same. This chapter will outline the basic theory behind infrared spectroscopy and Fourier transform measurements, including the instrumental setup in the Bernath laboratory at Old Dominion University.

Molecules exist with quantized energy levels. Transitions between different states requires discrete amounts of energy and molecules can therefore make a transition from one state to another when subjected to a photon, equal in energy to the energy difference between the two states. Radiation absorbed can cause a transition in the rotational, vibrational or electronic states or even cause dissociation of the molecule.

In general, rotational transitions require the lowest energy (microwave), followed by vibrational transitions (infrared) and then electronic transitions (visible/ultraviolet). A molecule can undergo a transition changing both the rotational and vibrational state; this is known as rotational-vibrational spectroscopy. The work in this dissertation focuses on results from rotational-vibrational spectroscopy.

ROTATIONAL SPECTROSCOPY

Pure rotational transitions generally occur in the microwave region of the electromagnetic spectrum. Classically, the moment of inertia of a molecule can be modeled by:

$$I = \sum_i m_i r_i^2 \quad (1)$$

where m_i is the mass of each atom and r_i is the distance between each atom and the rotational axis.

Assuming a linear rigid rotor diatomic molecule, the classical representation of rotational energy is given by:

$$E_R = \frac{1}{2} I_x \omega_x^2 + \frac{1}{2} I_y \omega_y^2, \quad (2)$$

where I is the moment of inertia and ω is the angular velocity. Angular momentum about the x axis is given as $J_x = I_x \omega_x$, so the rotational energy may be given by:

$$E_R = \frac{J_x^2}{2I_x} + \frac{J_y^2}{2I_y}, \quad (3)$$

and in terms of the total angular momentum, J , as:

$$E_R = \frac{J^2}{2I}. \quad (4)$$

In quantum mechanical terms, the Schrödinger equation for the rotational energy becomes:

$$\frac{\hat{J}^2 \psi}{2I} = E \psi. \quad (5)$$

The rotational energy is quantized and with the eigenvalue, E :

$$E_R = \frac{\hbar^2}{2I} J(J + 1) = BJ(J + 1), \quad (6)$$

where $B = \hbar^2/2I$ and is known as the rotational constant, given above in SI units. In spectroscopy, the rotational energy, shown above as E_R , is expressed as $F(J)$. The separation between subsequent rotational levels can therefore be shown to be equal to $2BJ$.

The assumption for the above is that the bond length between two nuclei in the molecule does not change, i.e. it is a rigid rotor. Since this bond is not fixed, when the molecule rotates, the internuclear distance, r , varies as the rotating masses of each of the nuclei distorts the bond length. Taking into account the centrifugal force and the restoring force from Hooke's law, the full rotational energy level expression is given by:

$$F(J) = BJ(J + 1) - D(J(J + 1))^2 + H(J(J + 1))^3 + L(J(J + 1))^4 + \dots \quad (7)$$

where D is known as the centrifugal distortion constant and H , L (and subsequent constants) are higher order distortion constants.

The observed absorption of a transition depends on the population of the states involved. From statistical thermodynamics, it can be shown that the population of a rotational energy level (P_J) is given by:

$$P_J = N(2J + 1) \frac{e^{-BJ(J+1)/kT}}{q_r}, \quad (8)$$

in which k is the Boltzmann constant, T is the temperature, N is the total number molecules and q_r is the rotational partition function. Therefore, the absorption depth of a molecular transition is dependent on the molecule's temperature.

VIBRATIONAL SPECTROSCOPY

For a diatomic molecule with atoms A and B, the bond can be modeled as a Hookean (harmonic) spring, having spring constant K . For a non-rotating molecule, the Hamiltonian is given by:

$$\hat{H} = \frac{-\hbar^2}{2\mu} \frac{d^2}{dr^2} + \frac{K(r-r_e)^2}{2}, \quad (9)$$

where r is the internuclear distance and r_e is the equilibrium internuclear distance and μ is the reduced mass. The eigenvalues of the vibrational Schrödinger equation are:

$$E_v = \hbar\omega \left(v + \frac{1}{2} \right), \quad (10)$$

where ω is the vibrational frequency and $v = 0, 1, 2, \dots$ and is known as the vibrational quantum number. The energy level expression for the harmonic potential is given by:

$$G(v) = \omega \left(v + \frac{1}{2} \right). \quad (11)$$

The potential energy curve of a real molecule however is not harmonic.

A commonly used anharmonic potential energy function is the Morse potential (Figure 11). The vibrational part of the solution of the Schrödinger equation for the Morse potential is (in cm^{-1}):

$$G(v) = \omega_e \left(v + \frac{1}{2} \right) - \omega_e x_e \left(v + \frac{1}{2} \right)^2, \quad (12)$$

where ω_e is the vibrational frequency and $\omega_e x_e$ is an anharmonicity constant. The anharmonicity term is positive and decreases the energy relative to the energy given by the harmonic potential.

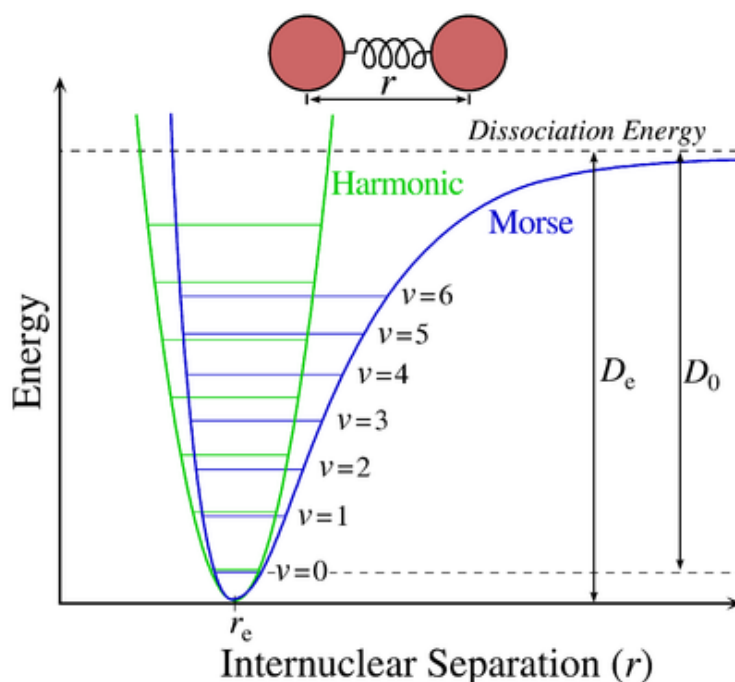


Figure 11. Two-dimensional representation of the harmonic and Morse oscillators. From <https://commons.wikimedia.org/wiki/File:Morse-potential.png>, accessed June 17th 2017.

FUNDAMENTAL, OVERTONE, HOT BAND AND COMBINATION TRANSITIONS

Fundamental vibrational transitions of a molecule occur when there is a transition from $v=0$ to $v=1$. For a linear molecule, there are $3N-5$ vibrations (where N is the number of atoms in the molecule) and for a non-linear (polyatomic) molecule there are $3N-6$ vibrations. The vibrational modes of polyatomic molecules are approximated as a sum of harmonic oscillators. Carbon monoxide (CO) will have one fundamental vibrational mode (the C-O stretching mode) and ammonia (NH₃) will have 6 fundamental modes. Possible vibrational transitions are summarized in Figure 12.

At higher energies, transitions between the states $v=0$ and $v=2$ or higher are possible. This is referred to as an overtone. Assuming the harmonic oscillator approximation, the $v=0$ to $v=2$ transition will occur at twice the transition frequency of the fundamental, although in a more realistic anharmonic system this energy will be slightly less than that predicted by the harmonic oscillator.

Hot bands are observed for a transition between two excited vibrational energy levels, for example $v=1$ to $v=2$. The observed absorption of any transition is related to the population of the energy levels involved. At room temperature, the ground state ($v=0$) is the most populated, followed by $v=1$. As such fundamental transitions are the strongest observed. The population of vibrational energy levels are based on the Maxwell-Boltzmann distribution and therefore the observed absorption of hot bands increase with temperature. For example, at 298 K, the $v=0$ state population of the CO molecule is 99.997% and the $v=1$ state has a population of 0.00282%. At 1000 K the ground state population is 95.6% and the population of the $v=1$ state is 4.21%. Due to the anharmonicity of molecules, hot bands occur at lower energies than fundamental transitions.

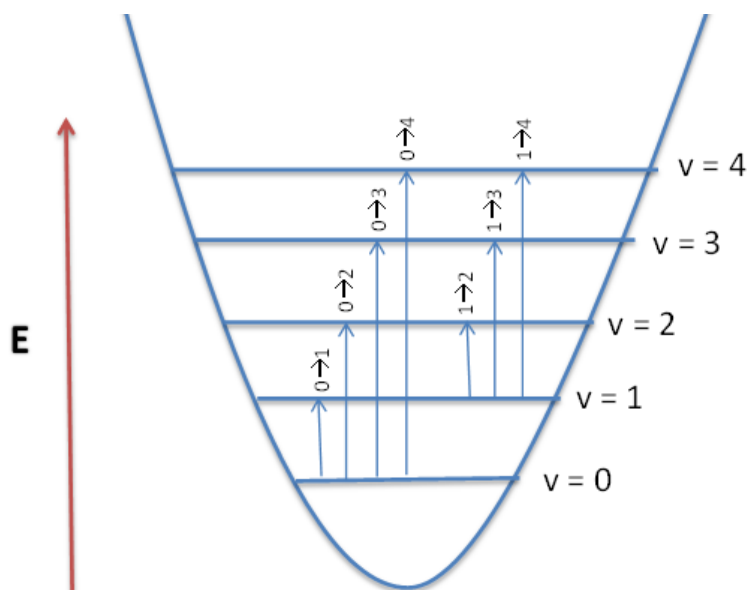


Figure 12. Energy level diagram showing fundamental (1-0), overtone (2-0, 3-0, 4-0) and hot band (2-1 3-1, 4-1) transitions. Figure from:

https://chem.libretexts.org/@api/deki/files/78873/%253Dvib_diatomic_molecule.png?revision=, accessed June 15th 2017.

For polyatomic molecules with more than one fundamental vibrational mode, combination bands occur when quantum numbers for two more vibrational modes change (*Bernath, 2005*). Combination bands break the selection rules of the harmonic oscillator and are generally weak, although they become important in spectra at energies above the fundamental such as those studied in this dissertation.

SELECTION RULES

A molecule can undergo rotational transitions while also changing vibrational states, these are known as rotational-vibrational transitions. For a rotational-vibrational transition to occur, there

must be a change in the dipole moment of the molecule as it vibrates. A transition is allowed for a diatomic molecule for $\Delta J = \pm 1$ if the molecule has no net spin or orbital angular momentum, where ΔJ is the difference in rotational quantum number J in the transition between $v=0$ and $v=1$ (fundamental band). For diatomics with net spin or orbital angular momentum transitions of $\Delta J = 0$ are also possible (see Figure 13). A transition of $\Delta J = -1$ is known as a P branch, $\Delta J = 0$ as a Q branch and $\Delta J = +1$ as an R branch.

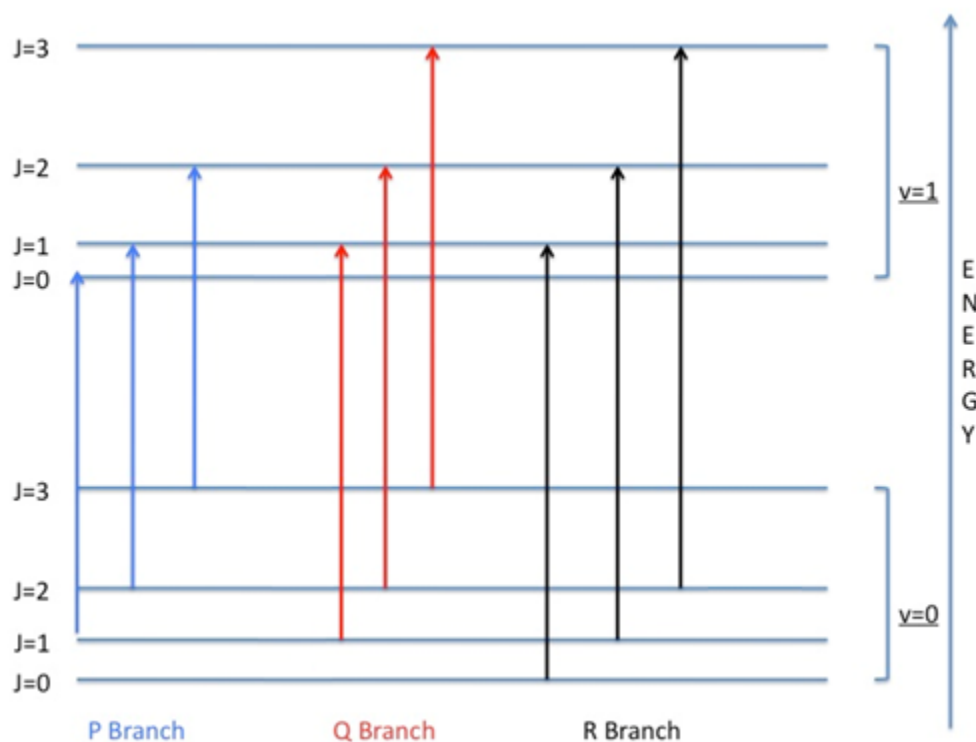


Figure 13. Schematic of P, Q and R transitions. Adapted from

https://chem.libretexts.org/Core/Physical_and_Theoretical_Chemistry/Spectroscopy/Fundamentals_of_Spectroscopy/Selection_rules_and_transition_moment_integral, accessed June 15th, 2017.

SPECTRAL LINESHAPE

A molecular transition from one quantized energy state to another should result in a spectral feature of infinitesimal width. Real spectra however show that spectral lines have widths and characteristic shapes. The shape of a spectral line is known as its lineshape and falls in to one of two categories: homogeneous and inhomogeneous. Homogeneous lineshapes occur when every molecule in the system is affected equally, i.e. they have the same lineshape function. This usually results in a Lorentzian lineshape.

The width of a line may be broadened by a number of physical factors. An example of homogenous broadening is pressure broadening. The cosine wave associated with the oscillation of the dipole moment is interrupted by collisions with other molecules. The frequency components obtained by Fourier transformations of the time dependent cosine wave result in a FWHM (full width at half maximum) of:

$$\Delta\nu_{1/2} = \frac{1}{\pi T} \quad (13)$$

where T is the average time between successive collisions. The average time between collisions is inversely proportional to the pressure, p so the FWHM of a line is therefore proportional to the pressure. The effect of pressure on a spectrum can be seen in Figure 14, where at 10 Torr the spectral features of ammonia are more easily identifiable. The spectrum at 100 Torr provides more signal (due to the Beer-Lambert law) but suffers from line broadening. Broadening of two or more lines close together may result in them overlapping and even blending into one single line. The blending of three resolved lines into one is shown in Figure 14 at 6479.25 cm^{-1} . The lower pressure spectrum results in less line blending and therefore better determination of individual line absorption whereas a higher pressure spectrum allows much weaker lines to be identified.

Inhomogeneous lineshapes result from molecules in the system having different lineshapes. An example of inhomogeneous broadening is Doppler broadening. At temperatures above absolute zero, molecules will move with a distribution of velocities. A moving molecule will emit a photon that is Doppler shifted, depending on the direction of motion relative to the observer. This effect results in a distribution of frequencies about some line center, with the scale of the distribution dependent on the molecular motion and ultimately the temperature of the system, resulting in a Gaussian lineshape.

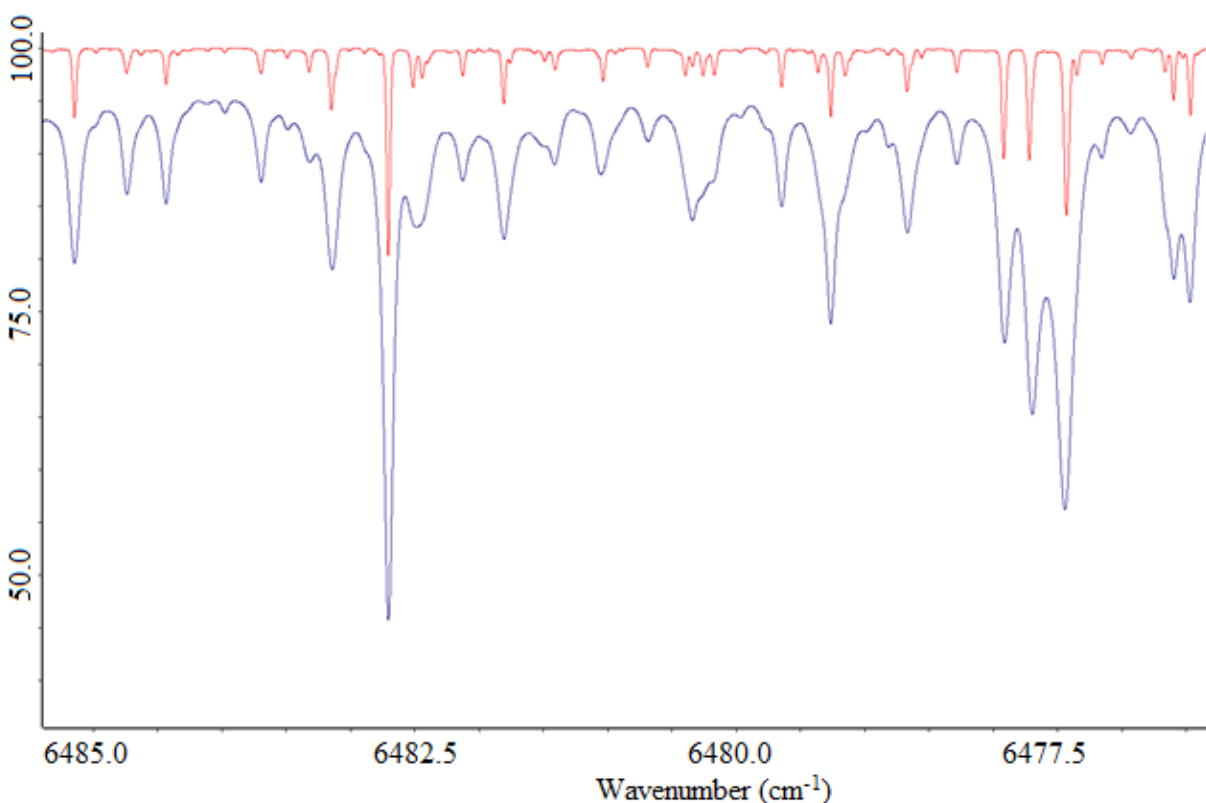


Figure 14. Transmission spectra of ammonia at both 10 Torr (red) and 100 Torr (blue; offset by 5%).

Other line broadening effects are possible, but will not be discussed here since pressure and Doppler broadening are the dominant effects on the lineshape in the experiments discussed here.

A convolution of these two lineshape functions is known as the Voigt lineshape function (Figure 15).

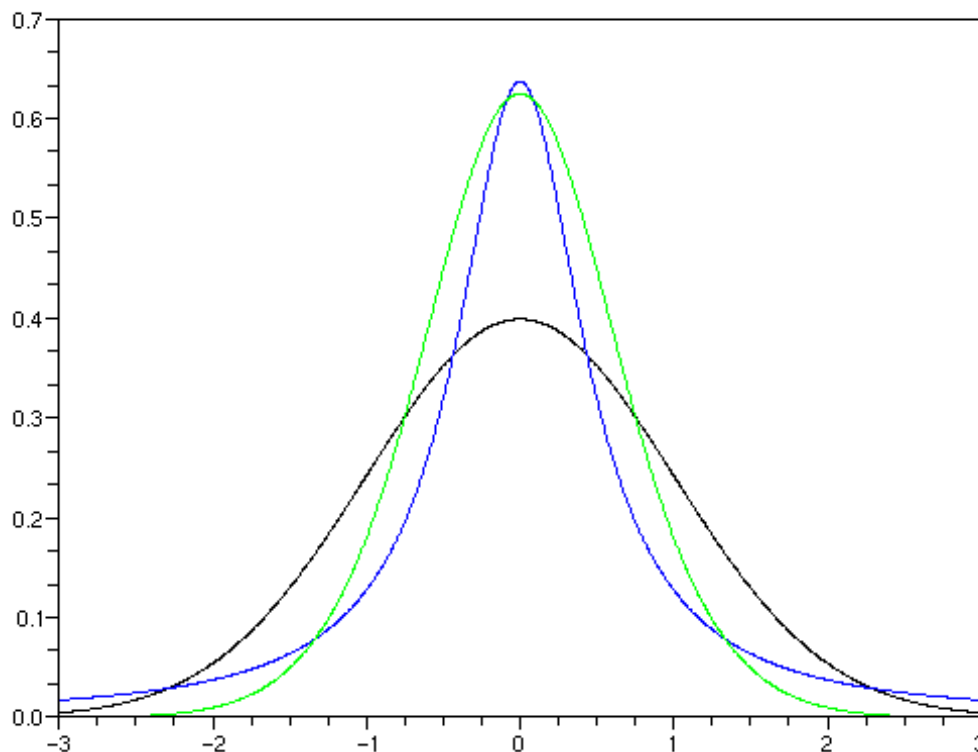


Figure 15. Gaussian (black), Lorentzian (blue) and Voigt (green) lineshapes. Units are arbitrary.

Adapted from https://commons.wikimedia.org/wiki/File:Fonction_voigt.png, accessed June 15, 2017.

LINELISTS

The main motivation for the laboratory spectroscopy experiments conducted for this dissertation is to provide linelists from which atmospheric models can be constructed. In order to produce an accurate atmospheric model, the position (transition frequency), line intensity and lower state energy are required. The lower state energy of a transition allows the intensity to be extrapolated

(or interpolated) for temperature; this will be detailed in Chapter VI. Each transition has a unique set of parameters that describe the upper and lower state involved. These parameters are known as quantum numbers and assignment of these quantum numbers allows a more complete description of the transition. Quantum assignments are desirable for comparison to *ab initio* calculations so that corrections can be made to the theory; however, assignments are not necessary for construction of an accurate atmospheric model.

The High resolution TRANsmission molecular absorption database (HITRAN (*Rothman et al.*, 2013)) is a compilation of linelists and absorption cross-sections (effective area of the molecule for absorption of a photon as a function of wavelength) for 47 different molecules including ammonia, carbon monoxide and propane. This database generally provides the most accurate assignments for the molecules included. HITRAN is designed for use at 296 K, primarily for applications to the Earth's atmosphere. HITRAN is a mix of experimentally obtained linelists and calculated ones. Calculated linelists have the advantage of being more complete; however, experimental linelists generally have more accurate line positions. Often a combination of both techniques approaches yields the best linelist. Many of the lines measured for this dissertation are already in HITRAN; however, this work includes the line intensities at higher temperatures and adds additional lines, especially at higher wavenumbers and those from hot bands. The results of these are detailed in Chapter V.

FOURIER TRANSFORM SPECTROSCOPY

This dissertation contains experimentally obtained spectra of two molecules: ammonia (NH_3) and propane (C_3H_8). Both of these studies were carried out using a Bruker IFS 125HR Fourier

transform spectrometer (FTS). The basis of an FTS is the Michelson interferometer, a schematic of which is given in Figure 16, an instrument developed by Michelson in the 1880s to study the speed of light.

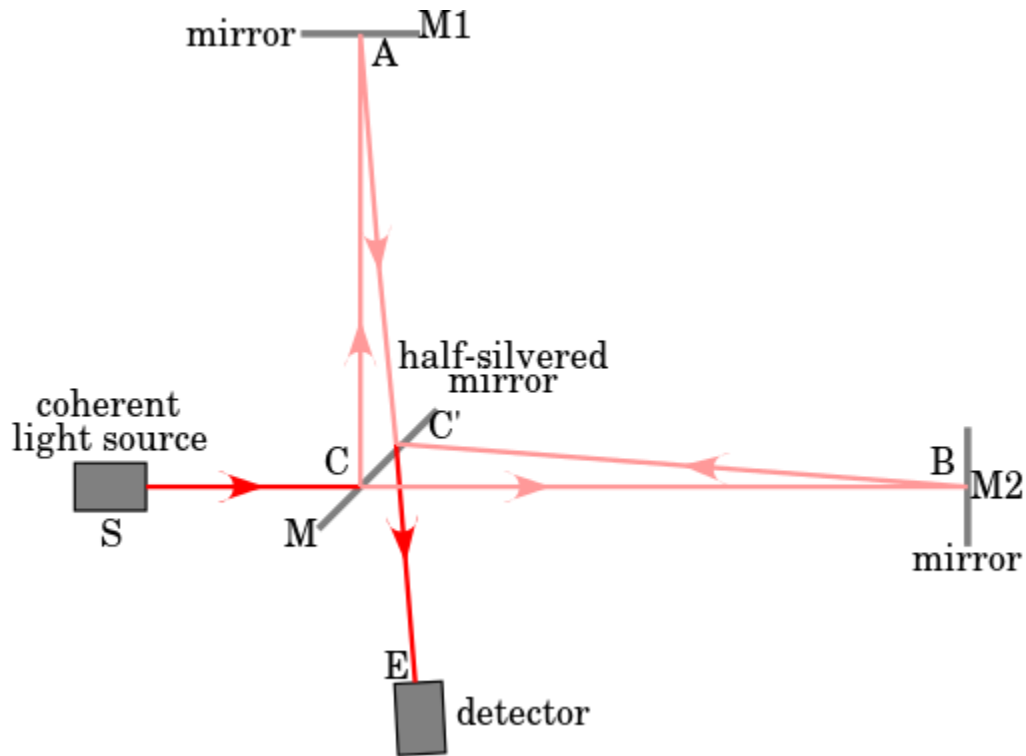


Figure 16. Layout of a Michelson interferometer, the fundamental component of a Fourier transform spectrometer (Krishnavedala 2014).

The incident light from an external source, S , is separated into two beams by the beamsplitter, M . The two beams are directed to two mirrors, one of which is fixed and the other can be moved a distance d . When the beams recombine at the beamsplitter, an interference pattern is created from the changing optical path difference x ($x = 2d$) from the movable mirror. If the light is coherent (monochromatic), the intensity $I(x)$ of the interferogram of the recombined beam is given by:

$$I(x) = B(\tilde{\nu})[1 + \cos(2\pi\tilde{\nu}x)] \quad (14)$$

where $B(\tilde{\nu})$ is the spectral power density as a function of wavenumber. For an incoherent source (i.e. from a continuous spectrum of frequencies), the total intensity is the sum over all frequencies, in wavenumber notation, in which $\tilde{\nu}$ is in wavenumbers (cm^{-1}) and x is in cm, this becomes:

$$I(x) = \int_0^{\infty} B(\tilde{\nu})[1 + \cos(2\pi\tilde{\nu}x)]d\tilde{\nu}, \quad (15)$$

where the first term in the brackets is a constant and the second (cosine) term contains all the information of the spectrum. This part and its Fourier transform pair are as follows:

$$I'(x) = \int_{-\infty}^{\infty} B(\tilde{\nu})[\cos(2\pi\tilde{\nu}x)]d\tilde{\nu} \quad (16)$$

$$B(\tilde{\nu}) = \int_{-\infty}^{+\infty} I'(x) [\cos(2\pi\tilde{\nu}x)]dx. \quad (17)$$

There is a fundamental limit to the possible resolution obtained as the mirrors can only be moved a finite distance. The limits to the integral will be given by the optical path difference, x .

The Bruker IFS 125HR Fourier transform spectrometer has a maximum optical path difference (MOPD) of 5 meters corresponding to a resolution (defined as $1/\text{MOPD}$) of 0.002 cm^{-1} . The optical layout of the Bruker IFS 125HR is given in Figure 18. The source for the system was a tube furnace, shown in Figure 17. The light path from the lamp enters the spectrometer at the spectrometer input aperture (labeled as C in Figure 18). The two parts of the apparatus are shown in photograph in Figure 19.

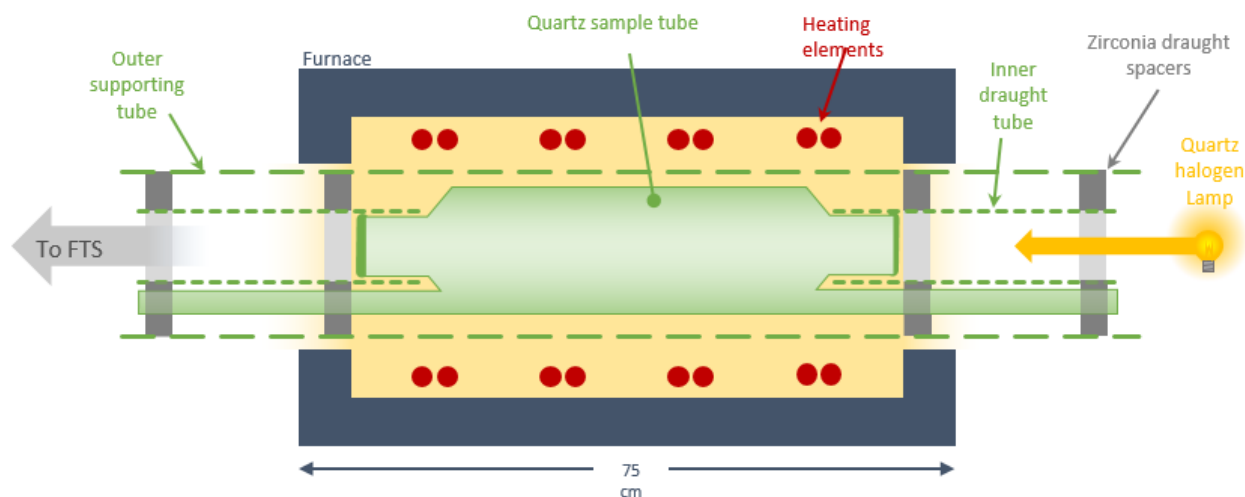


Figure 17. Schematic of the tube furnace used as a source.

The signal from the tube furnace enters the aperture of the spectrometer (C in Figure 18). In the schematic the beamsplitter (D) ideally reflects half of the signal onto the fixed mirror (E) and half onto the movable mirror (F) and the light is recombined at the beamsplitter. These are analogous to the half-silvered mirror and mirrors M1 and M2 in Figure 16 of the Michelson interferometer, the essential component of an FTS. The detector arm of the FTS uses a series of mirrors to lead the signal to the detector (A). For the frequency range studied in this work, a liquid nitrogen cooled indium antimonide (InSb) detector was used, providing detection over the spectral range 1850-9600 cm^{-1} .

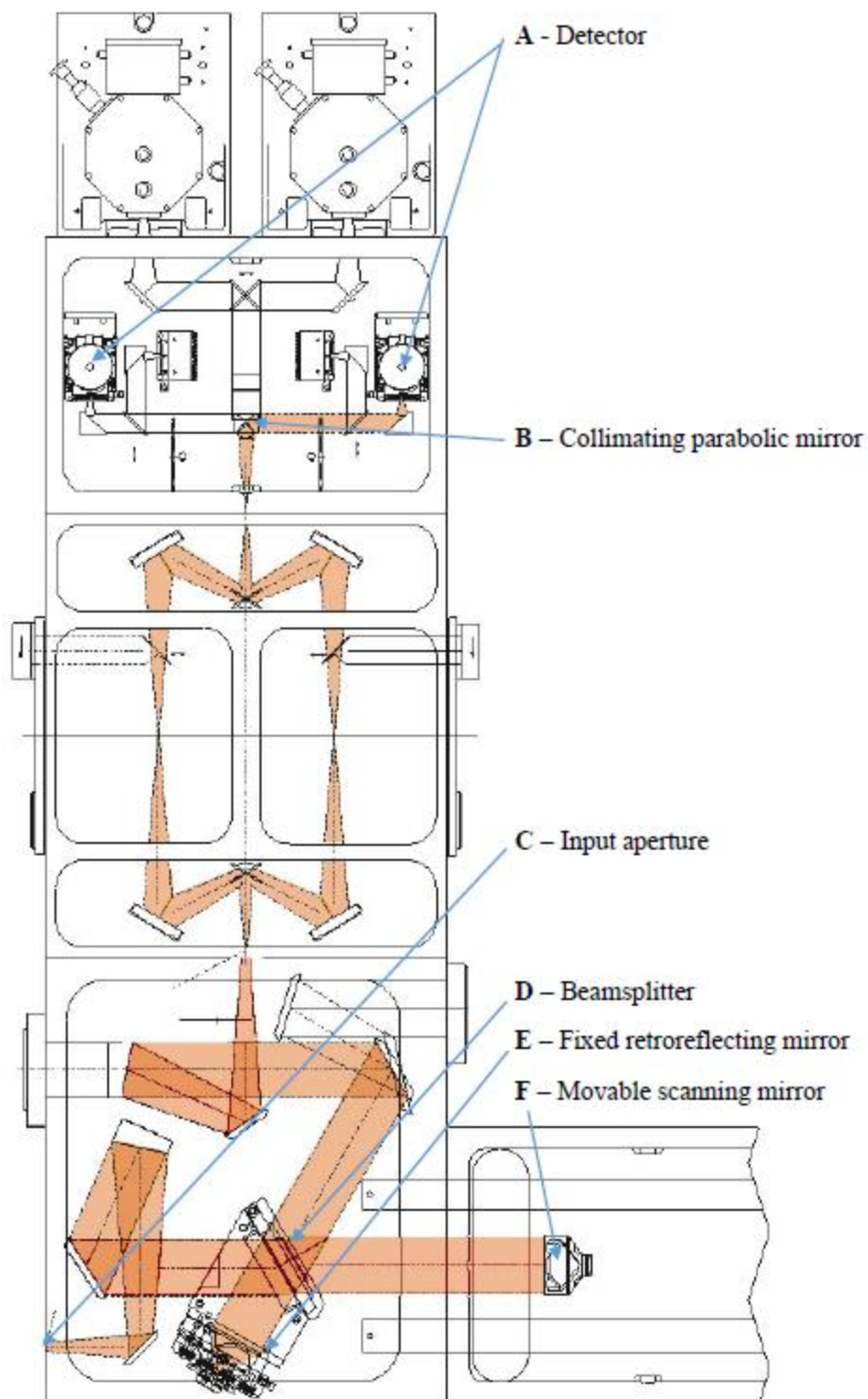


Figure 18. Schematic of the Bruker IFS 125HR FTIR with labels of main components. Adapted from Bruker IFS 125HR User Manual (Bruker 2006).

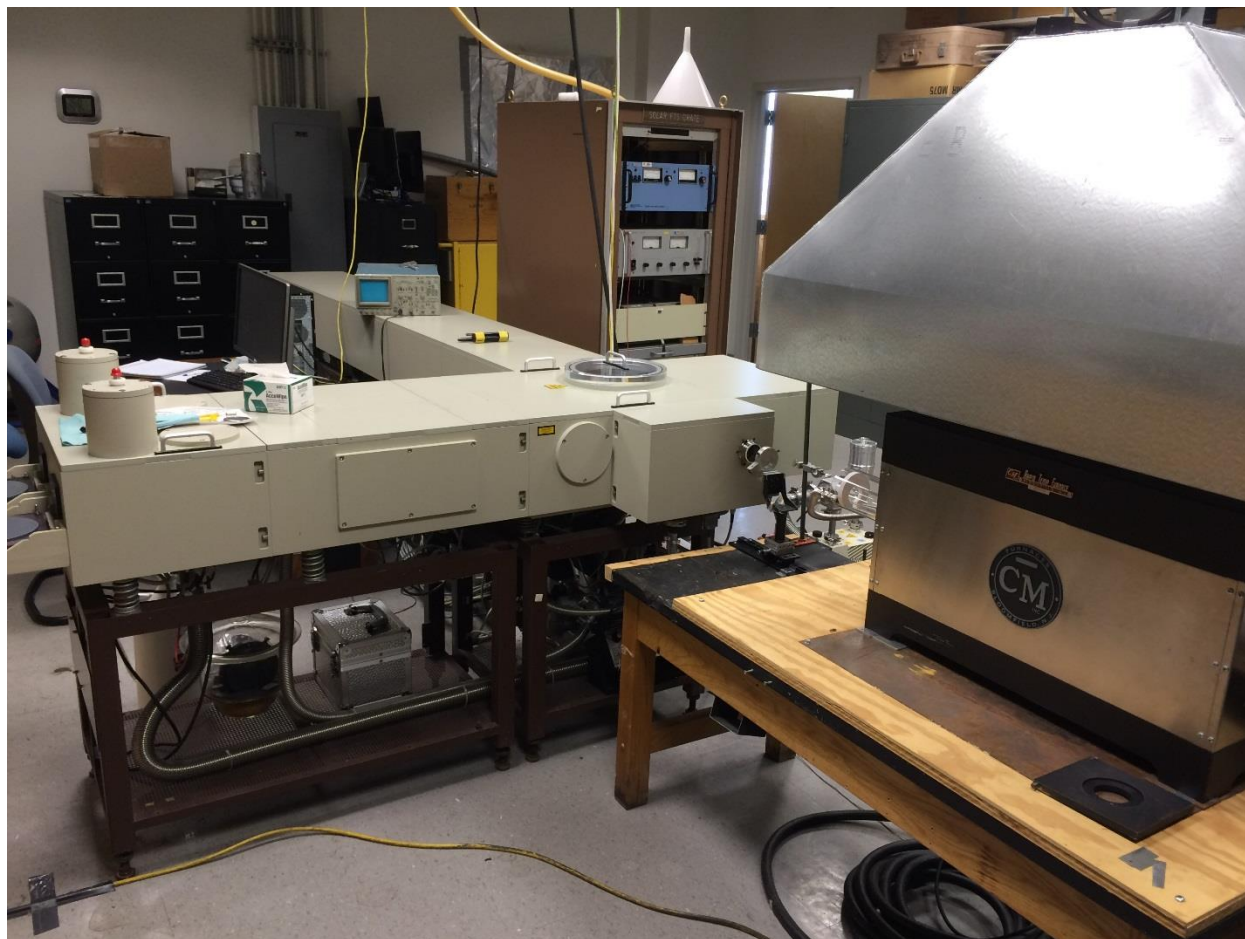


Figure 19. Photograph of the tube furnace (on the right with exhaust hood over it) and the Bruker IFS 125HR FTS (center) in the Bernath laboratory at ODU.

Bruker provides software, called OPUS, for controlling the instrument parameters and the processing of spectra obtained from the spectrometer. In order to calculate a desired transmission spectrum, absorption and emission (as well as background) spectra were recorded. Chapter VI describes the calculation in detail. One common problem with analysis of spectra in the infrared is the ubiquity of water vapor lines. Water is both abundant in the atmosphere and variable in its concentration throughout the day. For full analysis of the obtained spectrum, water must be

removed. If the concentration of water were constant, then water lines would be removed when calculating the transmission spectrum. Figure 21 shows the three spectra. The black spectrum (offset -20%) is the absorption spectrum with ammonia in the tube furnace, the green plot is a background spectrum with the tube furnace evacuated. The blue plot is the background plot corrected to have the baseline at zero. Subtraction of this new 'water spectrum' from the sample spectrum should remove the contribution of water (and other background signals) from the signal spectrum; however, the varying concentrations of atmospheric water result in a residual signal which is demonstrated in Figure 20. This can then be removed by manually cutting sections from the spectrum as shown in the black signal. In the spectrum shown in Figure 20 there is no ammonia signal; if there is a mix of target gas and water then care must be taken not to cut out sections of spectrum containing the sample.

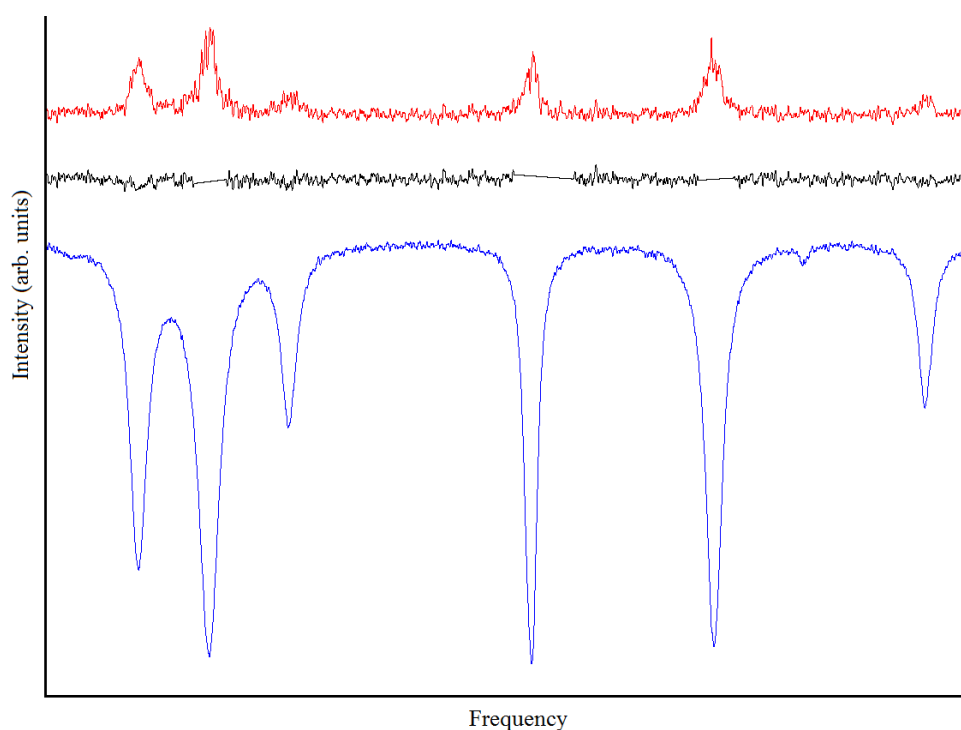


Figure 20. Water line removal, the sample is shown in the blue trace, initial water removal in red and the cut spectrum in black.

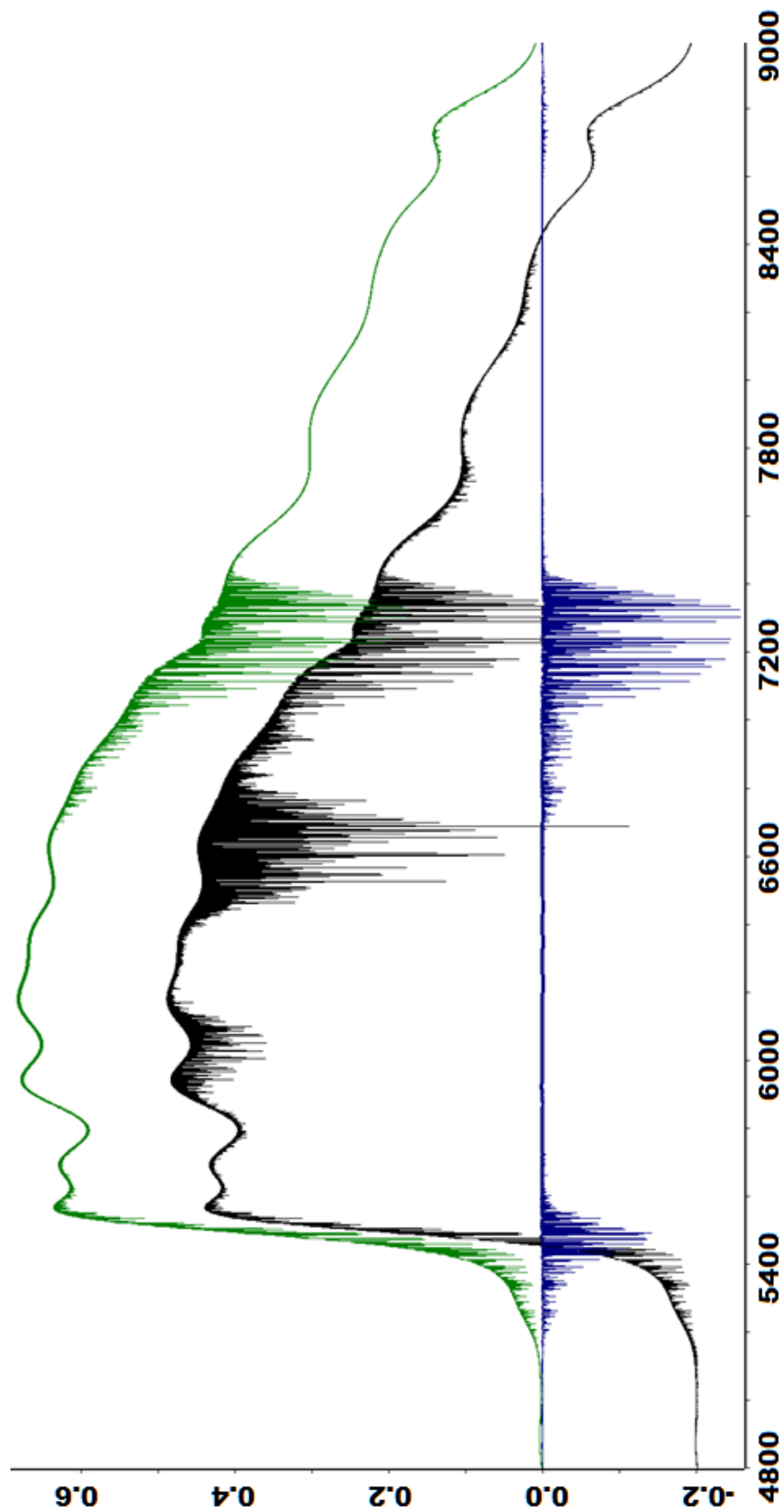


Figure 21. The sample spectrum (black, shifted -20%) includes signal from the sample (NH_3) and other gases, mainly water in the air gap between the furnace and the spectrometer. The green trace shows the background signal, which does not include ammonia, when corrected for the baseline, this becomes the blue trace which may be subtracted from the original spectrum.

In order to obtain a linelist, individual spectral features must be measured for their frequencies and intensities. WSpectra (*Carleer, 2001*) is a program used to pick peaks in a spectrum. This program is run to automatically find the peaks in a spectrum and has a wavenumber accuracy of 9×10^{-6} cm^{-1} and an intensity accuracy of 1% or better (*Carleer, 2001*). This peak picking is used with an intensity threshold; however, the automation is not always perfect and the spectrum must be checked manually to ensure that erroneous lines have not been included and that sample lines have not been missed. WSpectra allows the user to simply select or deselect lines on the interface.

CHAPTER IV

ISOTOPIC FRACTIONATION OF ATMOSPHERIC CARBON MONOXIDE

The results and the majority of the text presented in this chapter have been published in the Atmospheric Science special edition of the Journal of Molecular Spectroscopy (*Beale et al.*, 2016a). The co-authors for this work are; Eric Buzan (Old Dominion University), who obtained the WACCM output and produced the data from which Figure 27 was made as well as sourcing the data for Table 7; Chris Boone (University of Waterloo) who, as the retrievals scientist for the ACE mission, calculated the forward model and obtained the volume mixing ratios for each occultation, and Peter Bernath (Old Dominion University) who is the Mission Scientist for ACE and oversaw the project. As first author of this paper, all further ACE analysis after retrieval, all experimental data analysis, all other figures (unless explicitly cited) and all writing presented here is my original work.

INTRODUCTION

Carbon monoxide (CO) is an important molecule in atmospheric chemistry. Although it has a small direct global warming potential, it acts as an indirect greenhouse gas as a result of the formation of carbon dioxide (CO₂) through the reaction with the hydroxyl radical (OH). The reaction between CO and OH also leads to the formation of tropospheric ozone (O₃) (*Pommier et al.*, 2010) which acts as both a pollutant and a greenhouse gas (*Finlayson-Pitts and Pitts*, 1997). The lifetime of CO

(~2 months) makes it an excellent tracer of atmospheric dynamics, in particular vertical transport at high latitudes (*Clerbaux et al.*, 2008). Both CO and O₃ are considered major pollutants in the troposphere (*Parrish*, 1993) and have detrimental effects on human health, including lung disease and cancer (*Ebi and McGregor*, 2008).

Table 2. Estimates of sources (first four rows) and sinks (last two rows) (both in Tg/yr) for carbon monoxide.

| | WMO (<i>Haigh</i> , 1993) | Seiler & Conrad (<i>Conrad and Seiler</i> , 1988) | Khalil & Rasmussen (<i>Khalil and Rasmussen</i> , 1990) |
|---------------------------|-------------------------------|--|--|
| Fossil Fuel | 440 | 640±200 | 400-1000 |
| Biomass burning | 640 | 1000±600 | 335-1400 |
| CH ₄ oxidation | 660 | 900±500 | 300-1400 |
| NMHC oxidation | 600 | 600±300 | 400-1000 |
| OH reaction | 900±700 | 2000±600 | 2200 |
| Soil uptake | 256 | 390±140 | 250 |

CO has four major sources in the troposphere: fossil fuel combustion, biomass burning, methane oxidation and non-methane hydrocarbon oxidation. The contributions of each of these are summarized in Table 2. The major sink throughout the atmosphere is the reaction with OH. Since the concentration of OH is strongly dependent on the actinic flux, and therefore the time of year, the tropospheric lifetime of CO varies seasonally (1-6 months). The spatial distribution is also varied given the relatively short lifetime and the disparity of fossil fuel production between the Northern and Southern Hemispheres. In the troposphere CO is a precursor (through production of HO₂) to the formation of ozone under high NO_x conditions (*Funke et al.*, 2009; *Röckmann et al.*, 2002; *Pommier et al.*, 2010). In the stratosphere and mesosphere the main sources of CO are from

formaldehyde (CH₂O), which is formed through hydrocarbon oxidation (*Feilberg et al.*, 2004; *Feilberg et al.*, 2005), and photodissociation of CO₂, respectively.

The volume mixing ratio and lifetime of CO in the mesosphere is much higher than in the troposphere or stratosphere (Figure 22) and it can be used as an atmospheric tracer of vertical transport and other dynamical effects in the upper atmosphere.

CO exists predominantly as the ¹²C¹⁶O isotopologue, but there are appreciable amounts of ¹³C¹⁶O in the atmosphere and to a lesser extent ¹²C¹⁷O and ¹²C¹⁸O. The various CO sources have different isotopic signatures (*Gros et al.*, 2002; *Brenninkmeijer et al.*, 1999; *Wang et al.*, 2012) because of the different isotopic compositions of the reactants and the different fractionation processes that they undergo during CO formation. Indeed removal by OH oxidation also has considerable isotopic fractionation (*Feilberg et al.*, 2005). Measurements of the isotopic makeup of CO can therefore lead to a determination of the various sources and sinks (*Mak et al.*, 2003; *Manning et al.*, 1997; *Röckmann et al.*, 2002; *Brenninkmeijer et al.*, 1999).

The variation of the isotopic composition of a sample from the standard isotopic abundance is given in δ notation and expressed as ‘per mil’ (‰) changes. For ¹³C, this would be expressed as:

$$\delta^{13}\text{C} = \left[\frac{[\text{}^{13}\text{C}_\text{S}]/[\text{}^{12}\text{C}_\text{S}]}{[\text{}^{13}\text{C}_\text{R}]/[\text{}^{12}\text{C}_\text{R}]} - 1 \right] \times 1000 \text{ ‰}, \quad (18)$$

In which the S and R subscripts refer to the concentrations for the sample and reference, respectively. For ¹³C, this reference is the Vienna Pee Dee Belemnite (V-PDB) which has a [¹³C]/[¹²C] value of 0.0112372.

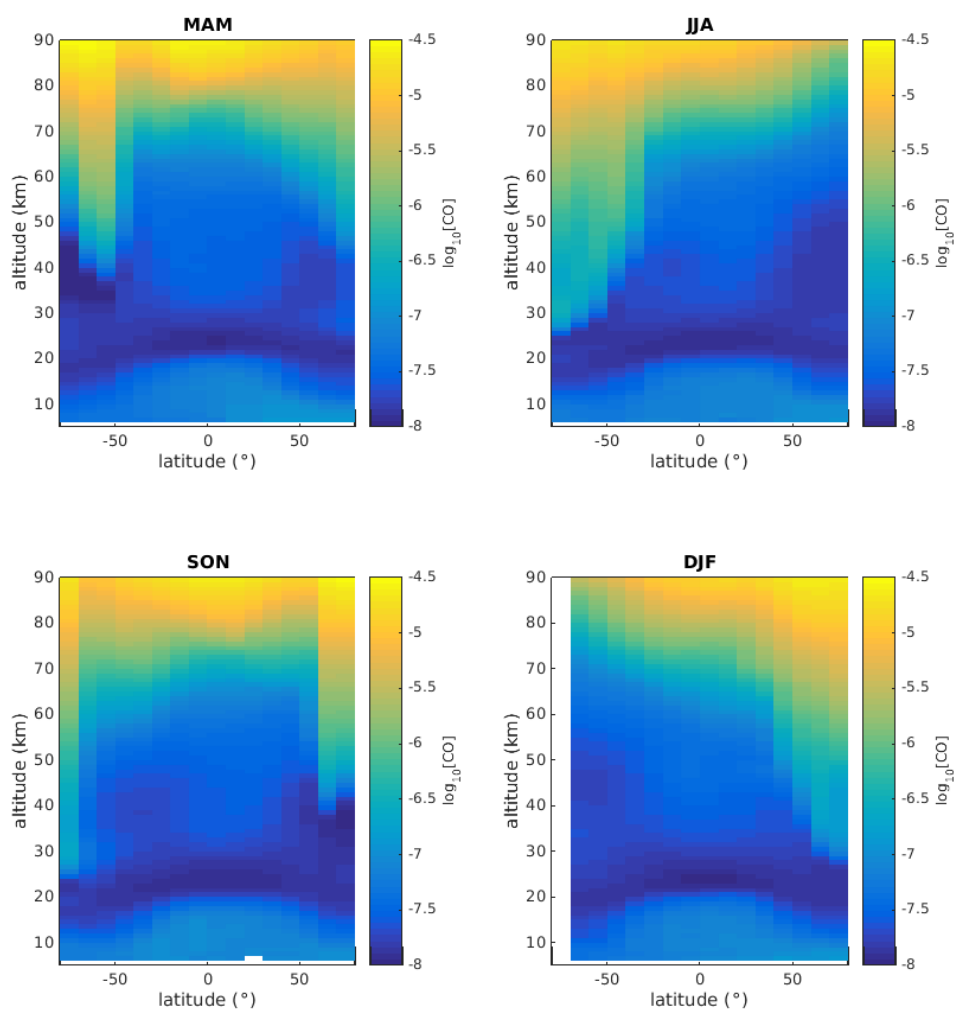


Figure 22. Global distribution of carbon monoxide volume mixing ratio by season as measured by the ACE-FTS. MAM represents the binned months of March, April and May (spring); JJA represents June, July and August (summer); SON represents September, October and November (autumn) and DJF represents December, January and February (winter). The colder and therefore denser air, traced by CO formed by CO₂ photolysis (high VMR), in each hemisphere's respective winter can be seen to descend to lower altitudes (*Beale et al., 2016a*).

A number of previous studies have used CO isotopologues to quantify the relative contributions of the various sources and sinks. In situ collection and measurement of suitable samples can be difficult due to the small volume mixing ratio of CO and generally sophisticated cryogenic traps are used (*Brenninkmeijer et al.*, 1999) to isolate the sample. This technique is clearly spatially limited, although analysis with mass spectrometry techniques provides highly precise values for the isotopic composition of a sample. Samples from the high latitude northern hemisphere (*Röckmann et al.*, 2002), Japan (*Kato et al.*, 2000), Barbados (*Mak et al.*, 2003), a transect along the Trans-Siberian railroad (*Tarasova et al.*, 2007) and other locales have been analyzed and modeling efforts have included a two dimensional model employed by *Manning et al.* (1997) to predict CO concentrations and $\delta^{13}\text{C}$ values in the extra tropical Southern Hemisphere. The CARIBIC project has provided isotopic fractionation values for CO in the upper troposphere and lower stratosphere (*Gromov and Brenninkmeijer*, 2015), although the sampling method suffered from contamination. However, all of these results are relatively local and cover a limited altitude range. Given the seasonal and spatial variability of CO, as well as the different contributions of sources and sinks, a more comprehensive study is needed. Nadir sounding instruments such SCIAMACHY (*de Laat et al.*, 2006) and MOPITT (*Deeter et al.*, 2003) and limb sounders such as MIPAS (*Funke et al.*, 2009), IASI (*George et al.*, 2009) and ACE (*Clerbaux et al.*, 2005) have successfully measured CO from satellite platforms, although this has not yet been extended to isotopic measurements.

EXPERIMENTAL

SCISAT is a Canadian-led satellite mission that was launched in 2003. The primary instrument on board is the Atmospheric Chemistry Experiment Fourier transform spectrometer (ACE-FTS)

which is a high resolution (0.02 cm^{-1}) spectrometer covering the spectral region $750\text{--}4400\text{ cm}^{-1}$. The instrument records solar occultation spectra, recording transmission spectra through the limb of the Earth's atmosphere at sunrise and sunset over a latitudinal range of about 85°S to 85°N . The satellite's orbital inclination of 74° provides near global coverage with a strong weighting toward occultations at higher latitudes (Figures 23 and 24). Profiles of over 30 trace gas species are obtained from ACE-FTS spectra, at a vertical resolution of around 3-4 km (Bernath *et al.*, 2005).

Retrievals of ACE-FTS data were obtained using version 3.5 of the ACE-FTS software (Boone *et al.*, 2013). Pressure and temperature profiles are first derived from the ACE-FTS spectra through the analysis of CO_2 lines, and then volume mixing ratio (VMR) profiles are retrieved for the various atmospheric constituents of interest using a forward model in which the target molecule's concentration is adjusted until the calculated spectrum matches observations. Spectroscopic parameters for the forward model calculations were taken from the HITRAN 2004 database (Rothman *et al.*, 2005).

The subsidiary isotopologues from a number of molecules are routinely retrieved from ACE-FTS measurements, including H_2O , CO_2 , O_3 , N_2O , CH_4 , OCS , and CO (<http://www.ace.uwaterloo.ca/>). For carbon monoxide, in addition to the main isotopologue ($^{12}\text{C}^{16}\text{O}$), VMR profiles are retrieved for $^{13}\text{C}^{16}\text{O}$, $^{12}\text{C}^{18}\text{O}$ and $^{12}\text{C}^{17}\text{O}$ isotopologue ($^{12}\text{C}^{16}\text{O}$), VMR profiles are retrieved for $^{13}\text{C}^{16}\text{O}$, $^{12}\text{C}^{18}\text{O}$ and $^{12}\text{C}^{17}\text{O}$. The high altitude portion (above $\sim 95\text{ km}$) of the retrieval for main isotopologue CO in version 3.5 differs significantly from version 3.0, the previous processing version.

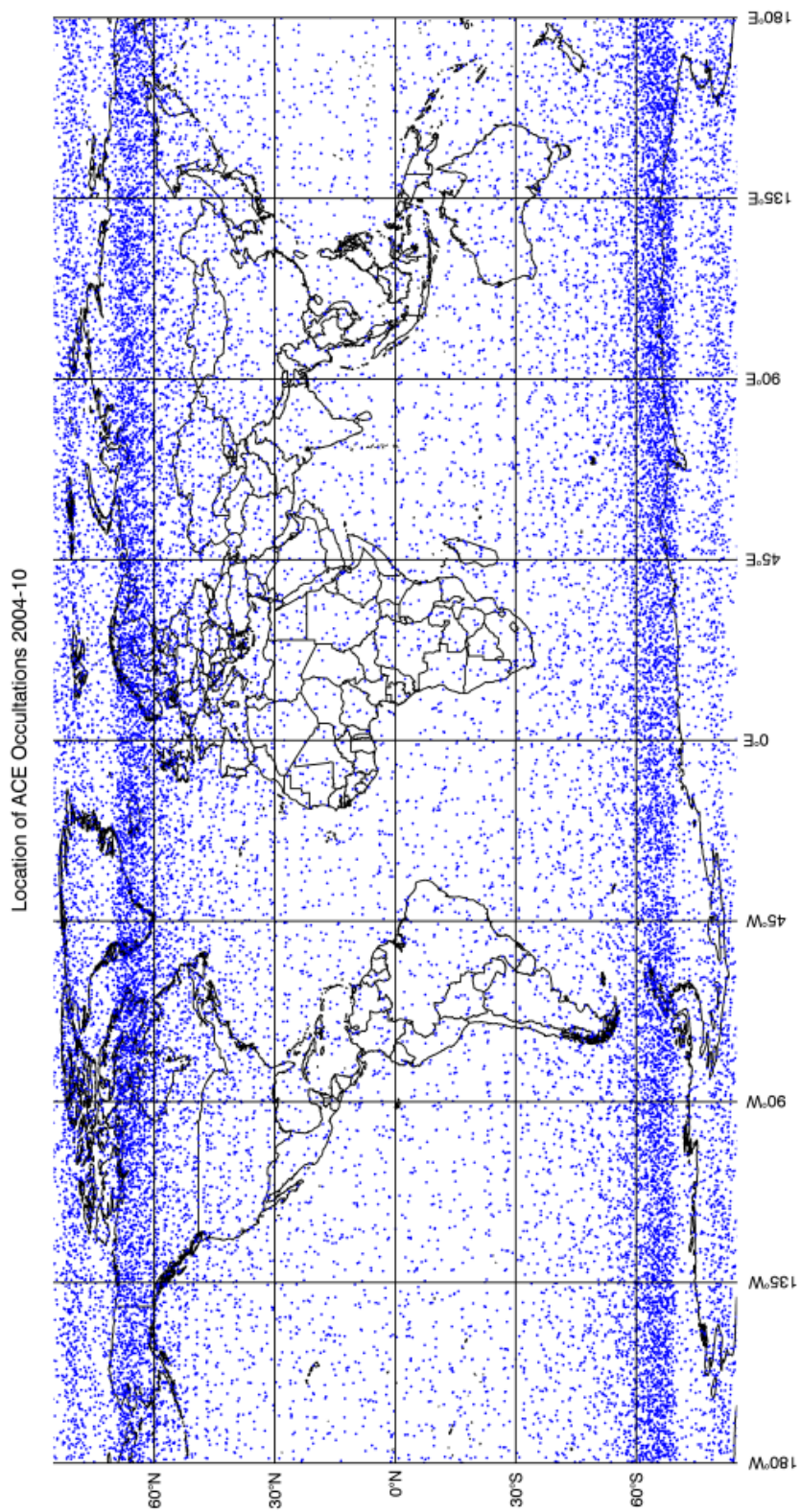


Figure 23. Locations of 25855 ACE-FTS occultations between March 2004 and October 2010 showing the global coverage of the instrument with a particularly large number of measurements at high latitudes. (Beale *et al.*, 2016a).

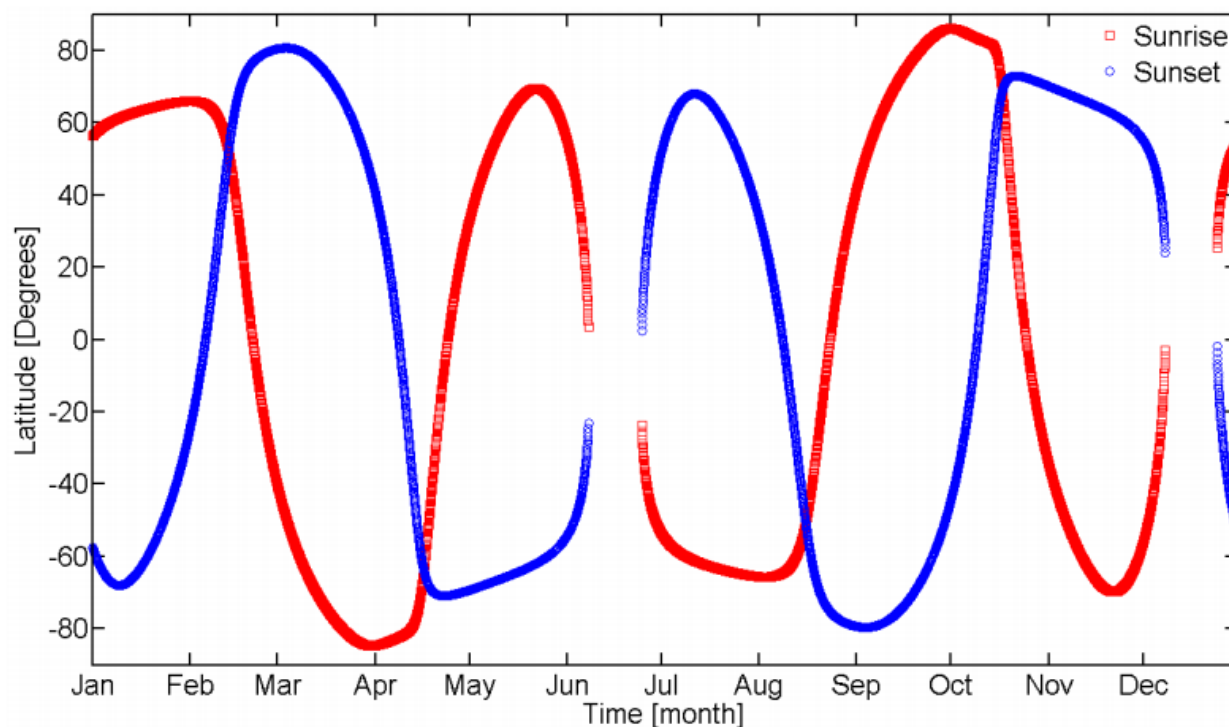


Figure 24. Latitudinal coverage of SCISAT for one year. Each circle represents one occultation.

Figure from *Jones et al. (2012)*.

In version 3.0, the CO VMR profile in the thermosphere was assumed to be increasing rapidly with altitude, which yielded an overestimation of the contribution to the calculated spectrum from the altitude region above the highest analyzed measurement (~110 km). In version 3.5, a constant VMR was assumed above the highest analyzed measurement.

The spectral microwindows employed in the CO and ^{13}CO retrievals are presented in Tables 3 and 4, respectively. The ACE-FTS measurements cover the 1-0 and 2-0 CO vibration-rotation bands, both of which are included in the ^{12}CO microwindow set, with the weaker 2-0 band used for low altitudes where many of the lines in the 1-0 band are saturated. The microwindow set for the ^{13}CO

isotopologue only contains lines from the fundamental band. Unlike the main isotopologue, lines in the 1-0 band for ^{13}CO do not saturate in the low-altitude ACE-FTS spectra thanks to the lower atmospheric abundance compared to ^{12}CO . At low altitudes, microwindows with relatively weak CO lines must be used as strong lines will be saturated (making determination of line intensity and therefore concentration difficult or even impossible). At high altitudes as atmospheric pressure decreases so (generally) does the concentration of gas. As a result, the microwindows used for high altitudes include lines that are more intense than those used at lower altitudes.

Table 3. List of microwindows used for ^{12}CO retrievals (ACE-FTS version 3.5 data product).

Table from *Beale et al.* (2016a).

| Center Frequency (cm^{-1}) | Microwindow Width (cm^{-1}) | Lower Altitude (km) | Upper Altitude (km) |
|---|--|--------------------------------------|--------------------------------------|
| 1950.10 ^[1] | 0.35 | 7 | 15 |
| 1986.09 ^[1] | 0.30 | 6-7 | 22 |
| 2033.08 ^[1] | 0.30 | 5 | 8 |
| 2046.29 | 0.24 | 8 | 25 |
| 2050.90 | 0.30 | 20 | 45 |
| 2081.88 | 0.48 | 13-15 | 100 |
| 2083.05 ^[1] | 0.70 | 5 | 15 |
| 2086.36 | 0.40 | 15 | 100 |
| 2094.76 | 0.40 | 70 | 110 |
| 2098.97 | 0.50 | 40 | 110 |
| 2107.46 | 0.40 | 60 | 110 |
| 2115.50 | 0.60 | 40 | 110 |
| 2119.70 | 0.50 | 70 | 110 |
| 2131.65 | 0.50 | 18 | 105 |
| 2135.40 | 1.00 | 14-16 | 105 |
| 2139.35 | 1.00 | 13-15 | 105 |

Table 3. continued

| | | | |
|------------------------|------|-------|-----|
| 2140.00 | 1.25 | 5 | 22 |
| 2140.80 ^[1] | 0.60 | 5 | 22 |
| 2146.75 | 1.00 | 5 | 22 |
| 2147.05 | 0.90 | 13-15 | 105 |
| 2149.75 ^[1] | 0.60 | 5 | 15 |
| 2150.90 | 0.70 | 16-17 | 105 |
| 2154.65 | 0.80 | 17-18 | 110 |
| 2158.30 | 0.50 | 19 | 110 |
| 2161.95 | 0.50 | 20 | 110 |
| 2164.00 ^[1] | 0.50 | 10 | 20 |
| 2165.48 | 0.55 | 20 | 110 |
| 2169.13 | 0.55 | 20 | 110 |
| 2172.68 | 0.50 | 50 | 110 |
| 2176.25 | 0.45 | 20 | 110 |
| 2179.85 | 0.40 | 60 | 110 |
| 2183.20 | 0.40 | 40 | 110 |
| 2186.60 | 0.40 | 60 | 110 |
| 4209.38 | 0.40 | 5 | 15 |
| 4222.90 | 0.45 | 5 | 15 |
| 4227.37 | 0.70 | 5 | 15 |
| 4236.01 | 0.45 | 5 | 15 |
| 4248.34 | 0.40 | 5 | 15 |
| 4274.77 | 0.30 | 5 | 15 |
| 4285.10 | 0.55 | 5 | 15 |

[1] Microwindow contains no information on the target. Used to improve the retrieval of interferers.

Table 4. List of microwindows used for ^{13}CO retrievals (ACE-FTS version 3.5 data product)Table from *Beale et al.*, (2016a).

| Center Frequency (cm^{-1}) | Microwindow Width (cm^{-1}) | Lower Altitude (km) | Upper Altitude (km) |
|---|--|--|--|
| 1446.50 ^[1] | 0.35 | 30 | 50 |
| 1649.34 ^[1] | 0.30 | 20 | 30 |
| 1950.10 ^[1] | 0.35 | 5-7 | 20 |
| 1977.66 ^[1] | 0.60 | 5-7 | 22 |
| 1986.09 ^[1] | 0.30 | 5-7 | 22 |
| 2020.90 | 0.40 | 5-8 | 12 |
| 2024.90 | 0.40 | 5 | 12 |
| 2033.37 | 0.30 | 5 | 15 |
| 2045.67 | 0.35 | 12 | 20 |
| 2045.90 | 0.40 | 50 | 85 |
| 2049.42 | 1.00 | 50 | 85 |
| 2049.92 | 0.40 | 12 | 50 |
| 2053.74 | 0.40 | 50 | 85 |
| 2057.80 | 0.30 | 15 | 50 |
| 2058.05 | 0.50 | 50 | 90 |
| 2061.57 | 0.70 | 50 | 90 |
| 2061.87 | 0.35 | 12 | 50 |
| 2065.82 | 0.40 | 50 | 90 |
| 2069.60 | 0.26 | 20 | 90 |
| 2073.38 | 0.55 | 50 | 90 |
| 2077.45 | 0.50 | 60 | 90 |
| 2081.60 | 1.00 | 45 | 90 |
| 2084.98 | 0.40 | 10 | 90 |
| 2088.77 | 0.40 | 45 | 90 |
| 2092.43 | 0.30 | 12 | 20 |
| 2103.32 | 0.40 | 45 | 90 |

Table 3. continued

| | | | |
|---------|------|-----|----|
| 2107.15 | 0.70 | 55 | 90 |
| 2111.0 | 1.25 | 50 | 90 |
| 2113.95 | 0.40 | 50 | 90 |
| 2117.35 | 0.35 | 55 | 90 |
| 2120.90 | 0.35 | 55 | 90 |
| 2124.00 | 0.80 | 60 | 90 |
| 2127.65 | 0.30 | 60 | 90 |
| 2131.34 | 1.00 | 40 | 90 |
| 2134.35 | 0.35 | 45 | 90 |
| 2137.60 | 0.30 | 5-7 | 85 |
| 2140.80 | 0.60 | 5 | 40 |
| 2144.10 | 0.40 | 5 | 45 |
| 2147.10 | 0.40 | 20 | 40 |
| 2153.28 | 0.45 | 5 | 12 |
| 2159.60 | 0.40 | 5-7 | 12 |

[1] Microwindow contains no information on the target. Used to improve the retrieval of interferers.

ISOTOPIC EFFECTS ON INFRARED SPECTRA

The vibrational energy of a molecule is related to the masses of the atoms in that molecule (Equation 9). When a neutron is added to the nucleus of an atom in a molecule, as is the case with a heavier isotopologue, the vibrational energies change. The vibrational energy is inversely proportional to the square root of the reduced mass, as such the vibrational band center of the heavier isotopologue is at a lower energy than a lighter one. The vibrational band centers for ^{12}CO and ^{13}CO are given in Table 3. Carbon monoxide, being a diatomic molecule only has one vibrational mode (Figure 25).

Table 5. Vibrational band centers of ^{12}CO (*Mina-Camilde et al.*, 1996) and ^{13}CO (*Chen et al.*, 1976).

| Isotopologue | 1-0 band center (cm^{-1}) | 2-0 band center (cm^{-1}) |
|------------------|--------------------------------------|--------------------------------------|
| ^{12}CO | 2146.9 | 4263.2 |
| ^{13}CO | 2099.71 | 4170.43 |

The rotational energy expression (Equation 7) is also dependent on the mass of the atoms in the molecules (by Equation 1). As such the infrared transitions and therefore the rotational-vibrational spectrum of a heavier (or indeed lighter) isotopologue is different from the most common form of that molecule. The rotational constant, B , is inversely proportional to the reduced mass and therefore the line spacing (given by $2B$) is lower for a heavier isotopologue than a lighter one. For ^{12}CO the rotational line spacing is 3.842 cm^{-1} , for ^{13}CO this is equal to 3.673 cm^{-1} .

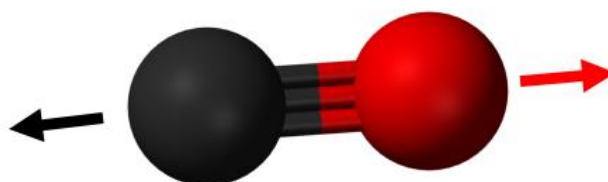


Figure 25. The stretching mode for carbon monoxide. Figure adapted from

<https://commons.wikimedia.org/wiki/File:Carbon-monoxide-3D-balls.png>, accessed July 8 2017.

Different isotopologues are obtained from the ACE-FTS independently as if they are separate molecules and their volume mixing ratios are provided at 1 km vertical intervals. The infrared contains many isolated lines for the various isotopologues. Accurate spectroscopic line data are required as fractionation is often rather small so that errors in spectroscopic data can lead to much larger errors in the δ -values calculated (Equation 18). Total CO concentration measurements have been validated (Clerbaux *et al.*, 2008) and the δ -values obtained from ACE have been compared to independent *in situ* measurements in the troposphere and the agreement between the values was within 5%.

Due to the number of molecules in the atmosphere with active infrared transitions, there are a number of interfering molecules in the CO microwindows. The vertical profiles of these interfering molecules are determined simultaneously. As isotopologues of molecules generally have different profiles, a separate profile is used for each interfering isotopologue. Where the contribution of an interfering molecule to a particular microwindow is relatively weak, additional microwindows with information about the interfering molecule (rather from the CO isotopologue) are used. If the contribution from an interferer is too small, the least squares fit may not converge. For the main isotopologue, the interferers in the version 3.5 microwindow set were H_2^{16}O , H_2^{17}O , CO_2 , $^{18}\text{O}^{12}\text{C}^{16}\text{O}$, $^{17}\text{O}^{12}\text{C}^{16}\text{O}$, O_3 , $^{18}\text{O}^{16}\text{O}^{16}\text{O}$, N_2O , ^{15}NNO , N^{15}NO , ^{13}CO , C^{18}O , CH_4 , and OCS . For ^{13}CO , the interferers were H_2^{16}O , H_2^{18}O , H_2^{17}O , CO_2 , $^{13}\text{CO}_2$, $^{18}\text{O}^{12}\text{C}^{16}\text{O}$, $^{17}\text{O}^{12}\text{C}^{16}\text{O}$, O_3 , $^{18}\text{O}^{16}\text{O}^{16}\text{O}$, $^{16}\text{O}^{18}\text{O}^{16}\text{O}$, $^{17}\text{O}^{16}\text{O}^{16}\text{O}$, $^{16}\text{O}^{17}\text{O}^{16}\text{O}$, N_2O , ^{12}CO , C^{18}O , CH_4 , and OCS . The ACE retrievals used in this work were carried out by Chris Boone at the University of Waterloo.

An extensive validation of ACE measurements, using satellite, airborne and ground-based data, of total CO from the 2.2 dataset has been provided by Clerbeaux *et al.*, (2008) and this work showed the retrieval error for the main isotopologue to be within 5% from the upper troposphere to 40 km

and 10% above 40 km. The ACE-FTS may therefore be considered as a reliable platform for CO measurements in the atmosphere from 8-110 km. The ^{13}CO retrieval has not been formally validated yet, except for tropospheric comparisons.

Table 6. The fractionation effects (with respect to V-PDB) of the four main tropospheric CO sources (Adapted from *Brenninkmeijer et al.*, (1999) and sources therein).

| Source | Amount Tg/year | $\delta^{13}\text{C}$ (‰) |
|------------------------|----------------|---------------------------|
| Fossil fuel combustion | 300-550 | -27.5 |
| Biomass burning | 300-700 | -21.3/-24.5 |
| Methane oxidation | 400-1000 | -52.6 |
| NMHC oxidation | 200-600 | -32.2 |

WACCM

The Whole Atmosphere Community Climate Model (WACCM) is an atmospheric component of the Community Earth System Model (*Marsh et al.*, 2013) developed by the National Center for Atmospheric Research (NCAR) to include interactive chemistry, radiation and dynamics (*Verronen et al.*, 2016). WACCM spans from the Earth's surface up to 5×10^{-6} hPa (approximately 140 km, in the thermosphere) which fully covers the altitude range of ACE retrievals for ^{12}CO , ^{13}CO , C^{17}O and C^{18}O . The native WACCM resolution is 1.9° latitude by 2.5° longitude, but for this work WACCM was used with a resolution of 4° latitude by 5° .

WACCM has no in built support for isotopic chemistry, but it is fully interactive and isotopologues may be input as separate species, with rate constants for their various reactions differing from the main isotopologues as given by the kinetic isotope effect (Table 7). Many kinetic isotope effects are temperature and pressure dependent. This dependency was not included in the model runs and will introduce small errors in the results at the surface, increasing with altitude as the atmospheric temperature and pressure changes. From initial conditions WACCM was run for 20 years, with years 18, 19 and 20 being used for data collection.

Table 7. List of major reactions for CO in the atmosphere with their related kinetic isotope effects k_{12}/k_{13} . All KIEs for the chemical reactions are reported at 298 K and 1 atmosphere pressure. CO₂ photolysis is reported at 295 K.

| Reactants | Products | k_{12}/k_{13} | Source |
|-------------------------------------|---|-----------------|---------------------------------|
| CH ₄ + OH | CH ₃ O ₂ + H ₂ O | 1.00288 | (Sander <i>et al.</i> , 2011) |
| CH ₃ Cl + Cl | HO ₂ + CO + 2 HCl | 1.07 | (Gola <i>et al.</i> , 2005) |
| CH ₂ O + NO ₃ | CO + HO ₂ + HNO ₃ | 0.96 | (Feilberg <i>et al.</i> , 2004) |
| CH ₂ O + OH | CO + H ₂ O + H | 0.952 | (Feilberg <i>et al.</i> , 2004) |
| CH ₂ O + Br | HBr + HO ₂ + CO | 1.13 | (Feilberg <i>et al.</i> , 2004) |
| CH ₂ O + Cl | HCl + HO ₂ + CO | 1.058 | (Feilberg <i>et al.</i> , 2004) |
| CO + OH + M | CO ₂ + HO ₂ + M | 1.00597 | (Röckmann <i>et al.</i> , 1998) |
| CO ₂ + hv | CO + O | varies | (Schmidt <i>et al.</i> , 1996) |

The major source of CO at high altitudes in the photolysis of carbon dioxide (CO₂). The fractionation effect of CO₂ photolysis is dependent on the wavelength of the light. Above 150 nm theoretical values for the cross-sections are used (*Schmidt et al.*, 2013). Below 150 nm there only exists cross-section data for the ¹²C¹⁶O isotopologue, experimental values for these cross-sections (*Yoshino et al.*, 1996) are used for both isotopologues.

Isotopic fractionation data for CO surface emissions are available and these were added to WACCM. WACCM natively includes boundary conditions for CH₄, although the heavy isotopologues of these molecules were added. The NOAA ESRL Carbon Cycle Cooperative Global Air Sampling Network (*Novelli and Masarie*, 2014) collects surface CO concentrations and these values were interpolated over all latitudes. For the heavy isotopologue, ¹³CO boundary conditions were calculated using δ¹³C measurements from *Bergamaschi et al.* (2000). δ¹³C relations for methane (CH₄) and CO₂ were derived by Eric Buzan from experimental data by *Rockmann et al.* (2011), and *Assamov et al.* (2010):

$$\delta^{13}C (CH_4)/\text{‰} = \frac{1.29 \times 10^4}{[CH_4]/(\text{ppm})} - 151.4 \quad (19)$$

$$\delta^{13}C (CO_2)/\text{‰} = \frac{6.47 \times 10^3}{[CO_2]/(\text{ppm})} - 25.3. \quad (20)$$

These were combined with boundary condition data (*Lamarque et al.* 2010) from WACCM to calculate boundary conditions for each isotopologue.

RESULTS FOR ^{13}CO

A total of 25855 occultations containing concentrations of ^{12}CO and ^{13}CO were successfully obtained. Physically unrealistic data are removed from the data product of the obtained occultations. Quality flags are assigned to the data based on a statistical fitting and outliers, which may be due to instrumental or processing errors (*Sheese et al.*, 2015); these quality flags are available as part of the ACE data products. Data with quality flags of 1 were accepted, individual data with quality flags of 2 or greater, or any occultation containing any data with quality flags of 4, 5 or 6 were rejected. The accepted occultations are grouped into one of eighteen 10° latitude bins. The data are further binned by altitude (1 km bins). The global distribution of the total concentration of CO by season can be seen in Figure 22. The $\delta^{13}\text{CO}$ values from ACE are calibrated by comparing subtropical values at 8-10 km with $\delta^{13}\text{CO}$ values at the same latitude and altitude from aircraft transects in the troposphere obtained by *Mak and Brenninkmeijer* (1998). A calibration factor of 0.99582 was applied to the ACE ^{13}CO concentrations in order to match the satellite and in situ $\delta^{13}\text{CO}$ values. This factor is likely due to a small inconsistency between the ^{12}CO and ^{13}CO line intensities. VMRs of around 100 ppb in the troposphere, decreasing to between 20 and 50 ppb in the stratosphere can be seen and these results are consistent with previous satellite measurements (*Clerbaux et al.*, 2008). The large production by photolysis of CO_2 at high altitudes can clearly be seen, as can the dynamics of the air masses between the seasons. Another interesting feature is the asymmetrical distribution of CO between the Northern and Southern Hemispheres in the troposphere, with higher CO concentrations in the Northern Hemisphere being expected because of the larger emissions and *in situ* formation.

There is a distinct hemispheric and seasonal disparity in the distribution of CO in the atmosphere (Figure 22). This is caused by atmospheric dynamics, specifically the upwelling of tropical air

(Brewer-Dobson circulation) and the downwelling of air from the upper mesosphere and thermosphere in the polar regions in the winter. This effect can be seen more clearly in our WACCM results. The effect of this is that during winter months, CO from UV photolysis of CO₂ in the thermosphere descends into the stratosphere where the concentration of CO at a particular altitude is higher than other latitudes by a factor of ten or more. Ground-based FTIR measurements (*Velazco et al.*, 2007) show the rapid change of CO column densities by season with increased CO in the winter in each hemisphere with the greatest changes coming at high latitudes.

Figure 26 shows how the isotopic fractionation of ¹³CO varies by season. The bands of highly positive fractionation near 10 km and 40-50 km are most likely due to systematic errors in the CO VMR retrievals in the vicinity of those altitudes. Although seemingly a problem, these results highlight the sensitivity of our method. The individual atmospheric concentration profiles of CO isotopologues from the ACE-FTS (*Clerbaux et al.*, 2008) do not show any glaring errors, but this analysis shows that isotopic fractionation can be used to diagnose problems in the retrievals from satellite observations. Although the VMR of formaldehyde (CH₂O) peaks in the troposphere and at around 40 km (*Vigouroux et al.*, 2009; *Ricaud et al.*, 2007) which could explain a slight positive fractionation as oxidation of formaldehyde favors ¹³CO production over ¹²CO (*Feilberg et al.*, 2004). However, the apparent enhanced fractionation near 40 km seen in Figure 26 is very high, exhibits a suspiciously flat variation with latitude, and no such feature is seen in our WACCM results, all of which suggests that the feature is an artifact.

The positive fractionation observed at 20-30 km, just above the tropical and subtropical tropopause, is another noticeable feature in all seasons. Perhaps this positive fractionation is indicative of the reaction of CO with OH, which will fractionate the air mass by preferentially removing the lighter isotope and therefore the remaining CO has a higher relative abundance of

^{13}CO . This kinetic isotope effect has a small positive value of 5‰ (Brenninkmeijer *et al.*, 1999) (Table 7).

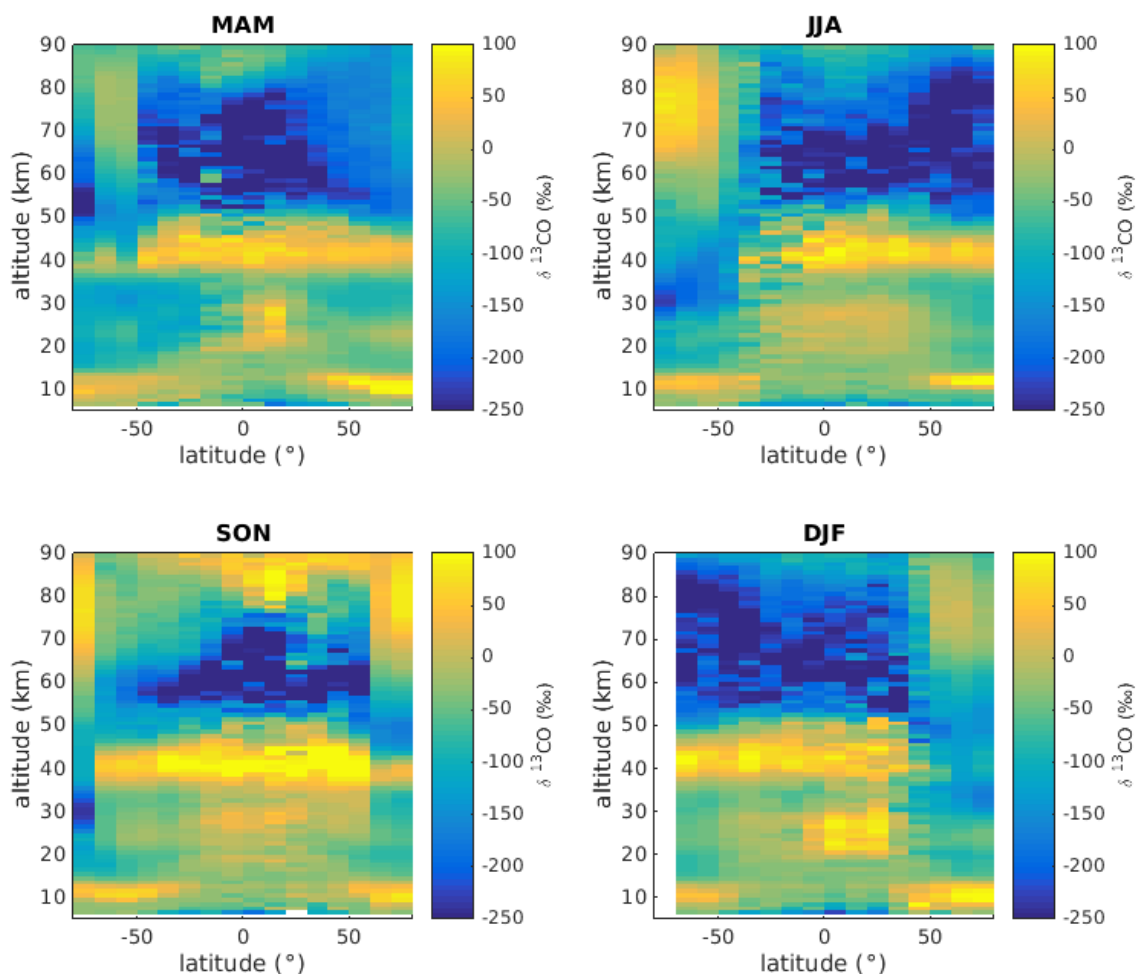


Figure 26. Seasonal variation of $\delta^{13}\text{CO}$ as a function of latitude between 8 and 90 km from the ACE-FTS (Beale *et al.*, 2016a).

Outside of the tropics and subtropics, the CO has the fractionation signature of that created by the oxidation of methane of -52.5‰ (Table 6). This latitudinal dependence is not observed in WACCM, where the entire stratosphere has the isotopic signature of CO formed by the oxidation of methane. Unlike the features at 40 km, the observations in the tropics do not exhibit features

that are typical of a retrieval error and it is likely that these results show a real fractionation effect in the atmosphere not modelled by WACCM. Indeed, the concentrations of CO in the atmosphere are at their lowest in this region (Figure 22) so it is expected that the isotopic signature of CO in the tropics will be highly dependent on its oxidation by OH.

The fractionation of CO isotopologues in the mesosphere varies spatially and seasonally; in general, the values are highly negative around 60 km and positive at 80 km and higher. CO at high altitudes is primarily formed from photolysis of CO₂. Photolysis of CO₂ from UV light between 167 nm and 210 nm is the main source of CO in the mesosphere and lower thermosphere (MLT) (*Schmidt et al.*, 2013). This photolysis has a very high fractionation effect and given the increase of UV radiation in the respective summers, explains the highly negative values in the MLT shown in Figure 26 in the summer, where the air is subjected to UV radiation and therefore photolysis. Indeed, in a simulated photolysis experiment *Schmidt et al.* (2013) found ¹²CO₂ to photolyze much faster than ¹³CO₂, leading to ¹²CO enrichment, in agreement with ACE observations. However, downwelling from the thermosphere in the winter results in CO that is enriched in ¹³CO (positive δ value) to descend into the mesosphere and even in the upper stratosphere as seen in the southern hemisphere in JJA and the northern hemisphere in DJF (Figure 22). In the winter, the air at these latitudes is subject to much less photolysis as it receives little sunlight and as a result the highly negative fractionation observed in other seasons does not occur.

WACCM results in Figure 27 represent the observed data well in the mesosphere. The tropospheric values of WACCM are consistent with in situ measurements (*Kato et al.*, 2000; *Röckmann et al.*, 2002; *Mak et al.*, 2003) and are less variable than the ACE-FTS data at low altitudes. The observed fractionation at 40-50 km is not seen in Figure 27, but the evidence of the effect of dynamics (which WACCM includes) on the distribution of CO fractionation is. As with CO concentrations,

this is best viewed as a month by month animation, but winter descent as part of the polar vortex can be seen in the upper right and lower right panels of Figure 27. Although the trend of fractionation is similar to ACE-FTS results, the strength of fractionation is different between the two results with ACE results showing much higher depletion of ^{13}CO in the lower and middle mesosphere.

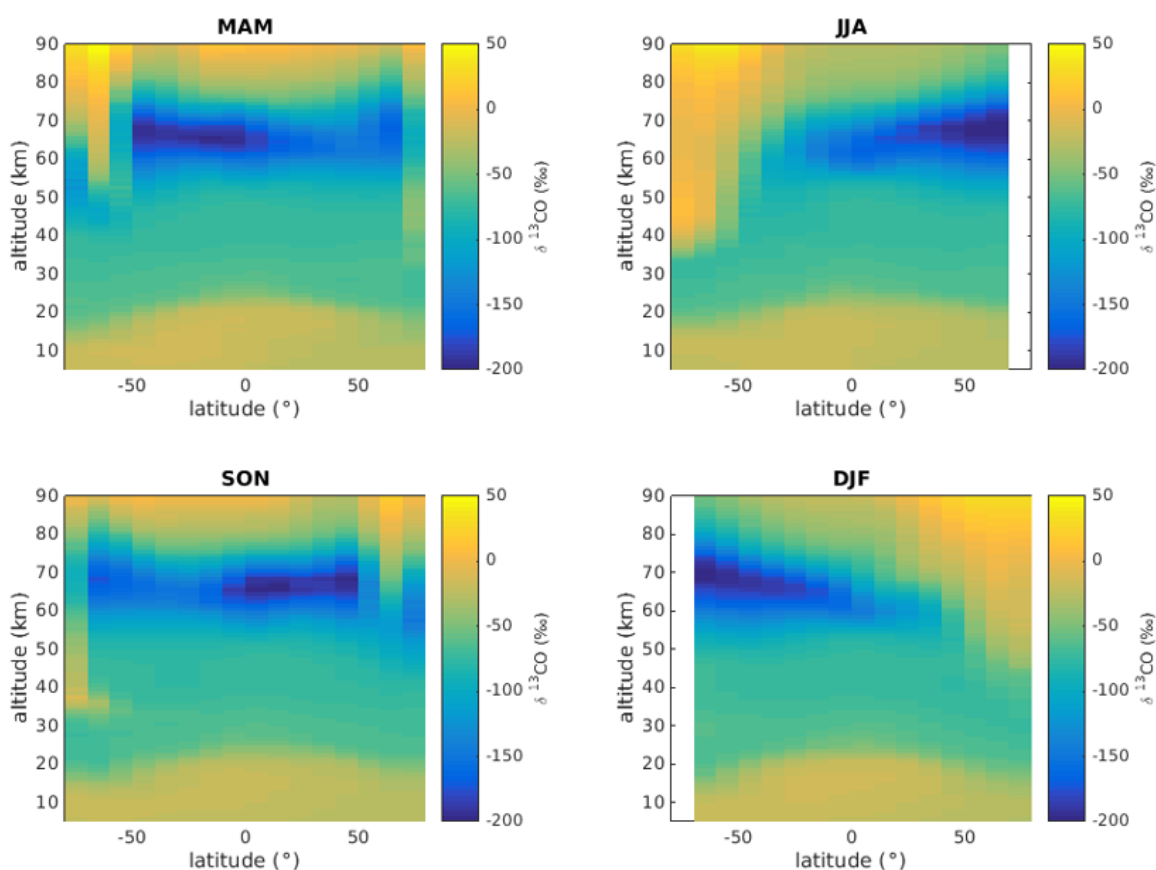


Figure 27. Seasonal variation of $\delta^{13}\text{CO}$ as a function of latitude between 0 and 90 km from WACCM (Beale *et al.*, 2016a).

Figure 28 shows the difference between $\delta^{13}\text{CO}$ determined from ACE measurements and WACCM. The band of high fractionation at 40-50 km and the smaller positive fractionation in the

tropical stratosphere at 20-30 km, which were not shown from WACCM, are highlighted in Figure 28. The band at 40-50 km is likely due to an artefact in the retrieval process.

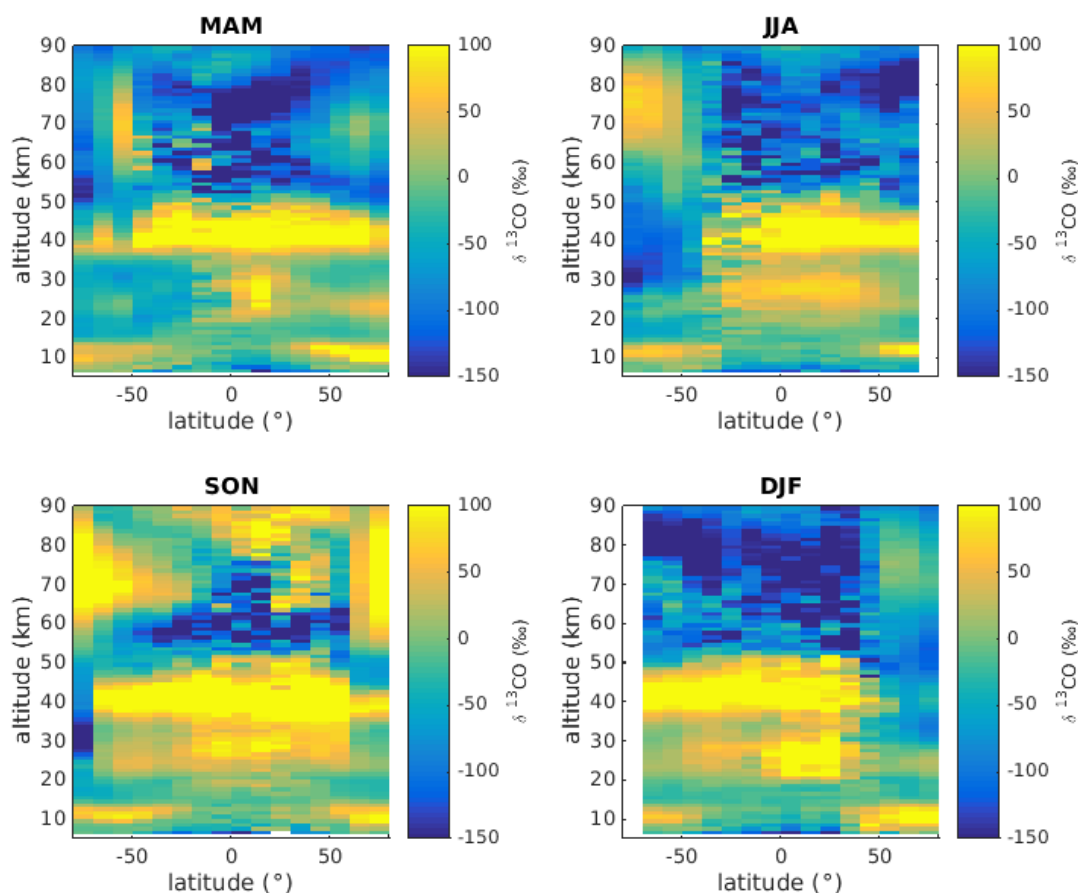


Figure 28. Difference between ACE measurements of $\delta^{13}\text{CO}$ and WACCM output (*Beale et al.*, 2016a).

The residuals in the mesosphere show that our WACCM runs underestimate fractionation in that region of the atmosphere. Although our treatment of CO_2 photolysis is not comprehensive, due to the fact that isotopic dependent cross-sections are not available for all wavelengths, appropriate cross-sections have been used where possible. This first attempt to model ^{13}CO in the atmosphere

is at least semi-quantitative. Indeed the differences between WACCM and ACE shown in Figure 28 at high altitudes may be due to our inability to implement correct cross-section data below 150 nm or at the appropriate temperatures or pressures. These isotopic measurements suffer from very high levels of noise, due to the difficulty in accurately determining the ^{13}CO concentration from very weak absorption lines and interfering lines in the microwindows used. Disagreement between the model results and observations in the tropics at 20-30 km may be due to missing isotopic chemistry of hydrocarbons in the stratosphere. The oxidation of hydrocarbons plays an important role in the cycling of carbon in this region of the atmosphere although fractionation values are only available for methane, the simplest hydrocarbon.

There have been a number of studies of CO isotopic fractionation on the surface of the Earth. ACE has coverage of CO in the troposphere, although spectral congestion in the low atmosphere results in measurements at the surface being less accurate than those higher in the troposphere. As the troposphere is relatively well mixed, ACE $\delta^{13}\text{CO}$ values from the higher troposphere may be compared to surface measurements. In the sub tropics, the average $\delta^{13}\text{CO}$ value from ACE in the troposphere is -32 ‰. Measurements from Mount Sonnblick, Austria (47° N) have $\delta^{13}\text{CO}$ values ranging between -25 and -30 ‰, (*Gros et al.*, 2001), from Happo, Japan (37° N) have values between -24 and -29 ‰ (*Kato et al.*, 2000) and a transect across the Trans-Siberian Railroad had values ranging between -26 to -29.5 ‰ (*Tarasova et al.*, 2007). These measurements were used to independently validate the ACE $\delta^{13}\text{CO}$ values and provided satisfactory agreement.

ISOTOPIC FRACTIONATION OF C¹⁷O AND C¹⁸O

The ACE-FTS data set also includes retrievals of two oxygen isotopologues of carbon monoxide, namely C¹⁷O and C¹⁸O. The relative abundance of the oxygen isotopologues (Table 8) are much lower than that of ¹³CO, making retrievals much more difficult. As a result of this, the altitudinal range of C¹⁷O and C¹⁸O measurements and therefore fractionation is much lower.

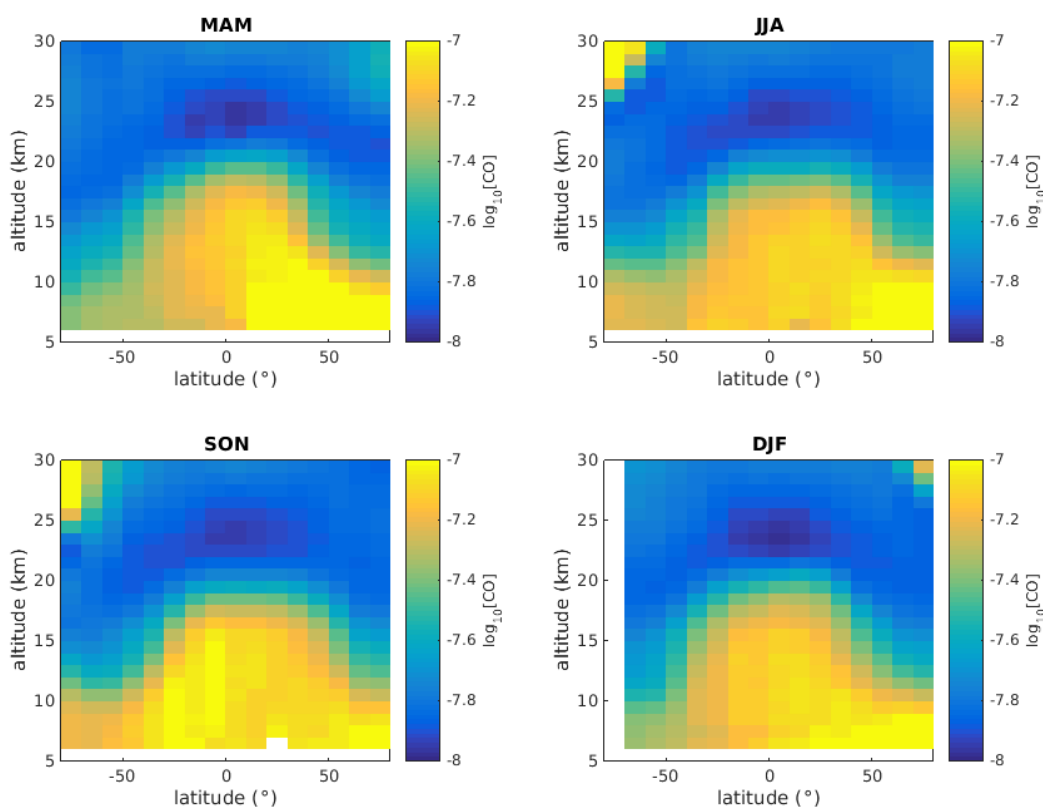


Figure 29. Total CO volume mixing ratios from 6-30 km as measured by the ACE-FTS.

As the altitude ranges for the oxygen isotopologues ranges only up to the lower-mid stratosphere, the total CO concentrations as measured by the ACE-FTS shown in Figure 22 up to 90 km are reproduced in Figure 29 up to 30 km.

The fractionation of $C^{17}O$ shown in Figure 30 suffers from low altitude coverage. However, some trends are identifiable. Fractionation generally increases with CO concentration above 20 km at high latitudes and the very highest levels of fractionation follow the lower stratosphere just above the tropopause. The values for fractionation are believed to only be semi-quantitative. A quantitative analysis would require greater altitudinal coverage and higher quality retrievals. Such retrievals are not possible with current $C^{17}O$ molecular data.

Table 8. Summary of $C^{17}O$ and $C^{18}O$ abundance and retrieval ranges. Oxygen isotopic abundances are based on Vienna Standard Mean Ocean Water (SMOW).

| Molecule | Abundance | Altitude range (km) |
|-----------------|------------------------|----------------------------|
| $^{12}C^{16}O$ | 0.99757 | 5-110 |
| $^{12}C^{17}O$ | 3.799×10^{-4} | 8-25 |
| $^{12}C^{18}O$ | 2.005×10^{-3} | 5-30 |

$C^{18}O$ fractionation shown in Figure 31 is of higher quality than that of $C^{17}O$, mostly due to the higher fractional abundance (Table 8). Seasonal trends are shown with this dataset with highly negative fractionation above 25 km in the Northern Hemisphere summer (JJA) and the Southern Hemisphere summer (DJF) and conversely fractionation of approximately zero in each hemisphere's winter at this altitude. Comparison with the ^{13}CO isotopologue in Figure 26 at this

altitude shows that this fractionation is qualitatively opposite. There is also more positive fractionation in the summer of each hemisphere at 6-12 km.

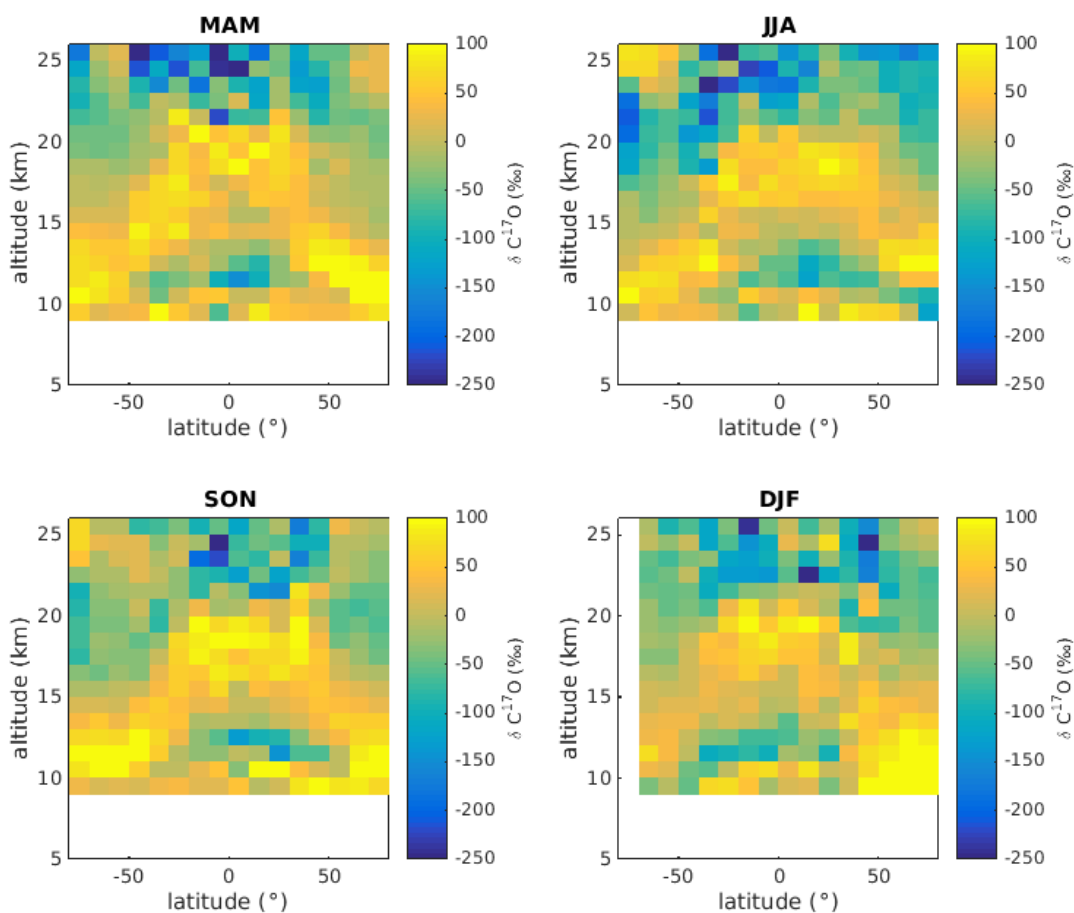


Figure 30. Isotopic fractionation of $C^{17}O$ from 9-25 km.

The primary cause of fractionation in the oxygen isotopologues of CO in the lower atmosphere is the reaction of ozone (O_3) with hydrocarbons, specifically terpenes and isoprene emitted by plants (Röckmann *et al.*, 1998). This reaction produces CO with the same ^{18}O fractionation as the O_3 from which it was made of 25-40 ‰ (Krankowsky *et al.*, 1995). Seasonally, concentrations of CO are highest in winter as removal by OH is reduced. As sources are greater than the sink in winter, the

isotopic makeup of CO reflects those of the sources, in the Northern Hemisphere this is mainly fossil fuels, which have a high value for $\delta^{18}\text{C}$ (Röckmann and Brenninkmeijer, 1997). As with data for C^{17}O , the results for C^{18}O are most likely not quantitatively correct. These data have not been validated by *in situ* measurements throughout the atmosphere. Ground based fractionation results are available, and tropospheric values from ACE were compared to generally validate these results.

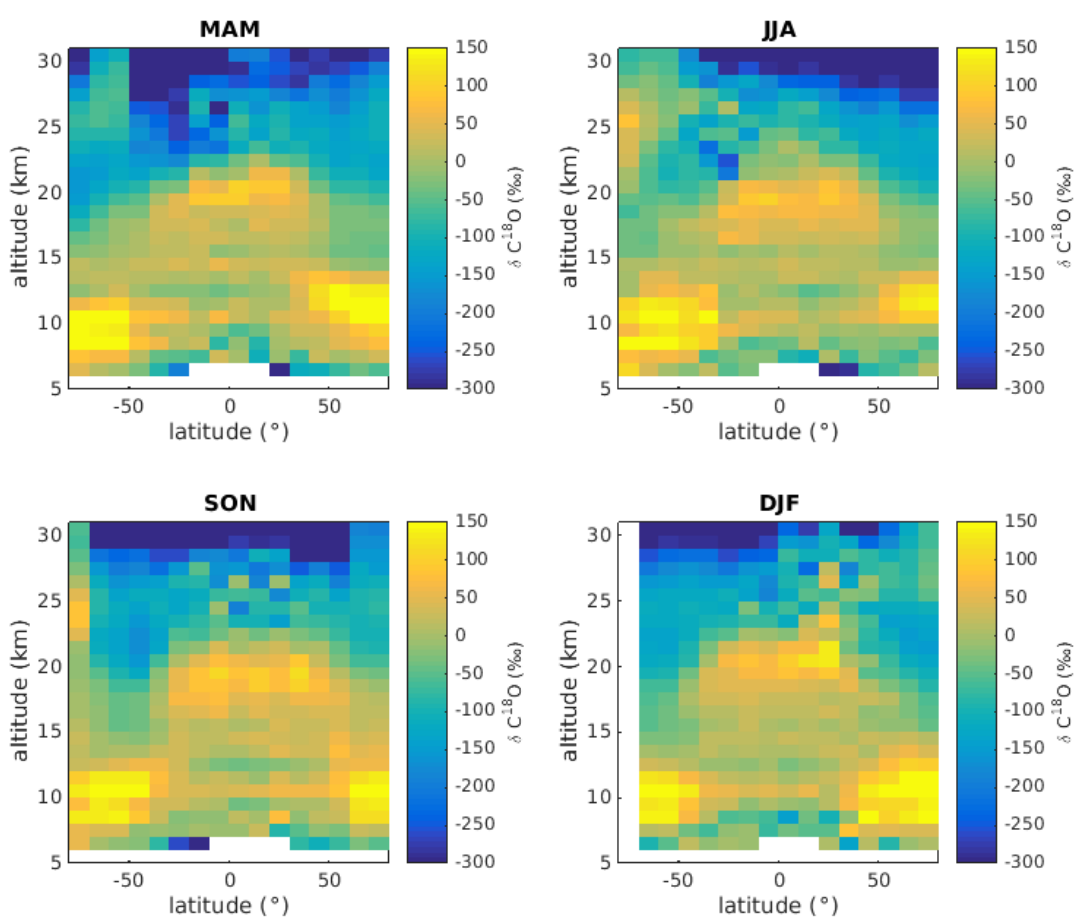


Figure 31. Isotopic fractionation of C^{18}O from 6-30 km.

CONCLUSION

This chapter presents the first near global atmospheric data set of the isotopic fractionation of CO based on infrared remote sensing measurements from orbit. The advantage of measuring the various isotopologues of CO is that δ values identify the particular chemical or physical source. The satellite observations and model results show the high concentrations of ^{13}CO in winter to have descended from the thermosphere. The ACE instrument is a useful tool to study the seasonal variation in atmospheric dynamics and may be used to analyze the isotope chemistry of the upper atmosphere. Observations of C^{17}O and C^{18}O fractionation are also presented. C^{17}O is limited coverage and data quality to enable any substantial analysis; however C^{18}O fractionation allows a quantitative comparison with chemical reactions affecting CO fractionation trends in the troposphere and lower stratosphere.

CHAPTER V

PROPANE CROSS-SECTIONS IN THE 3 μm REGION

The results presented in Chapter V have been published in the Journal of Quantitative Spectroscopy and Radiative Transfer (*Beale et al.*, 2016b). The co-authors for this paper were Robert Hargreaves (Old Dominion University, now University of Oxford) and Peter Bernath (Old Dominion University). Hargreaves assisted with the recording of the data, as propane is a flammable gas which is dangerous at high temperatures, more than one person is required in the laboratory when recording spectra for safety purposes. Bernath was the overall project PI who guided the research. As primary author of the paper, I took the lead on experimental setup (including selection of temperature range, number of scans), was the primary collector of data and conducted all analysis, writing and production of figures for the journal article and also for this chapter (unless explicitly cited).

INTRODUCTION

Propane (C_3H_8) is the second most abundant non-methane hydrocarbon (NMHC) in the Earth's atmosphere after ethane (C_2H_6) (*Doskey and Gaffney*, 1992). Propane and the other NMHCs only have a small radiative forcing effect on the Earth's atmosphere. Nevertheless, the chemistry of these molecules has a significant impact on the troposphere through the reaction with the hydroxyl radical (OH), which leads to the formation of acetone. This reaction also leads to the production of peroxyacetyl nitrate (PAN) (*Harrison and Bernath*, 2010), which has a relatively long lifetime

in the upper troposphere where it acts as a reservoir for NO_x, a catalyst for the production of ozone (Tereszchuk *et al.*, 2013).

Propane has been identified in a number of Solar System objects. These include the atmospheres of Jupiter, from observations with the Galileo Probe Neutral Mass Spectrometer (Niemann *et al.*, 1998), and Saturn, using the TEXES instrument on NASA's Infrared Telescope Facility (Greathouse *et al.*, 2006). For both planets, emission features from the ν_{21} band (748 cm⁻¹) were detected (Greathouse *et al.*, 2006; Tokunaga *et al.*, 1983). Propane has also been detected on Titan, first in the stratosphere with infrared spectra from Voyager 1 (Maguire *et al.*, 1981; Hanel *et al.*, 1981; Kim and Caldwell, 1982) and more recently with TEXES (Roe *et al.*, 2003) and the CIRS instrument onboard Cassini (Nixon *et al.*, 2009; Coustenis *et al.*, 2007). Efforts to accurately quantify the propane concentration on Jupiter, Saturn and Titan have suffered from a lack of reliable spectroscopic data (Nixon *et al.*, 2009; Sung *et al.*, 2013) or laboratory spectra of sufficient resolution (Greathouse *et al.*, 2006) for the regions covered by these instruments. On board NASA's Juno mission (Matousek, 2007) is the Jovian Infrared Auroral Mapper (JIRAM) (Adriani *et al.*, 2008), which arrived at Jupiter in July 2016. The JIRAM spectrometer covers the 2-5 μm range and will be used to study hot emission in Jupiter's auroral regions that has been assigned to H₃⁺ and a number of hydrocarbon species (Adriani *et al.*, 2008). Although the JIRAM spectrometer has a relatively low spectral resolution, it has previously been shown (Nixon *et al.*, 2009) that recent high resolution propane spectra in the 7-15 μm region (Sung *et al.*, 2013) were crucial to accurately modelling the propane contribution in low resolution spectra of Titan (Figure 32) and thus enabling the detection of propene (C₃H₆) (Nixon *et al.*, 2013).

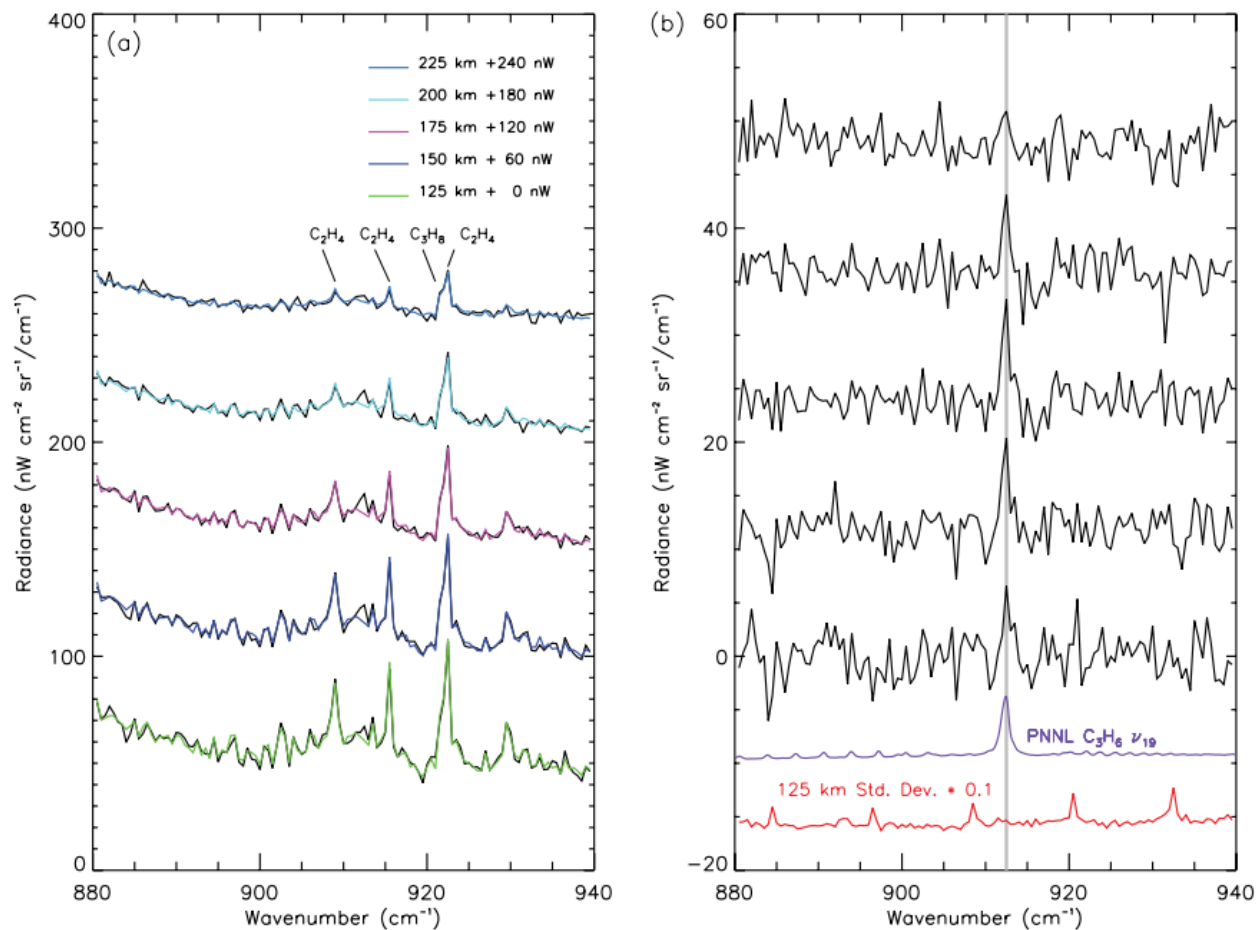


Figure 32. Detection of propene (unlabeled peak at 912.5 cm^{-1} in left panel) in Titan. This measurement relied on high resolution data to accurately model the other hydrocarbons present and observe C_3H_6 in the residual (right panel) (Nixon *et al.*, 2013).

The existence of propane and other hydrocarbons in the atmosphere of Jupiter, Saturn, Titan and other Solar System objects indicates the possibility of such molecules existing in the atmosphere of cool brown dwarfs and exoplanets. Methane (CH_4) has already been detected in exoplanet atmospheres (Swain *et al.*, 2008; Swain *et al.*, 2009) and a number of additional hydrocarbons, including propane, are predicted to exist in the atmospheres of such objects (Venot *et al.*, 2015; Lodders and Fegley, 2002). The relatively cool temperatures of brown dwarf atmospheres result in their spectra being dominated by molecular features. Models have predicted brown dwarf

atmospheres may include propane, although at much lower concentrations than methane or ethane (Lodders and Fegley, 2002). The atmospheres of hot Jupiters and brown dwarfs provide environments at elevated temperatures that could contain complex hydrocarbons such as propane. However, the laboratory data on which spectral models for these objects rely are incomplete or not recorded under the appropriate temperatures or pressures.

SPECTROSCOPY OF PROPANE

Propane, an asymmetric top molecule with C_{2v} symmetry (Lide, 1960), has been the subject of a number of spectroscopic studies. Of the 27 fundamental modes of propane detailed in *Shimanouchi* (1972), several have been studied in high resolution, including the ν_4 (a_1 , 1476 cm^{-1}), ν_{18} (b_1 , 1378 cm^{-1}), ν_{19} (b_1 , 1338 cm^{-1}), ν_{24} (b_2 , 1472 cm^{-1}) bands (Flaud *et al.*, 2001), the ν_9 band (a_1 , 369 cm^{-1}) (Kwabia Tchana *et al.*, 2010), the ν_{21} band (b_1 , 748 cm^{-1}) (Perrin *et al.*, 2015), the ν_{26} (b_2 , 748 cm^{-1}), $2\nu_{19}$ (a_1)- ν_{19} (b_1) (1338 cm^{-1}) and the cross-sections of the 690-1550 cm^{-1} region (Sung *et al.*, 2013) and 2550-3300 cm^{-1} (Harrison and Bernath, 2010). In the 3 μm region there are 8 C-H stretching modes (ν_1 (a_1), ν_2 (a_1), ν_3 (a_1), ν_{10} (a_2), ν_{15} (b_1), ν_{16} (b_1), ν_{22} (b_2) and ν_{23} (b_2)) of which 7 modes are allowed, with only the ν_{10} mode being forbidden (Shimanouchi, 1972), as such the spectrum of propane is extremely congested in this region.

Table 9. The 27 fundamental modes of propane, data from Shimanouchi, (*Shimanouchi 1972*). Modes with wavenumbers marked with an asterisk are infrared inactive.

| Symmetry | Mode | Mode type | Wavenumber (cm ⁻¹) |
|----------------|-----------------|-------------------------|--------------------------------|
| a ₁ | v ₁ | CH ₃ stretch | 2977 |
| | v ₂ | CH ₃ stretch | 2962 |
| | v ₃ | CH ₂ stretch | 2887 |
| | v ₄ | CH ₃ deform | 1476 |
| | v ₅ | CH ₂ scis | 1462 |
| | v ₆ | CH ₃ deform | 1392 |
| | v ₇ | CH ₃ rock | 1158 |
| | v ₈ | CC stretch | 869 |
| | v ₉ | CCC deform | 369 |
| a ₂ | v ₁₀ | CH ₃ stretch | 2967* |
| | v ₁₁ | CH ₃ deform | 1451* |
| | v ₁₂ | CH ₂ twist | 1278* |
| | v ₁₃ | CH ₃ rock | 940* |
| | v ₁₄ | Torsion | 216* |
| b ₁ | v ₁₅ | CH ₃ stretch | 2968 |
| | v ₁₆ | CH ₃ stretch | 2887 |
| | v ₁₇ | CH ₃ deform | 1464 |
| | v ₁₈ | CH ₃ deform | 1378 |
| | v ₁₉ | CH ₂ wag | 1338 |
| | v ₂₀ | CC stretch | 1054 |
| | v ₂₁ | CH ₃ rock | 922 |
| b ₂ | v ₂₂ | CH ₃ stretch | 2973 |
| | v ₂₃ | CH ₂ stretch | 2968 |
| | v ₂₄ | CH ₃ deform | 1472 |
| | v ₂₅ | CH ₂ rock | 1192 |
| | v ₂₆ | CH ₂ rock | 748 |
| | v ₂₇ | Torsion | 268 |

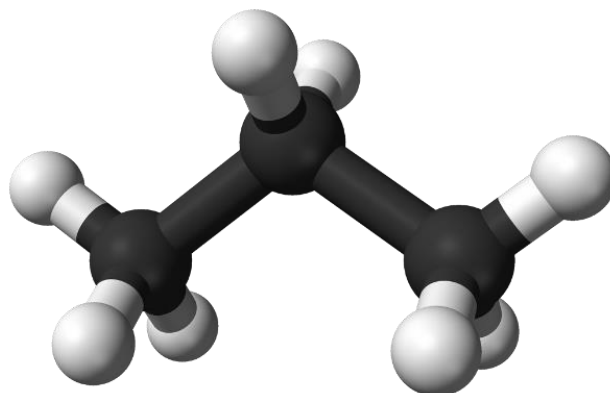


Figure 33. Stick and ball figure of propane. The mode types in Table 9 refer to the central methylene group (CH_2), the two methyl groups (CH_3) either side of the methylene group or vibrational modes between the carbon atoms. Adapted from:

<https://commons.wikimedia.org/wiki/File:Propane-3D-balls-B.png>, accessed June 15th, 2017.

Infrared absorption cross-sections are typically presented instead of a list of individual lines. Several molecular databases include data for propane. HITRAN (*Rothman et al.*, 2013) contains cross-sections for propane, broadened by air, from *Harrison and Bernath* (2010) for 195-296.4 K at high resolution (0.015 cm^{-1}) in the range $2540\text{-}3300 \text{ cm}^{-1}$ (*Harrison and Bernath*, 2010). GEISA (*Jacquinet-Husson et al.*, 2016) includes cross-sections for $220\text{-}2000 \text{ cm}^{-1}$, broadened by N_2 , recorded at 296 K at a resolution of 0.25 cm^{-1} , as well as 8983 transitions in the range $700\text{-}800 \text{ cm}^{-1}$, the CH_2 rocking mode region at a resolution of 0.08 cm^{-1} . Absorption cross-sections of propane broadened by N_2 are available from the Pacific Northwest National Laboratory (PNNL), recorded in the infrared at 278, 293 and 323 K, in the range $600\text{-}6500 \text{ cm}^{-1}$ at medium resolution (0.1 cm^{-1}) (*Sharpe et al.*, 2004). Cross-sections provided by *Sung et al.* (2013) were also recorded, broadened by N_2 , at various temperatures between 145-297 K, in the range $690\text{-}1550 \text{ cm}^{-1}$ at resolutions of $0.0033\text{-}0.0056 \text{ cm}^{-1}$. Absorption cross-sections for propane broadened by N_2 have

been measured in the 3 μm region ($2500\text{--}3400\text{ cm}^{-1}$) at elevated temperatures (*Grosch et al.*, 2010), although at medium resolution (0.09 cm^{-1}) and relatively low temperatures (298, 373 and 473 K).

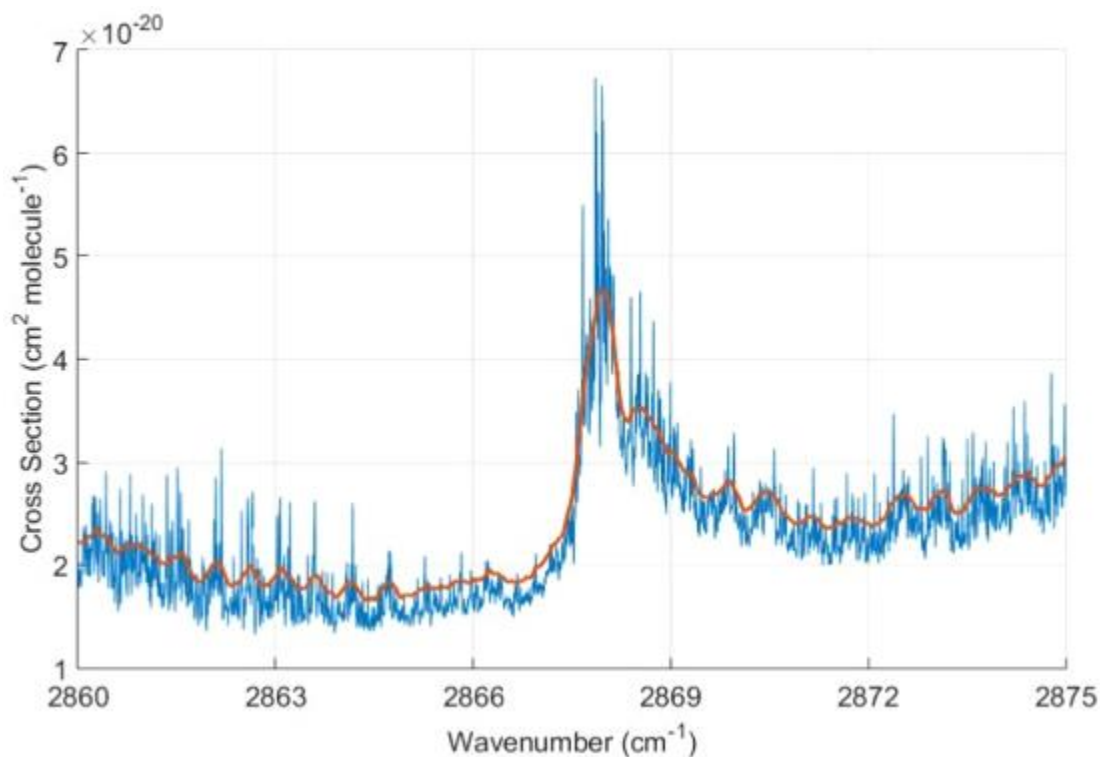


Figure 34. Comparison of propane spectra (C_3H_8) at high resolution (0.005 cm^{-1} , blue trace) and medium resolution (0.08 cm^{-1}), orange trace. Figure from *Buzan et al.* (2016).

The efficiency of a number of fuels and engines is important for industrial applications. The combustion reactions involved can be analyzed by sophisticated models which include a large number of temperature dependent reactions from the constituents of fuels and the products of their combustion. To this end, spectra have been recorded to monitor a number hydrocarbons in combustion reactions (*Klingbeil et al.*, 2007; *Chrystie et al.*, 2015; *Eiji et al.*, 2003; *Sahlberg et al.*, 2016; *Grosch et al.*, 2011).

Cross-sections from high resolution spectra (0.1 cm^{-1} or better) of a number of hydrocarbons have been studied in the $3 \text{ }\mu\text{m}$ region at elevated temperatures, including ethane (*Hargreaves et al.*, 2015), propylene (C_3H_6) (*Klingbeil et al.*, 2007; *Es-sebbar et al.*, 2014), methane, ethane and ethylene (C_2H_4) (*Es-sebbar et al.*, 2014). *Klingbeil et al.*, (2007) have also obtained spectra of a number of larger hydrocarbons (12 in total) at 1 cm^{-1} resolution up to 500°C . However there do not exist high resolution cross-section measurements of propane for the $3 \text{ }\mu\text{m}$ region. Such data are required to accurately model hot environments such as auroral regions on Jupiter, exoplanets or brown dwarfs. Figure 34 shows the lack of structure in the spectrum of propene at low resolution and the inclusion of line structure in high resolution data. The results in this Chapter address the lack of high resolution cross-sections of propane at high temperature.

EXPERIMENTAL

High resolution (0.005 cm^{-1}) propane spectra were recorded between 2500 and 3500 cm^{-1} , at five temperatures from 296 K to 700 K using a Bruker IFS 125HR Fourier transform spectrometer. This region contains the seven active C-H stretching modes (*Shimanouchi*, 1972) and a number of combinations and overtones of the various other modes. The propane gas is contained in a quartz cell which is heated to the appropriate temperature using a tube furnace as described in Chapter III.

To obtain a transmission spectrum (τ) two individual spectra are recorded for each temperature and combined as:

$$\tau = \frac{A_{ab}}{A_{ref}}, \quad (21)$$

where the C_3H_8 absorption component is given by A_{ab} and A_{ref} is the background spectrum.

Table 10. Experimental conditions and setup of the Bruker IFS 125 HR

| | |
|------------------------------|------------------|
| Spectral range (cm^{-1}) | 2500-3500 |
| Temperature range (K) | 296-700 |
| Resolution (cm^{-1}) | 0.005 |
| Cell path length (cm) | 50 |
| Detector | InSb |
| Filter | Germanium |
| Windows | CaF ₂ |
| Beamsplitter | CaF ₂ |
| Number of scans | 300 |

The conditions for the experiment are detailed in Table 10. At higher temperatures (600 and 700 K) there is an emission component which is significant enough that it must be corrected for. As a result two additional spectra were recorded for these temperatures without the infrared source, one with propane in the sample cell and one without. These emission spectra were subtracted from A_{ab} and A_{ref} respectively. The experimental setup and procedure for obtaining the transmission spectrum are described in *Hargreaves et al. (2015a)* where it was used to produce temperature dependent line lists for CH_4 and to obtain temperature dependent cross-sections for C_2H_6 (*Hargreaves et al., 2015b*).

The C-H stretching region contains a number of water lines that were removed using the OPUS software once the transmission spectra were obtained.

RESULTS

The experimental transmission spectra are converted to absorption cross-sections, σ (cm^2 molecule $^{-1}$) using the equation:

$$\sigma = -\xi \frac{10^4 k_B T}{Pl} \ln \tau(\nu), \quad (22)$$

where k_B is the Boltzmann constant ($1.38065 \times 10^{-23} \text{ J K}^{-1}$), T is temperature (K), P is the propane pressure (Pa), l is the optical path length (m), $\tau(\nu)$ is the transmittance at each wavenumber and ξ is a factor which is used to normalize the experimental cross sections to PNNL (*Harrison and Bernath, 2010*).

Table 11. Propane integrated cross-section calibration.

| Temperature (K) | Sample Pressure (Pa) | Normalization Factor | Effective Pressure (Pa) | Integrated Cross-Section ($\times 10^{-17} \text{ cm molecule}^{-1}$) |
|--------------------|-------------------------|-------------------------|----------------------------|--|
| 296 | 173.85 | 1.395 | 124.64 | 4.257 |
| 400 | 216.92 | 1.227 | 176.86 | 4.257 |
| 500 | 264.11 | 1.325 | 199.32 | 4.258 |
| 600 | 375.97 | 1.105 | 340.21 | 4.258 |
| 700 | 428.63 | 1.049 | 408.59 | 4.257 |

PNNL cross-sections are given in units of $\text{ppm}^{-1} \text{ m}^{-1}$ at 296 K, which may be converted into units of cm molecule^{-1} using the conversion $k_B \times 296 \times \ln(10) \times 10^4 / 0.101325$. The PNNL integrated cross-sections in the region $2550\text{-}3500 \text{ cm}^{-1}$ for 278, 293 and 323 K are 4.248×10^{-17} , 4.214×10^{-17}

and 4.310×10^{-17} cm molecule⁻¹, respectively. The mean of the three PNNL integrated cross-sections is 4.257×10^{-17} and are within 2.3% of each other (Sharpe *et al.* 2004).

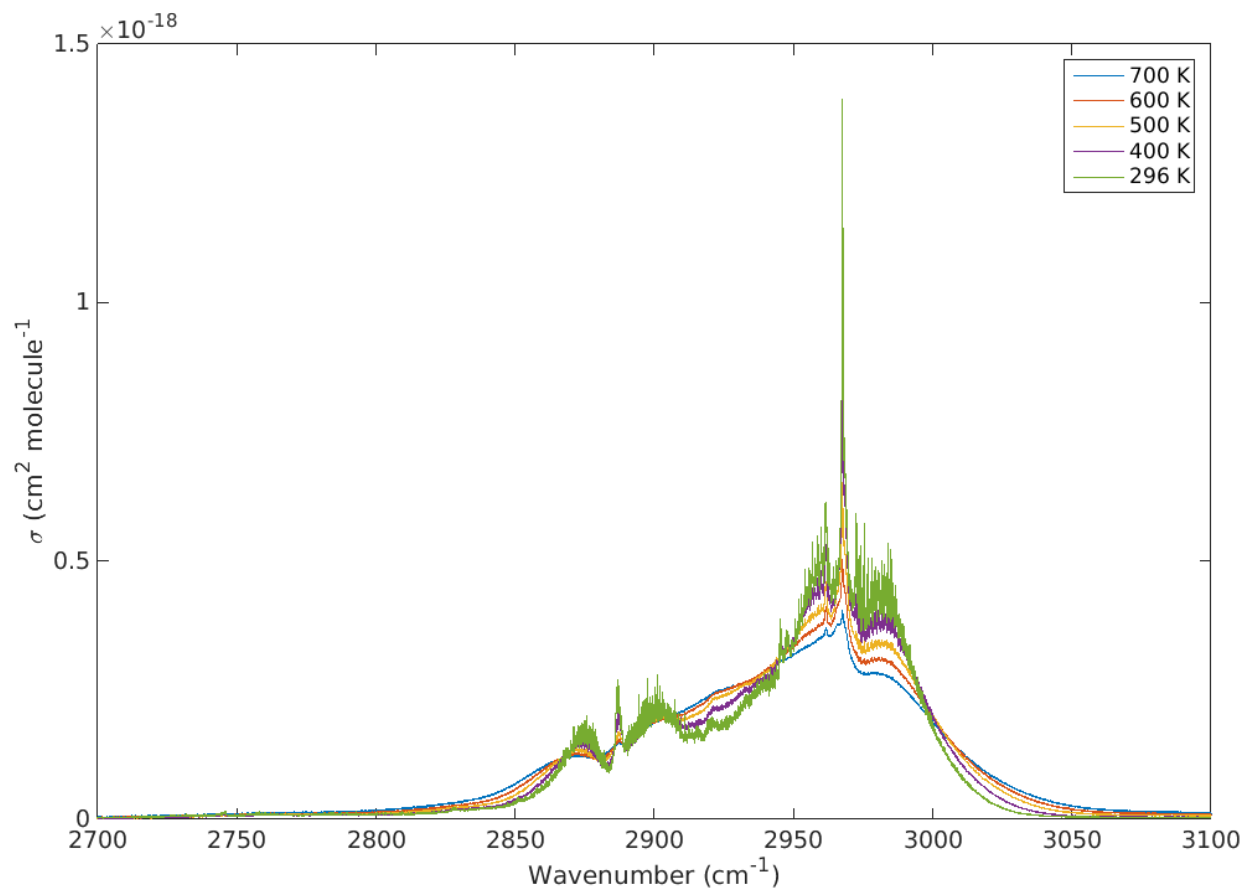


Figure 35. Cross-sections (0.005 cm^{-1} resolution) for increasing temperatures in the range 2700-3100 cm^{-1} (Beale *et al.*, 2016b).

In the experimental setup, the temperature and path length can be more reliably determined than pressure, P . The normalization factor ζ is applied to the recorded pressure and typical corrections are of the order of 5% (Hargreaves *et al.*, 2015), however a small leak of air in the regulator resulted in an overestimation of the cell pressure by approximately 40 Pa. This additional pressure was sufficiently small that no adverse increase in the recorded line widths was observed. However

sample pressures were overestimated by approximately 40 Pa leading to an increased normalization factor (Table 11). This pressure error is accounted for when calibrating to the integrated cross-sections of PNNL.

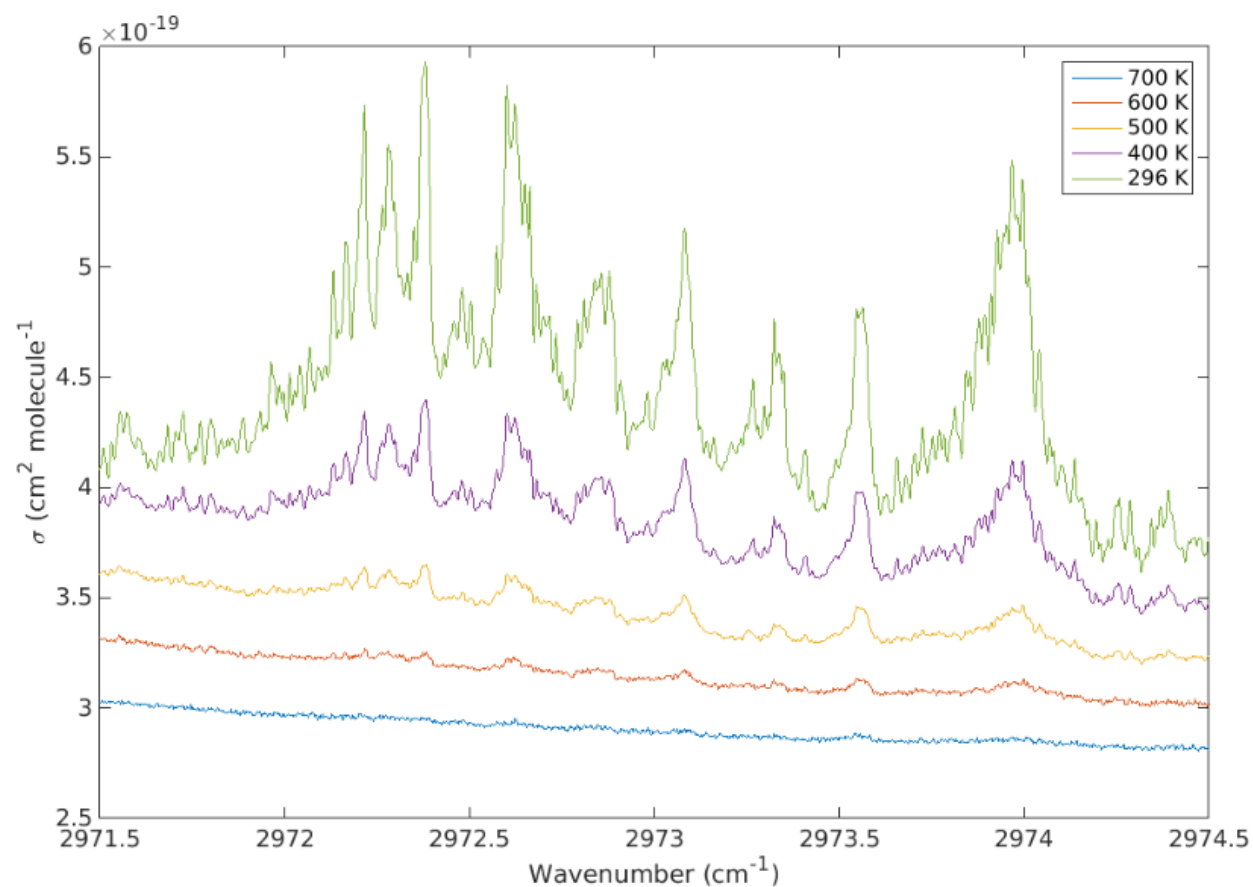


Figure 36. A more detailed view of each spectrum (2971.5-2974.5 cm⁻¹) where the strong features are seen to weaken with increasing temperature (*Beale et al.*, 2016b).

The normalization factors are used to establish the effective propane pressures of the sample and are given in Table 11. The resulting calibrated integrated cross-sections for each temperature over

the range 2550-3500 cm^{-1} are also provided in Table 11 and shown in Figure 35. The peak cross-sections for the modes at 2887 cm^{-1} (Figure 10), 2962 cm^{-1} and 2967 cm^{-1} are stronger at lower temperatures than at high temperatures.

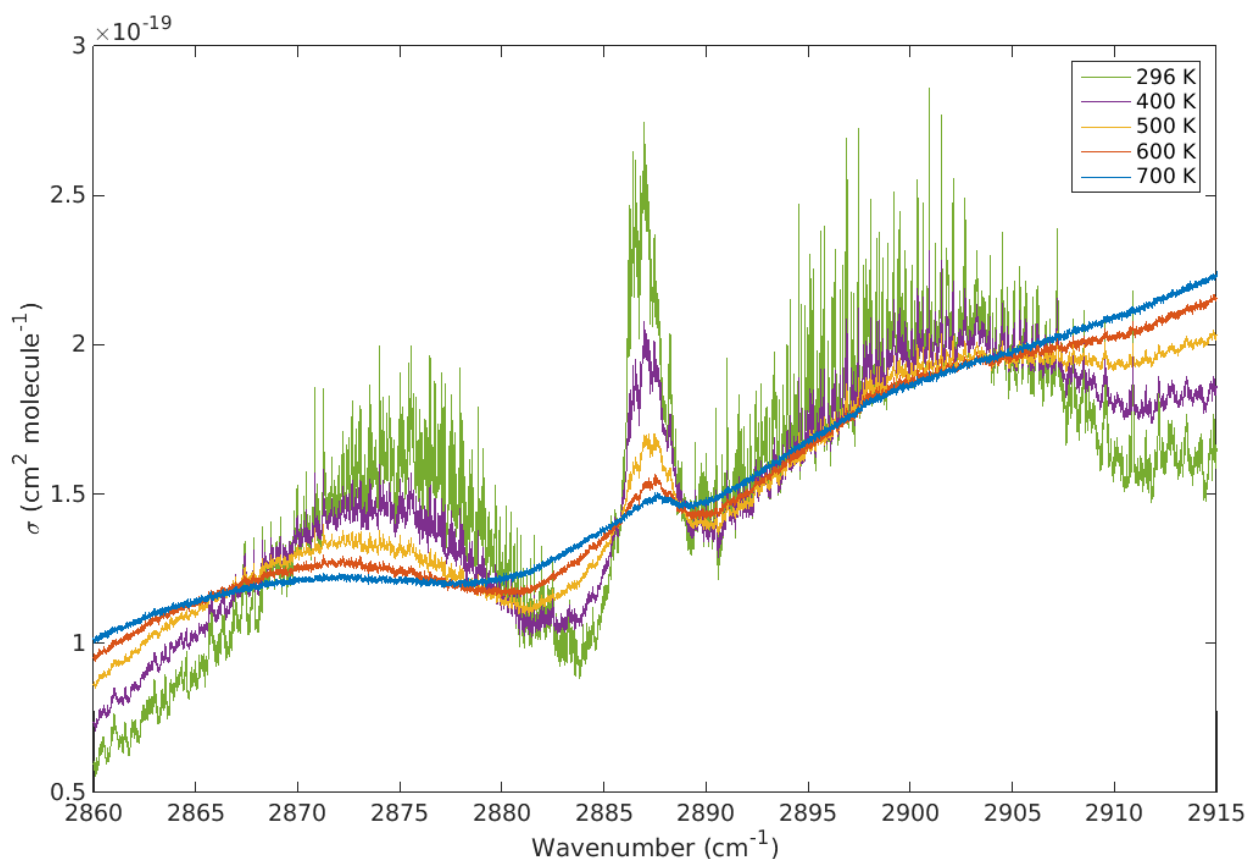


Figure 37. A more detailed view of the ν_3 and ν_{16} modes centered at 2887 cm^{-1} . Sharp features that are identifiable in room temperature spectra blend into the continuum as the temperature increases (*Beale et al.*, 2016b).

The spectrum at each temperature was recorded at high resolution (0.005 cm^{-1}) and the evolution of the sharp, individual features of the low temperature spectra can be seen to gradually decrease

to form a continuum with increasing temperature (Figure 36). This is primarily caused by Doppler broadening of spectral lines and increasing populations of higher rotational states and hot bands. Figure 37 demonstrates the temperature-dependence of the propane continuum between 2860 and 2910 cm^{-1} . The prominent P, Q and R branch structure (due to the ν_3 and ν_{16} bands) is effectively reduced to a gradual slope with no defining features over the observed temperature range.

DISCUSSION

The discrepancy between the recorded pressure and the effective pressure, used to calculate the calibrated integrated cross-sections, was up to 40% (at room temperature, see Table 11) and is much larger than with previous measurements. This pressure error was relatively consistent in absolute terms (around 40 Pa) and came from the propane gas tank regulator. The cell path length of 50 cm is determined to within 0.5% and the elevated temperatures (those above room temperature) are accurate to within 2%. The pressures were recorded along the same gas line as the cell using a 10 Torr MKS Baratron, which is accurate to within 0.5%. In addition to the experimental errors, photometric errors, estimated to be within 2%, were observed by variations between recorded baselines. These may be due to a number of reasons such as deposition of impurities on the cell windows, variation in the intensity of the light source during the recording of the spectra and changing environmental conditions over the course of measurement, such as room temperature and humidity. The PNNL propane spectra are composites of approximately 10 pathlength concentrations, making them suitably accurate to be used for calibration. These combined errors of our recorded spectra are therefore accounted for by calibration against the averaged integrated cross-sections of the three PNNL spectra. Our estimated error in the calibrated

absorption cross-sections is therefore approximately 5 %, which is consistent with the estimated errors from PNNL.

The integrated cross-section over an isolated band has been shown to be independent of temperature (*Hargreaves et al.*, 2015; *Breeze et al.*, 1965; *Crawford*, 1958). For comparison between temperatures, the cross-sections should be integrated over isolated bands, i.e. the transmission at the integration limits must be 100%. For propane, the large number of absorption bands within the observed 3 μm region (particularly at high temperature) means that complete isolation is not guaranteed. The 2550 and 3500 cm^{-1} integration limits were chosen as they provide the transmission maxima within the observed region.

The development of pseudo-continua with increasing temperature has been observed in CH_4 (*Hargreaves et al.*, 2015) for which the large number of weak lines contribute significant absorption at higher temperatures. For larger hydrocarbons such as C_2H_6 , the low frequency torsional modes result in a larger continuum effect (*Hargreaves et al.*, 2015). The changing shape of the spectral features of C_3H_8 with increasing temperature in this region can be seen in Figure 35. The populations of the low frequency torsional modes at 216 cm^{-1} (ν_{14} , a_2) and 268 cm^{-1} (ν_{27} , b_2) increase with temperature resulting in the growth of a broad continuum.

These measurements are the first high resolution absorption cross-sections of propane at high temperature and will find use in the remote sensing of propane on exoplanets, brown dwarfs and for combustion monitoring. The temperature-dependence of the propane cross-section in this region makes it suitable for inferring the temperature, particularly the sharp Q branches at 2887 cm^{-1} and 2967 cm^{-1} . It is only at high resolution that many of the temperature dependent features can be identified. Certain sub-regions are also unsuitable for temperature determination of propane. For example, the crossover point at 2945 cm^{-1} between the stronger continuum of the

higher temperatures and the sharp features of the low temperature Q branches here shows no temperature dependence.

CONCLUSION

High resolution absorption cross-sections have been measured for pure propane in the region 2550-3500 cm^{-1} at 296, 400, 500, 600 and 700 K. The integrated cross-sections were calibrated against PNNL values for the same spectral region. The data (available as wavenumber dependent cross-sections in the supplementary material of the paper published from this work (*Beale et al.*, 2016b)) may be included in simulations of astronomical atmospheres at appropriate temperatures, such as those of exoplanets and brown dwarfs.

CHAPTER VI

INFRARED SPECTRA OF AMMONIA

The results in Chapter VI span two separate sets of data. The first set encompasses the 2400-5500 cm^{-1} spectral range. The analysis for this dataset has been published in the Journal of Quantitative Spectroscopy and Radiative Transfer (*Beale et al.*, 2017). Co-authors for this article are Robert Hargreaves (Old Dominion University, now Oxford University), Phillip Coles (University College London), Jonathan Tennyson (University College London) and Peter Bernath (Old Dominion University). Robert Hargreaves assisted in data collection as hot ammonia requires special safety considerations, necessitating more than one person in the laboratory at the time of recording. Phillip Coles produced the 'BARVEL' dataset which was used to compare to the experimental data for quantum number assignment. Jonathan Tennyson is the group leader of Coles at University College London and Peter Bernath was the overall PI for the project. For the 4800-9000 cm^{-1} region, Andy Wong (Old Dominion University) assisted with data collection. All text and figures (unless explicitly cited) in this chapter are my original work. All analysis of the experimental data is my own work, including calculation of experimental lower state energies, production of linelists and comparison of the data to BARVEL and HITRAN to obtain quantum numbers.

INTRODUCTION

Ammonia (NH_3) is a widely-studied molecule in atmospheric chemistry. In the Earth's atmosphere, where sources include animal waste and fertilizers (*Beer et al.*, 2008), it acts as a precursor in the production of aerosols (*Höpfner et al.*, 2016) and particulate matter (*Clarisse et al.*, 2009). Deposition of atmospheric NH_3 can lead to fertilization, a side effect of which may be decreased biodiversity (*von Bobrutski et al.*, 2010).

NH_3 has also been observed in a number of astrophysical environments. In the solar system, it has been detected in the atmospheres of Jupiter (*Wildt*, 1931; *Carlson et al.*, 1996), Saturn (*Fletcher et al.*, 2012) and Titan (*Nelson et al.*, 2009) as well as on comets (*Bird et al.*, 1997; *Biver et al.*, 2012). The pure rotational transitions and inversion transitions of NH_3 have been detected in molecular clouds (*Cheung et al.*, 1968; *Ho and Townes*, 1983) making it one of the first extraterrestrial polyatomic molecules discovered. The atmospheres of cool astronomical objects, such as brown dwarfs and exoplanets, have low enough temperatures to allow small molecules such as NH_3 to form and maintain large enough concentrations to be detected.

AMMONIA IN BROWN DWARFS

Sub-stellar objects with sufficiently low mass (<0.08 solar masses) are known as brown dwarfs and cannot fuse hydrogen within their cores (*Burrows et al.*, 2001). The first such object discovered was Gliese 229B (*Oppenheimer et al.*, 1995) and since then a large number of brown dwarfs have been detected with atmospheres cool enough (500 – 2400 K) for a number of molecular species to exist. Indeed, brown dwarfs, similar to stars, are classified by the presence or absence of particular atomic and molecular features. The hottest such objects, the L dwarfs, contain features from

electronic transitions of metal hydrides such as FeH (*Hargreaves et al.*, 2010) and CrH (*Burrows et al.*, 2002; *Kirkpatrick et al.*, 1999). T dwarfs are distinguished by hot H₂O and CH₄ transitions (*Burgasser et al.*, 2006; *Cushing et al.*, 2006). NH₃ is observed in late T dwarfs, with increasing concentrations as the objects cool (*Cushing et al.*, 2006; *Line et al.*, 2015) as shown in figures 38 and 39. As such, NH₃ is expected to characterize a yet cooler class, the Y dwarfs that have an approximate maximum temperature of ~700 K. Y-dwarfs have now been observed and NH₃ appears as a shoulder on a feature at 1.58 μm (*Leggett et al.*, 2016; *Cushing et al.*, 2011).

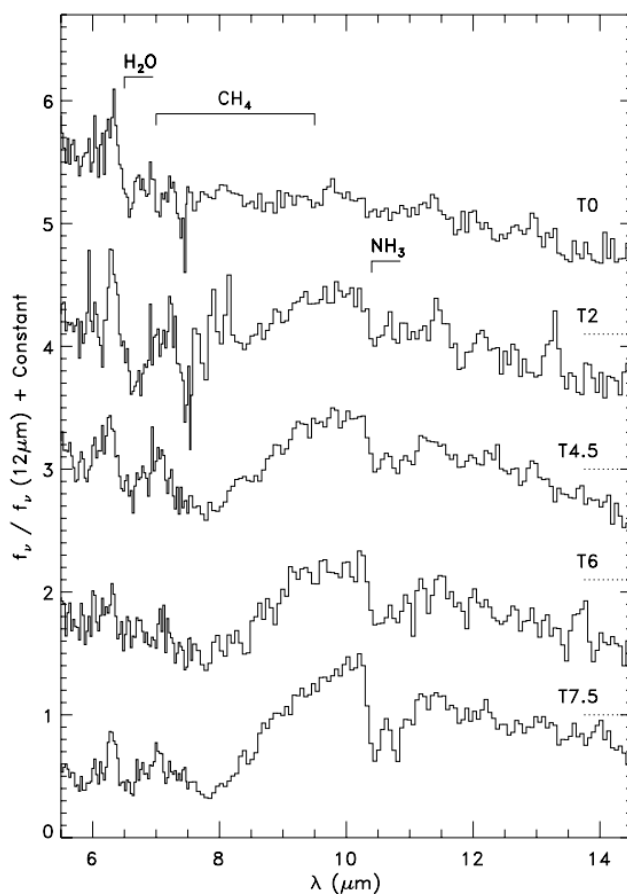


Figure 38. Spectra of 5 different T dwarf stars. As the temperature of the stars decrease from approximately 1300 K for a T0 to 900 K for a T7.5, the strength of the P and R branches of the NH₃ bending mode at 10.5 μm increase. Figure from *Cushing et al.*, (2006).

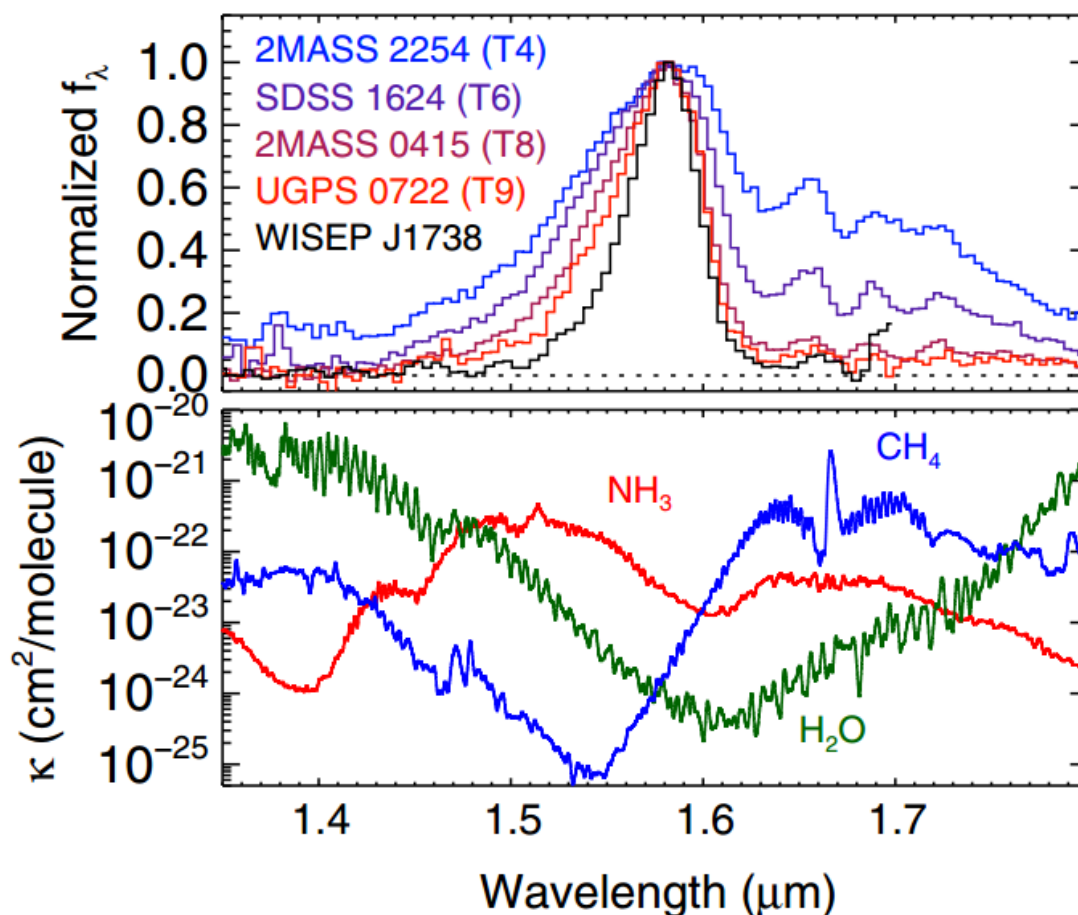


Figure 39. Bottom: opacity calculations for NH_3 , CH_4 and H_2O at 600 K. Top: H-band spectra of several T-type dwarfs. Note the increasing absorption in the shoulder of the feature at 1.58 μm as the temperature of the objects decreases. Figure from *Cushing et al.* (2011).

AMMONIA IN EXOPLANETS

Since the discovery of the first exoplanet in 1995 (*Mayor and Queloz, 1995*) more than 3500 have been discovered (<http://exoplanet.eu/>). If the planet passes in front of the star it orbits, then it may be detected by observation of periodic decreases in light intensity of the parent star. This technique

is known as the transit method and was first used successfully to detect the planet HD 209458b (Charbonneau *et al.*, 2000) and has since been used by the Kepler mission to observe large numbers of exoplanet candidates (Batalha *et al.*, 2013).

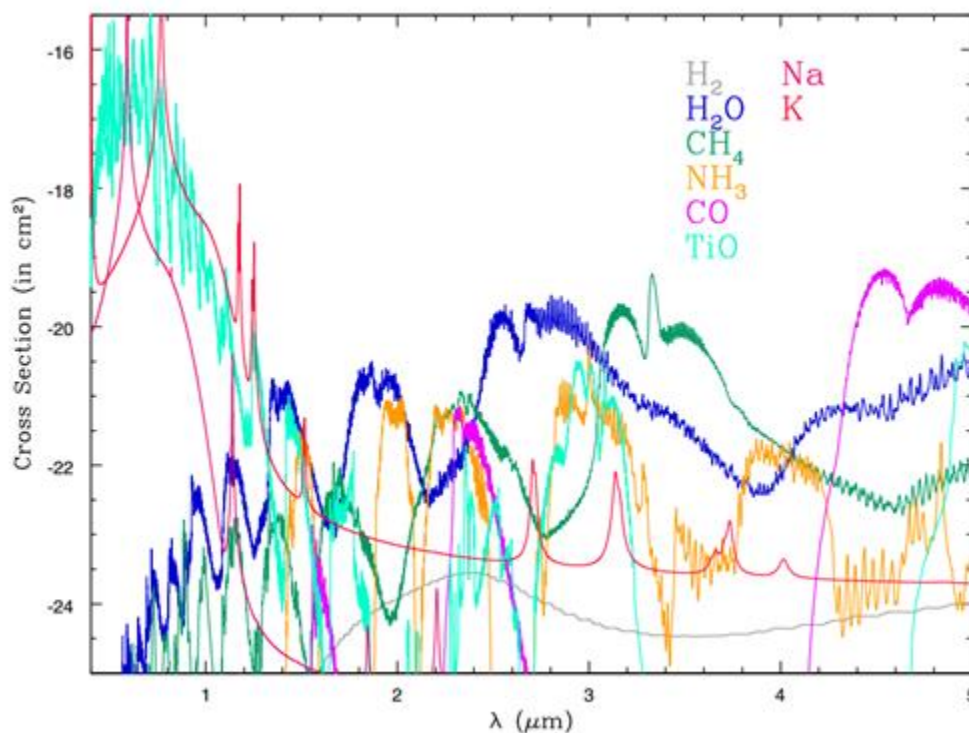


Figure 40. Calculation of cross-sections of a number of molecules predicted to exist in exoplanetary atmospheres, including NH_3 (orange). Between 1.4 and 5.0 μm (the region of interest in this experimental study) there are a number of strong absorption bands. Figure from Burrows (2014).

This technique also allows the spectrum of the exoplanet atmosphere to be obtained by recording the transit dips as a function of wavelength (Bernath, 2014) and use of the method has resulted in the detection of a number of molecules such as H_2O (Barman, 2008; Grillmair *et al.*, 2008), CH_4 (Swain *et al.*, 2008), CO (Swain *et al.*, 2009) and CO_2 (Swain *et al.*, 2009). As yet, NH_3 has not been observed in the atmosphere of an exoplanet, however a number of modelling studies have

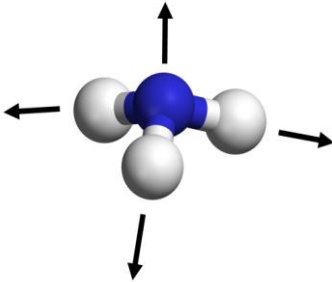
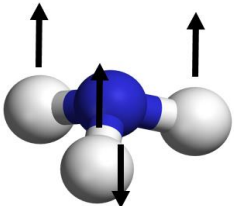
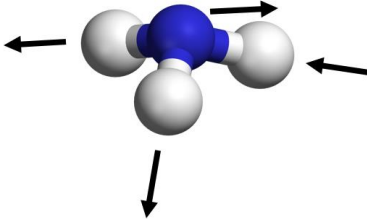
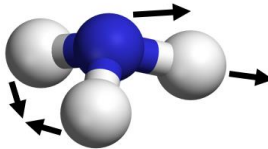
predicted its presence in hydrogen-rich hot-Jupiters (*Line et al.*, 2011; *Burrows*, 2014; *Venot et al.*, 2012) Figure 40 demonstrates the importance of the 2-5 μm region in the detections of NH_3 in exoplanetary atmospheres.

SPECTROSCOPY OF AMMONIA

NH_3 is a polyatomic molecule having four atoms arranged in a trigonal pyramid structure with C_{3v} symmetry (*Bernath*, 2005). Ammonia has a complex infrared spectrum with 6 fundamental vibrational modes, two of which are doubly degenerate. The four fundamental vibrational frequencies are: the symmetric stretch at 3336.2 cm^{-1} (ν_1 , a_1), the symmetric bend at 932.5 cm^{-1} (ν_2 , a_1), the antisymmetric stretch at 3443.6 cm^{-1} (ν_3 , e) and the antisymmetric bend at 1626.1 cm^{-1} (ν_4 , e), Table 5.1 provides details of these modes.

There has been extensive work on the spectroscopy of ammonia in the infrared. For example, experimental line lists have been obtained in the 2 μm (*Brown and Margolis*, 1996) and 3 μm (*Kleiner et al.*, 1999) regions. The most complete line assignments for NH_3 in the infrared are compiled in the HITRAN 2012 database (*Rothman et al.*, 2013). However HITRAN is intended for applications near room temperature and lacks complete hot band coverage in this region (*Down et al.*, 2013). The hot bands are essential when comparisons are made to high temperature atmospheres. A comprehensive theoretical line list, BYTe, has been calculated for NH_3 that can be used at temperatures up to 1500 K and contains approximately 1.1 billion transitions (*Yurchenko et al.*, 2011).

Table 12. Summary of the fundamental modes of ammonia. For each mode there are two frequencies, due to inversion doubling (Figure 3.4). Figures adapted from (Mills, 2008a).

| Mode | Symmetry | Wavenumber (cm^{-1}) | Description | |
|---------|----------|------------------------------------|-----------------------|---|
| ν_1 | a_1 | 3336.2 3337.2 | Symmetric stretch |  |
| ν_2 | a_1 | 932.5 968.3 | Symmetric bend |  |
| ν_3 | e | 3443.6 3443.9 | Asymmetric stretch |  |
| ν_4 | e | 1626.1 1627.4 | Asymmetric bend |  |

The rotational-vibrational calculations from *Huang et al.*, (2011a, 2011b) and references therein, provide an additional line list for ammonia in this region.

High temperature experimental line lists have been obtained using emission spectroscopy at high resolution (0.01 cm^{-1}) from $740\text{-}2100\text{ cm}^{-1}$ (*Hargreaves et al.*, 2011) and $1650\text{-}4000\text{ cm}^{-1}$ (*Hargreaves et al.*, 2012). Absorption spectra at moderate resolution (0.09 cm^{-1}) of hot samples at atmospheric pressure have also been recorded in the $500\text{-}2100\text{ cm}^{-1}$ (*Barton et al.*, 2015) and $2100\text{-}5500\text{ cm}^{-1}$ (*Barton et al.*, 2016) spectral regions. Existing experimental line lists have been used in an energy level analysis (MARVEL) to predict a large number of unmeasured lines (*Al Derzi et al.* 2015). Our work reported below details an extension of these experimental line lists, in the $2400\text{-}5500\text{ cm}^{-1}$ region using an improved cell design and technique (*Hargreaves et al.*, 2015) to record transmission spectra of hot samples. This chapter details the determination of empirical lower state energies, intensities and line positions ($\pm 0.002\text{ cm}^{-1}$) which can be used in atmospheric models for brown dwarfs and exoplanets.

One interesting fact concerning the spectroscopy of ammonia is that each of the frequencies of the four fundamental modes (Table 12) is doubled. Ammonia has a low barrier to inversion and can therefore convert between its left and right handed forms via quantum mechanical tunneling (Figure 41). The interaction between the left and right handed forms causes the wavefunctions of each form to mix giving rise to splitting of energy levels and therefore the transition frequencies.

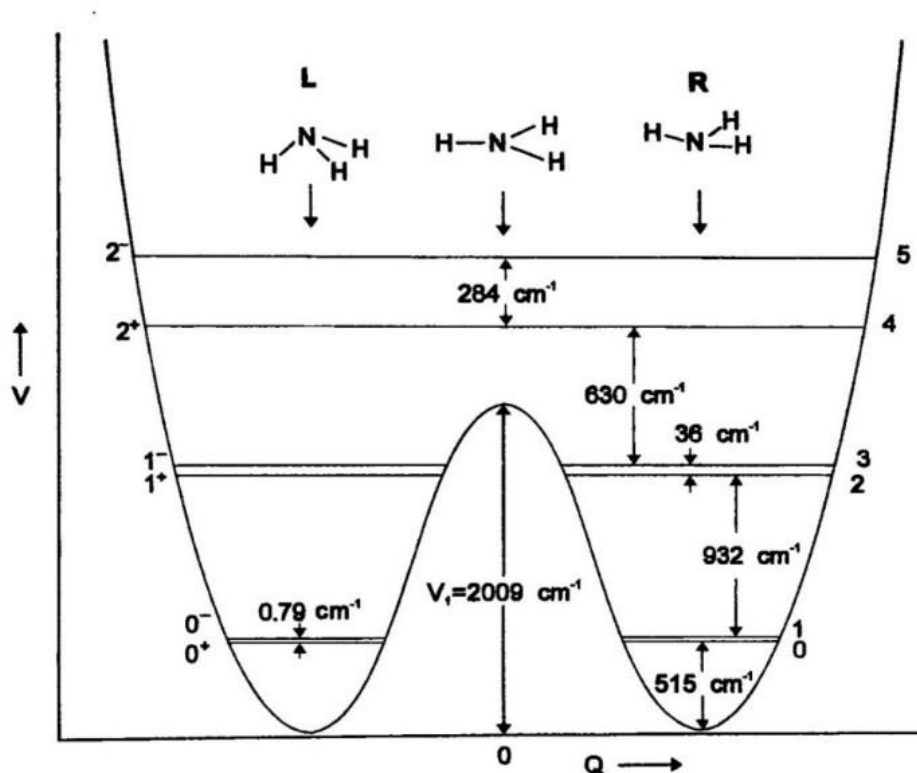


Figure 41. Energy level diagram of ammonia demonstrating the inversion doubling of the energy levels of ammonia. The x-axis represents the angle of the nitrogen-hydrogen bonds from a planar configuration and the y-axis gives the energy (Bernath, 2005).

EXPERIMENTAL

Transmission spectra were recorded for two separate regions in the infrared. The first region recorded spectra at seven different temperatures: 296 K, 473 K, 573 K, 673 K, 773 K, 873 K and 973 K in the region $2400\text{-}5500 \text{ cm}^{-1}$ and will be referred to as the low wavenumber range. The second region was recorded at 293 K, 400 K, 500 K, 600 K, 700 K, 800 K and 900 K in the region $5400\text{-}9000 \text{ cm}^{-1}$ and will therefore be referred to as the high wavenumber range. Both sets of spectra were recorded using a sealed quartz cell, tube furnace and Fourier transform spectrometer

as detailed in Chapter III. These ranges include the effective temperatures of the mid and late T dwarfs (*Cushing et al.*, 2006) and Y dwarfs (*Cushing et al.*, 2011) as well as the coolest observed hot Jupiters (*Line et al.*, 2011). Above 973 K thermal decomposition of the sample gas reduces the signal to such an extent that reliable spectra could not be obtained. The decomposition of the sample at high temperature is gradual and was noticed even at 873 K and 973 K in the first set of measurements. For this reason, the second set of measurements was recorded with a maximum temperature of 900 K. Also, given that the second region contains no fundamental modes and only combinations or overtones (see Chapter III), the signals of which are inherently weaker than fundamental modes, the lower temperature was used. The first set of measurements, recorded in October 2014, have been published as *Beale et al.* (2017). The second set of measurements, recorded in February 2016, have been analyzed and will be submitted as a research paper.

The transmission spectrum for each temperature is obtained from four individual spectra that, when combined, correct for NH₃ and cell emission; this method has been used previously to record spectra for methane (*Hargreaves et al.*, 2015). An absorption spectrum (A_{ab}) is recorded with NH₃ in the cell at temperature with an external emission source (200 W tungsten halogen broadband lamp). A background reference spectrum for the absorption (A_{ref}) is recorded without the NH₃ in the cell. The emission spectrum (B_{em}) is recorded with NH₃ in the cell at temperature without the lamp. The background reference spectrum for emission (B_{ref}) is recorded without the sample in the cell and with the lamp turned off. These spectra are combined to calculate the transmission spectrum for each temperature as:

$$\tau = \frac{A_{ab} - B_{em}}{A_{ref} - B_{ref}}. \quad (23)$$

The experimental technique is essentially the same for both the low and high wavenumber ranges. However certain considerations, such as the optical setup (windows and filters) and the temperature units, differ between the two. They will therefore be considered separately in this chapter. The conditions and results for the low wavenumber region will be given first and the conditions and results for the second region will be given after. Some discussion will be shared between the two regions as it is relevant to the experimental procedure, or ammonia as a whole. This will be presented at the end of the chapter.

TRANSMISSION SPECTRA OF NH₃ IN THE 2400-5500 CM⁻¹ REGION

Spectra were recorded in the 2400 – 5500 cm⁻¹ region, providing overlap with previous experimental work (*Hargreaves et al.*, 2012). This previous work includes spectral regions that cover the $3\nu_2/\nu_2+\nu_4$ (where $3\nu_2$ represents three quanta of the ν_2 mode and $\nu_2+\nu_4$ represents one quantum of the ν_2 mode and one quantum of the ν_4 mode) and $\nu_1/\nu_3/2\nu_4$ bands and the work provided here extends this coverage to include spectral regions that contain the $\nu_1+\nu_2/\nu_2+\nu_3$ and $\nu_1+\nu_4/\nu_3+\nu_4$ bands as well as associated hot bands. Notably, this region contains the bands associated with the ν_1 and ν_3 fundamental modes.

The 50 cm quartz tube sample cell was used under static conditions, i.e. the gas sample was enclosed in the cell for the entire experimental run to contain the NH₃ sample. The cell is contained within the tube furnace (Figure 17) which is heated to the appropriate temperature, which is accurate to within ± 10 °C. The cell was aligned with the entrance aperture of a Bruker IFS 125 HR Fourier transform spectrometer, and radiation was focused into the spectrometer using a CaF₂

lens. The spectrometer used a CaF₂ beamsplitter, covering the spectral region 1650–7000 cm⁻¹, and an indium antimonide (InSb) detector. Experimental parameters are summarized in Table 13.

Table 13. Experimental conditions for NH₃ low wavenumber region.

| Parameter | Value |
|-------------------------------------|------------------|
| Spectral region (cm ⁻¹) | 2400-5500 |
| Detector | InSb |
| Beamsplitter | CaF ₂ |
| Spectrometer Windows | CaF ₂ |
| Lens | CaF ₂ |
| Filter | Ge |
| Scans | 300 |
| Resolution (cm ⁻¹) | 0.01 |
| NH ₃ Pressure (Torr) | 40 |
| Zerofilling factor | x 16 |

Table 14. Total number lines, the number of added lines, partition functions and tentative assignments made via comparison with each line list at each temperature (*Yurchenko et al.*, 2011).

| Temperature | Number | HITRAN | Down <i>et al.</i> | MARVEL |
|--------------------|-----------------|------------------|---------------------------|--------------------|
| (K) | of lines | additions | assignments | assignments |
| 296 | 8494 | 722 | 2136 | 1813 |
| 473 | 16019 | 789 | 3020 | 2721 |
| 573 | 20300 | 825 | 2976 | 2839 |
| 673 | 23010 | 834 | 2913 | 2906 |
| 773 | 20066 | 713 | 2569 | 2594 |
| 873 | 18794 | 691 | 2296 | 2346 |
| 973 | 9985 | 598 | 1660 | 1178 |

The resulting transmittance spectra contained a number of H₂O lines which were removed manually using the Bruker OPUS software. After combining the spectra at each temperature to calculate a transmission spectrum, peaks were picked using WSpectra (*Carleer, 2001*) to measure their position and intensity, the lines are then fitted by WSpectra using a Voigt lineshape profile. Lines were calibrated for line position and intensity by matching strong and isolated lines that are also found in the HITRAN 2012 database. The number of lines found for each temperature is given in Table 14.

FREQUENCY CALIBRATION

The positions of the lines measured were calibrated to those of the HITRAN linelist. In order to do so, up to 25 strong, isolated lines were chosen that appear both in the experimental list and HITRAN. It is necessary to choose isolated lines, that is to say lines which do not overlap with other lines, because other lines interfere with the lineshape and potentially the line center (the position). Such lines would not be suitable for calibration as there is uncertainty in the location of the line. Table 15 summarizes the frequency calibration. For calibration, a ratio of the line positions from experiment and from HITRAN was taken to obtain an averaged linear factor through which all line positions could be multiplied.

INTENSITY CALIBRATION

The intensities of the lines obtained from the raw spectra have arbitrary units. In order for the linelists to have intensities that are useful quantitatively, they must first be calibrated. Similar to the calibration of the line position, calibration of line intensity is done by comparison to HITRAN.

However, calibration for intensity was carried out by comparison between all available lines. A line is considered suitable for calibration if the difference in calibrated line position is $\pm 0.002 \text{ cm}^{-1}$. For each temperature, a calibration factor is provided from the gradient of a plot of experimental intensity vs. HITRAN intensity, as can be seen in Figure 42. A summary of the intensity calibration factors is provided in Table 15 and this factor is used to give the experimental intensities useful units.

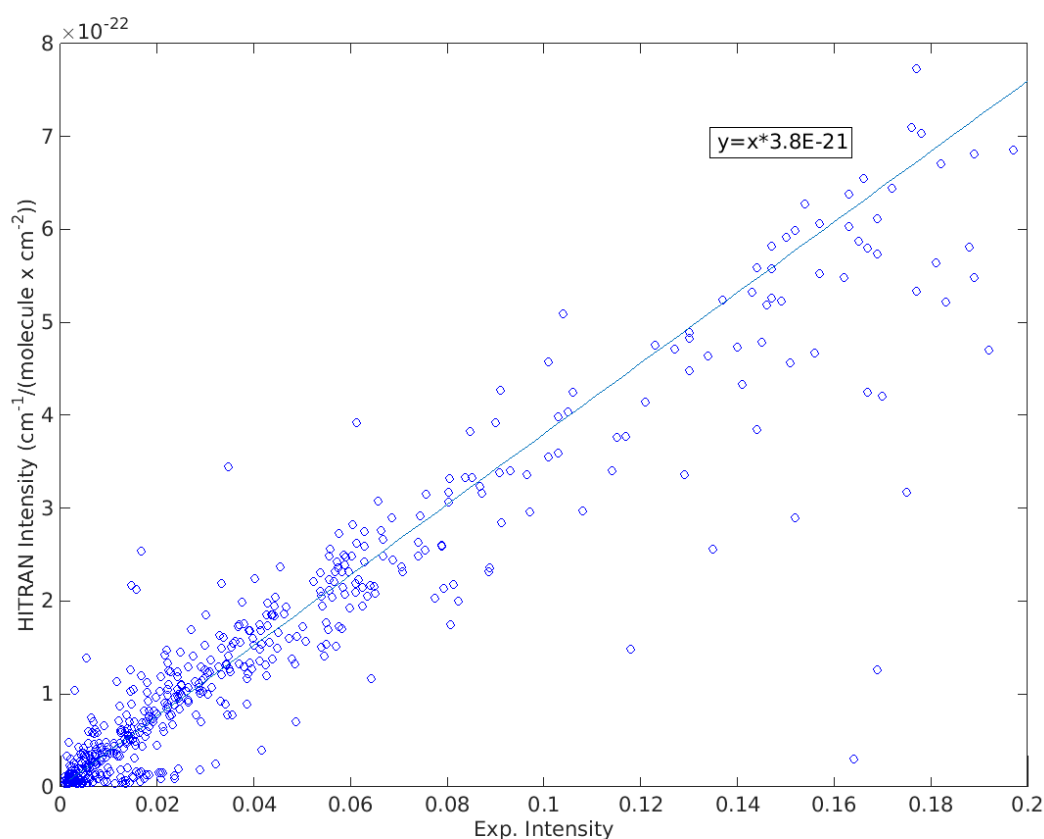


Figure 42. Intensity calibration plot for 500 K at 10 Torr for the higher wavenumber region. The calibration factor is the value of the trend line, which for example with this calibration is 3.8×10^{-21} .

Table 15. Linear calibration factors for experimental line positions and intensities for each temperature in the low wavenumber region.

| Temperature (K) | Position Calibration Factor | Intensity Calibration Factor (x 10 ⁻¹⁷ molecule cm ⁻¹) |
|-----------------|--------------------------------|--|
| 296 | 1.000000871 | 5.11 |
| 473 | 1.000000788 | 2.95 |
| 573 | 1.000000749 | 3.92 |
| 673 | 1.000000769 | 1.94 |
| 773 | 1.000000772 | 1.84 |
| 873 | 1.000000814 | 2.56 |
| 973 | 1.000000833 | 8.88 |

EFFECT OF TEMPERATURE ON INTENSITY

The line intensity equation gives the line intensity as a function of temperature:

$$S' = \frac{2\pi^2\nu_{10}S_{JJ''}}{2\varepsilon_0hcQ} \exp\left(-\frac{E''}{kT}\right) \left[1 - \exp\left(-\frac{h\nu_{10}}{kT}\right)\right] \quad (24)$$

where ν_{10} is the line frequency, $S_{JJ''}$ is the line strength, ε_0 is the permittivity of free space, h is Planck's constant, c is the speed of light, Q is the internal partition function, E'' is the lower state energy, k is the Boltzmann constant and T is the temperature (Bernath, 2005). To compare the room temperature HITRAN linelist to lines obtained at high temperatures, the HITRAN data was extrapolated using Equation 24 with the lower state energies from (Yurchenko *et al.*, 2011).

Table 16. Partition function for NH₃ (low wavenumber range) (*Yurchenko et al.*, 2011).

| Temperature (K) | Partition function |
|-----------------|--------------------|
| 296 | 1725.225 |
| 473 | 3711.930 |
| 573 | 5271.335 |
| 673 | 7259.686 |
| 773 | 9788.208 |
| 873 | 12989.473 |
| 973 | 17021.824 |

If a line is measured at different temperatures, the intensity of the line at each temperature may be compared to the intensity at a reference temperature by taking a ratio of the line intensity equation:

$$\frac{S'}{S'_0} = \frac{Q_0}{Q} \exp\left(\frac{E''}{kT_0} - \frac{E''}{kT}\right) \left[\frac{1 - \exp\left(-\frac{h\nu_{10}}{kT}\right)}{1 - \exp\left(-\frac{h\nu_{10}}{kT_0}\right)} \right] \quad (25)$$

where S'_0 and T_0 refer to the line intensity and temperature of the reference measurement. For these results, 773 K was used as the reference as this temperature contained the most lines with which to compare the line intensities of other temperatures. If there was no line measured at 773 K, then the reference used was the temperature with the next greatest number of lines. The partition function used for NH₃ was obtained from *Yurchenko et al.* (2011) and the values for each temperature are given in Table 16.

RESULTS FOR LOW FREQUENCY REGION

Forty Torr (0.053 atm) of NH_3 was used in the sample cell for these measurements in order to observe weaker transitions. However, at this pressure, many strong lines become saturated, particularly in the Q branch of the ν_1 fundamental mode and the lines are pressure-broadened. The resulting line lists are provided at each temperature and contain line position, line intensity and lower state energy (if calculated). For observed lines that could be assigned using the MARVEL or HITRAN line lists, the corresponding position, intensity, lower state energy and quantum number assignment is provided. Observed saturated lines, for which accurate positions and intensities could not be measured, were excluded and replaced with HITRAN lines with intensities greater than 2.0×10^{-20} cm molecule⁻¹. The experimental positions were calibrated to strong lines in HITRAN, and the mean difference between all matched lines is approximately 4.0×10^{-4} cm⁻¹ with a standard deviation of 3.0×10^{-4} cm⁻¹ after calibration. Similarly, the accuracy of the intensities of the experimentally obtained lines is measured by comparison with matched HITRAN lines; for these the mean difference is within 20 %.

The top panels of Figures 43 and 44 show overviews of the recorded spectra at 296 and 773 K, respectively. The middle panels show simulated spectra from the BYTe line list and the bottom panels similarly show simulated spectra from the HITRAN line list. The spectral simulation uses the Reference Forward Model (*Dudhia, 2017*), a line-by-line radiative transfer model, to calculate the transmission through a 50 cm cell with the experimental pressure and temperature. Individual line broadening parameters for the lines in BYTe were obtained as averages from HITRAN 2012 and applied to all lines. The HITRAN spectral simulation uses the line positions and intensities from HITRAN 2012 as well as the averaged broadening parameters applied globally, therefore allowing for comparisons between HITRAN, BYTe and our measurements. HITRAN is a linelist

produced using a combination of experimental and theoretical data sets. Line positions are generally very good in HITRAN, however, although the line intensities may be extrapolated for temperature using Equation 24, the database is missing many hot or overtone bands which are important for high temperature studies. BYTe is a purely *ab initio* linelist. It includes many more lines than can be measure experimentally and includes the hot bands and overtones missing in HITRAN, although the accuracy of the line positions is less reliable than HITRAN. The linelists produced from the work in this chapter include the fundamental, hot and overtone bands that are important for high temperature studies. Line positions are determined to high accuracy.

The experimental spectrum at 296 K (Figure 43) shows some saturated lines of the ν_1 fundamental, $\nu_1+\nu_2/\nu_2+\nu_3$ and $\nu_1+\nu_4/\nu_3+\nu_4$ modes which have been replaced in the final line list. In general, there is good agreement between the three spectra at 296 K. This is expected due to the fact that HITRAN is designed to be used at room temperature. For 773 K, the experimental and BYTe spectra in Figure 44 clearly show a number of additional hot bands that are not present in the HITRAN spectrum, most notably the Q-branch of the $\nu_1+3\nu_2-2\nu_2$ band at around 3850 cm^{-1} and the $2\nu_2+\nu_3-\nu_2$ band from 4000 cm^{-1} to 4200 cm^{-1} . In fact, there are clearly no HITRAN lines in the $3600\text{--}4000\text{ cm}^{-1}$ region. Both the BYTE and experimental spectra show the existence of hot band lines in this region. Other hot bands are included in the $3000\text{--}3600\text{ cm}^{-1}$ regions and $4200\text{--}4700\text{ cm}^{-1}$ regions although they are not shown because of the density of lines. Some lines in HITRAN have an incorrect lower state energy which can be seen clearly in Figure 44 at, for example, around 4650 cm^{-1} (indicated by the blue arrow) where the extrapolated intensity (Equation 24) is incorrect due to an incorrect lower state energy (seen in Figure 47 circled in red). This work has helped identify a number of such errors.

A more detailed view of short segments of the three spectra is shown in Figures 45 and 46. Figure 45 again shows the three spectra for 296 K. There are a number of lines that assignable in both the experimental and BYTe spectra; one example being the strong line at 4151.8 cm^{-1} (the R(6) line of the $\nu_1 + \nu_2$ band) that appears in all three spectra within 0.1 cm^{-1} with a similar intensity. Even at room temperature, however, there are a number of lines in the experimental spectrum that are missing from HITRAN and a number of inconsistencies between the experimental spectrum and the BYTe simulation.

Lines in the experimental line lists which have been matched to lines in either reference line list are marked by an asterisk. At 773 K, the hot lines in the experimental spectrum at 4141.0 cm^{-1} , 4147.4 cm^{-1} and 4153.2 cm^{-1} can be matched to lines in the BYTe spectrum, although their positions are shifted as there is uncertainty in the position of the vibrational band centers. In this region the shift is over 1 cm^{-1} towards higher wavenumbers, although in other regions the shift value and direction vary. While the strong lines can be identified, it becomes more problematic to assign weaker features from BYTe primarily due to the observed shifts. The lines in Figure 46 which are not matched (i.e., those without an asterisk) include a number of strong lines, and these are mostly hot lines. This demonstrates the difficulty in assigning lines in regions with overlapping hot bands where the line position from calculated spectra is of insufficient accuracy. Line positions may be more quantitatively compared by using the method of combination differences (Bernath 2005). However, this method is effort intensive and this more thorough analysis was not utilized due to time constraints.

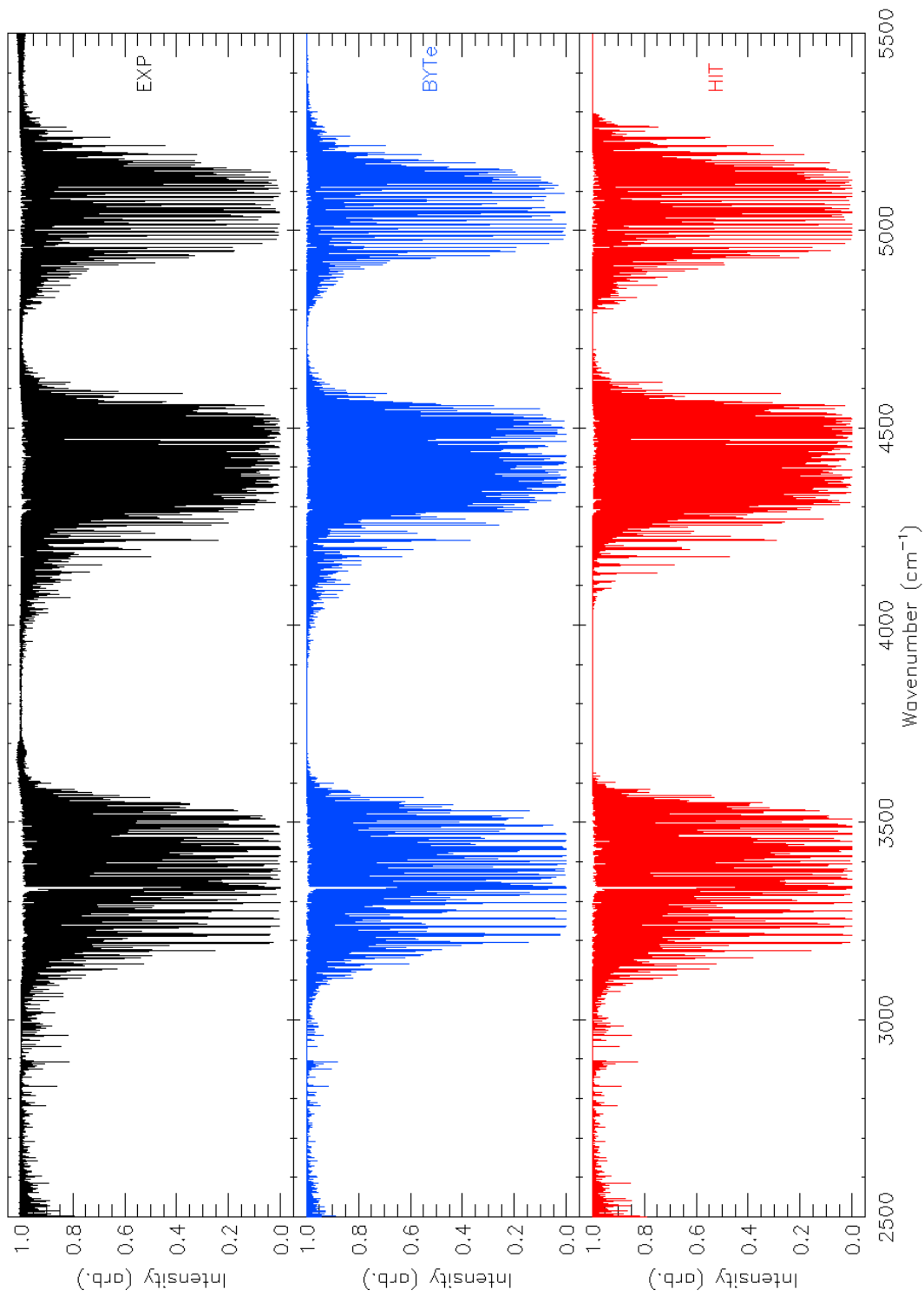


Figure 43. Overview of spectra of NH₃ showing experimental data (top panel) and simulated spectra created to match the conditions of the experiment from the BYTe (center panel) and HITRAN (lower panel) line lists at 296 K (Beale *et al.*, 2017).

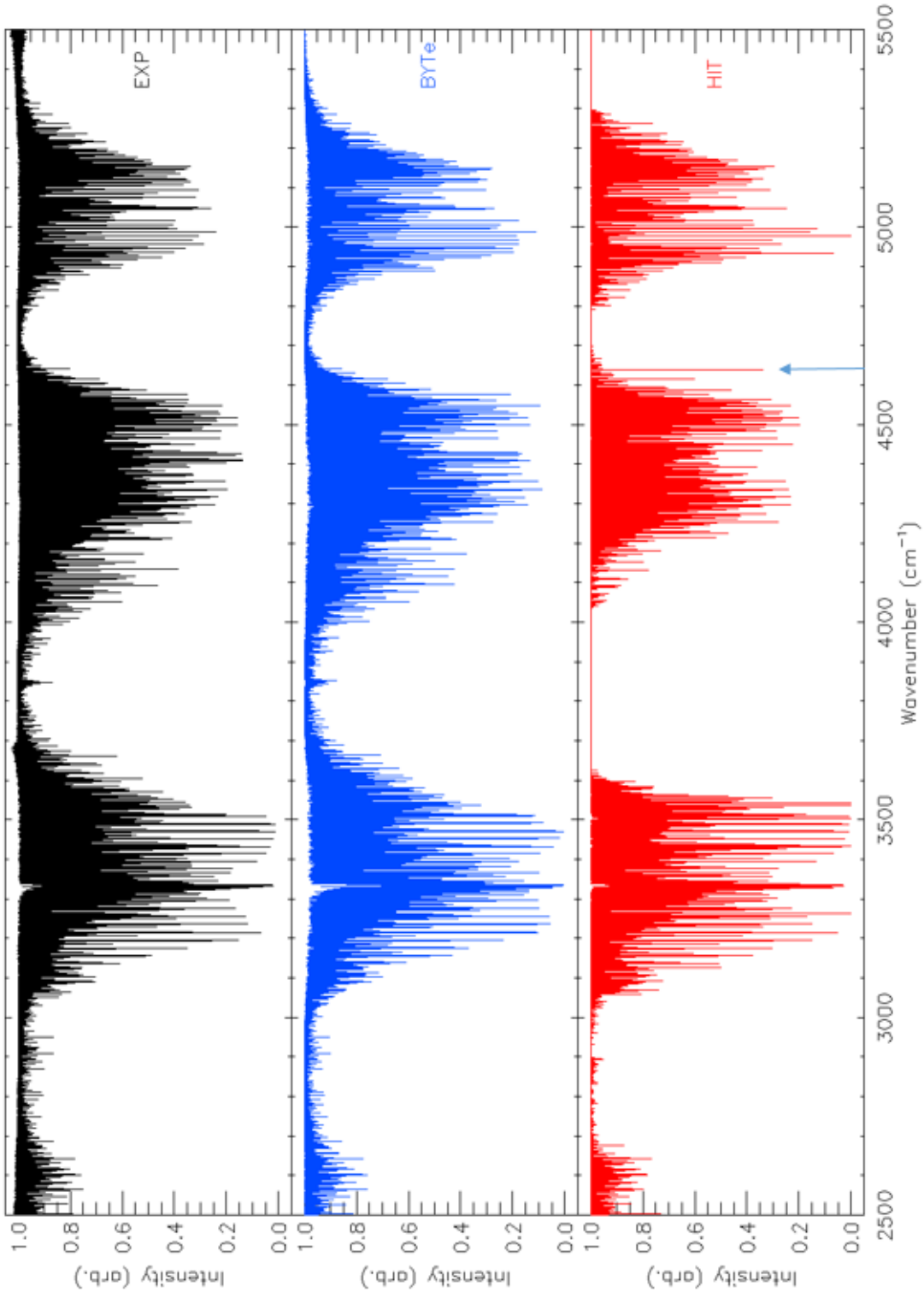


Figure 44. Overview of spectra of NH₃ showing experimental data (top panel) and simulated spectra created to match the conditions of the experiment from the BYTe (center panel) and HITRAN (lower panel) line lists at 773 K (Beale *et al.*, 2017).

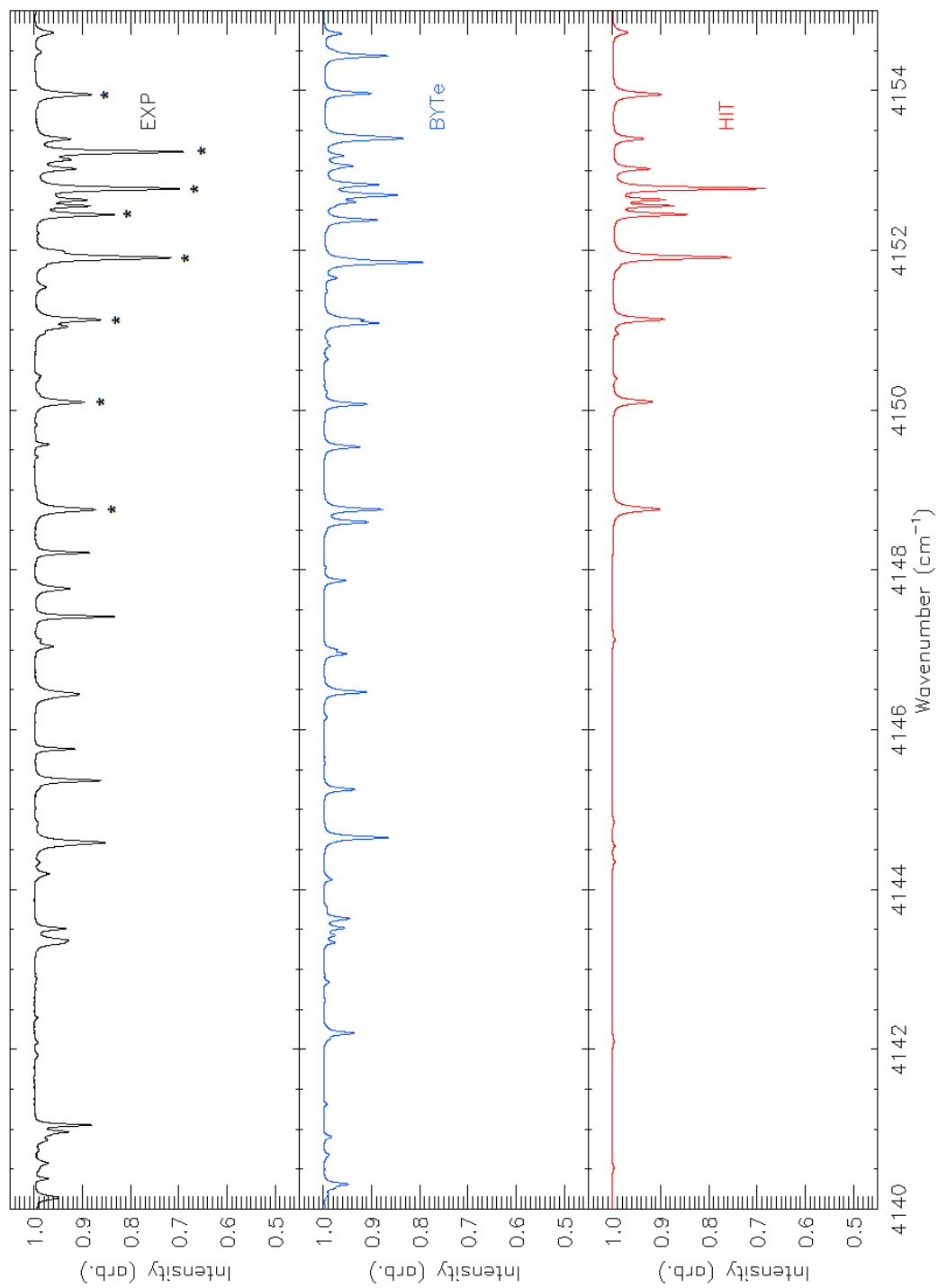


Figure 45. Detailed spectra of NH_3 showing experimental data (top panel) and simulated spectra created to match the conditions of the experiment from the BYTe (center panel) and HITRAN (lower panel) line lists at 296 K. Experimental lines that have been assigned by matching are marked by asterisks (Beale *et al.*, 2017).

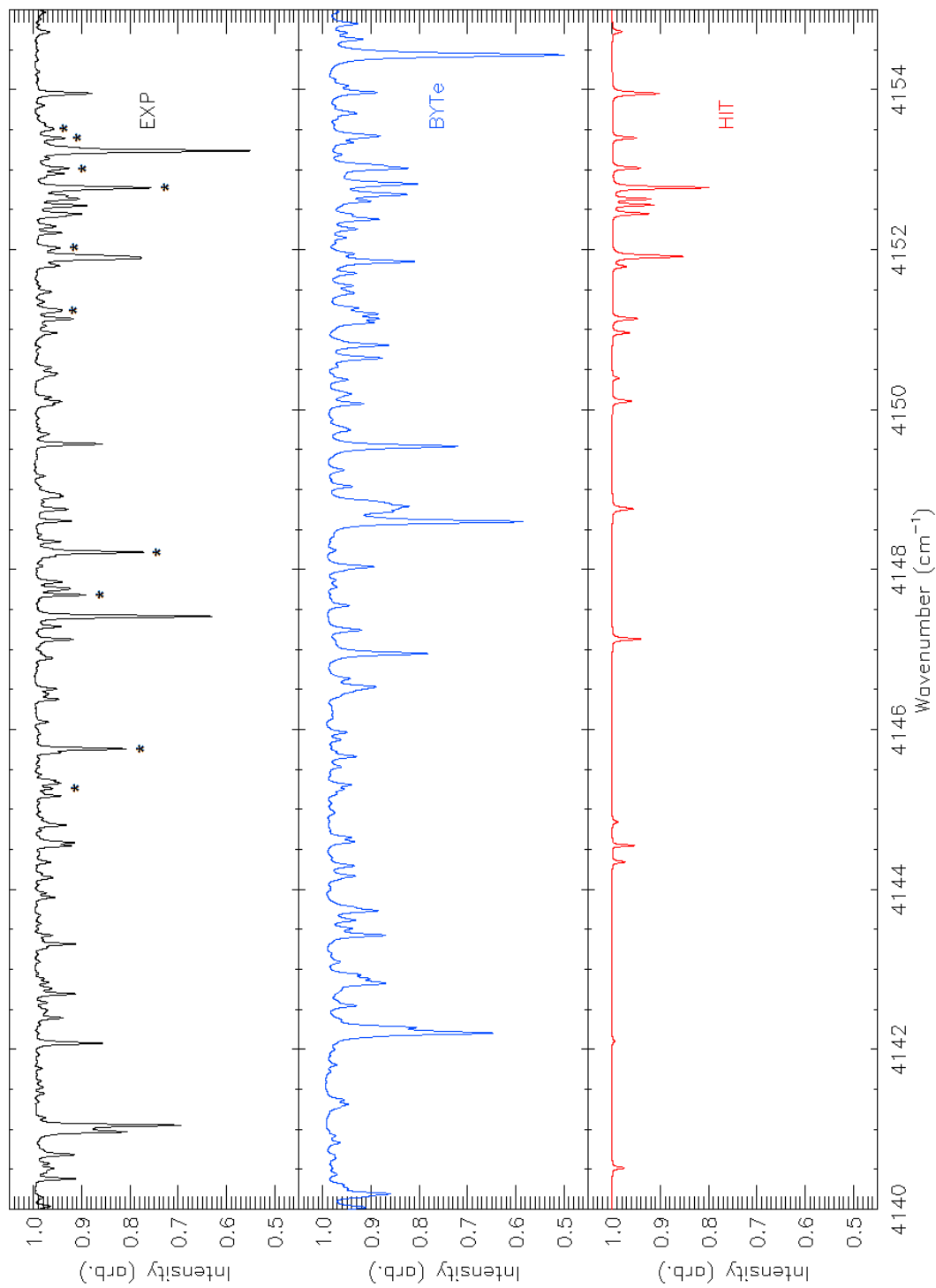


Figure 46. Detailed spectra of NH₃ showing experimental data (top panel) and simulated spectra created to match the conditions of the experiment from the BYTe (center panel) and HITRAN (lower panel) line lists at 773 K. Experimental lines that have been assigned by matching are marked by asterisks (Beale *et al.*, 2017).

LOWER STATE ENERGIES

The line intensity equation (equation 24) gives the intensity of a line as a function of the partition function, the lower state energy and the temperature of the gas. If the intensity of a given line is known at multiple temperatures, the lower state energy can be obtained from a rearranged version of the line intensity equation:

$$\ln \left(\frac{SQ}{S_0 Q_0} \left[\frac{1 - \exp\left(-\frac{h\nu_{10}}{kT}\right)}{1 - \exp\left(-\frac{h\nu_{10}}{kT_0}\right)} \right] \right) = \frac{E''}{kT_0} - \frac{E''}{kT} \quad (26)$$

where the intensity ratio on the left hand side can be plotted against $1/kT$. Plotted for multiple temperatures, the gradient of this line gives the lower state energy.

The empirical lower state energies are plotted against line position in Figure 47 in the lower panel along with those from HITRAN in the upper panel. The near-vertical lines belong to Q branches and the parabolic features the left and right of the Q-branches are from the P and R branches, respectively.

There are a number of notable differences between the HITRAN lower state energies and those obtained by experiment (Figure 47). The incompleteness of HITRAN can be seen between 3600 and 4100 cm^{-1} , experimental data has been obtained in this region. There are also very few lower state energy values listed in HITRAN with energies above 2000 cm^{-1} ; some of these are from fundamental and combination transitions and can be seen in the bottom panel, particularly the Q branch of the ν_1 band and the P and R branches of the $\nu_1 + \nu_2$ band. However, most of the lines with high lower state energies are from hot transitions. The most notable 'hot' band in the lower panel is the strong Q branch at a position 3850 cm^{-1} , extending from a lower state energy of 2000-3000 cm^{-1} , which is not provided in HITRAN. This feature can be seen in the 773 K NH_3 spectra in

Figure 44 in both the experimental data (top) and BYTe (center) panels and not in the HITRAN (lower) panel.

The MARVEL analysis of NH_3 (*Al Derzi et al.*, 2015) and re-analysis of the HITRAN NH_3 database (*Down et al.*, 2013) are line lists in the region of interest which contain quantum number assignments. MARVEL provides a self-consistent list of fully assigned line positions, but no associated line intensities. Therefore, rather than using MARVEL directly, the MARVEL adjusted BYTe linelist BARVEL (produced by Phillip Coles, University College London) was used, which was computed by replacing BYTe energies with the corresponding values from MARVEL. Disregarding the 13% of MARVEL states that could not be matched to corresponding BYTe states, BARVEL provides intensity data for roughly 18,500 (66%) of MARVEL transitions, plus many predicted transitions between MARVEL energy levels that have not been observed experimentally. The remaining linelist consists of transitions for which either one or both of the energy states takes its energy from BYTe. Other transitions for which both upper and lower state had their values taken from MARVEL were used, to avoid any discrepancies in line positions due to the inaccuracy of BYTe. As a result BARVEL provides the MARVEL linelist with line intensities from BYTe and may therefore be compared with the experimental linelist.

The positions and intensities from these lists may be compared to those obtained experimentally to provide tentative assignments. Lines with positions within 0.002 cm^{-1} and intensities between 0.5 and 2.0 times that of the experimental lines were considered matched, with the number of assigned lines from each reference list given in Table 14, it should be noted that many of these assignments are for the same lines at different temperatures. Figure 48 shows the comparison of lower state energies from matched lines.

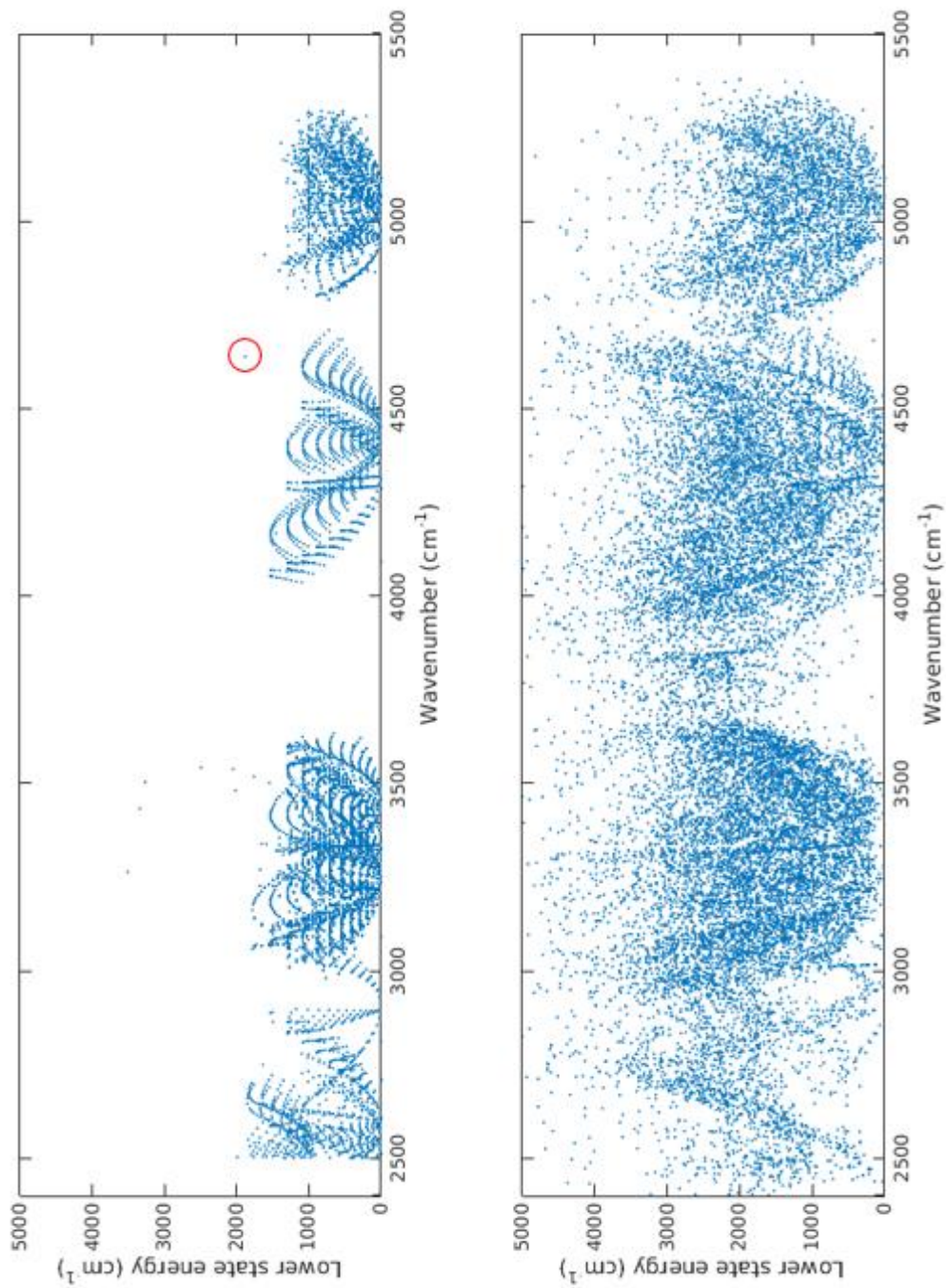


Figure 47. Comparison of lower state energies from the HITRAN line list (Rothman *et al.* 2013) (top panel) and from the experimental line list (lower panel) as a function of line position (Beale *et al.*, 2017).

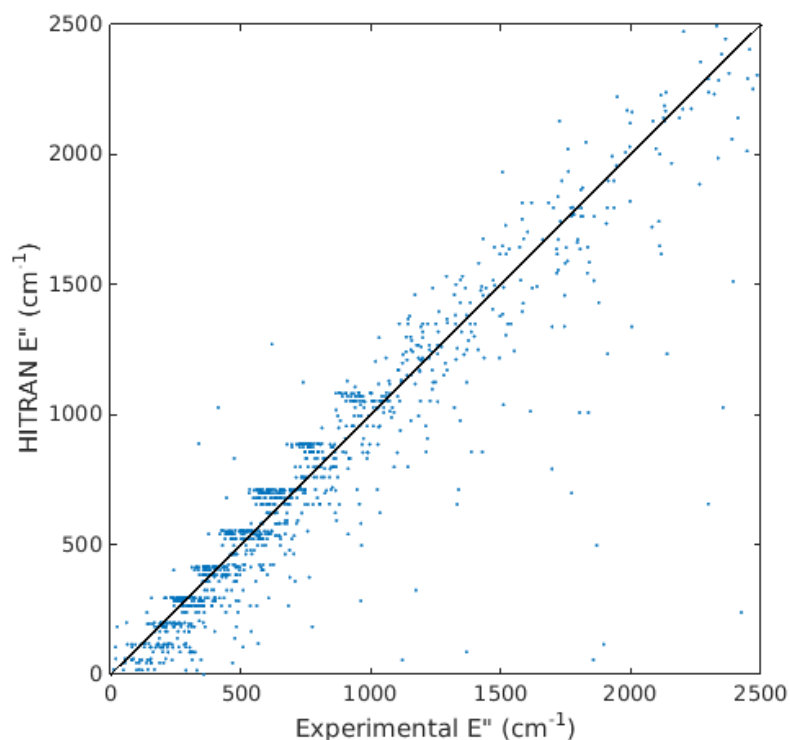


Figure 48. Comparison of matched lower state energies obtained from experiment (x-axis) and the HITRAN re-analysis of Down *et al.* (2013) (y-axis). Figure from (Beale *et al.*, 2017).

TRANSMISSION SPECTRA OF NH₃ IN THE 4800-9000 CM⁻¹ REGION

The 2400-5500 cm⁻¹ region contains the ν_1 and ν_3 modes, as well as a number of combinations and overtones. The 4800-9000 cm⁻¹ region contains no fundamental modes, only combinations or overtones of the four fundamental modes listed in Table 12. At a given temperature, the populations of the states of the overtone or combination transitions are lower and therefore the intensity of transitions in this region are generally lower than those of the 2400-5500 cm⁻¹ region. In order to compensate for the varied band intensities, the spectra in this higher wavenumber region were recorded at two pressures, 10 Torr (0.0132 atm) and 100 Torr (0.132 atm).

Pressure has two main effects on a spectrum. Increased pressure results in more of the sample gas and therefore stronger absorption of the lines. However, as discussed in Chapter III, higher pressure results in increased line width. In this higher wavenumber region, the 100 Torr spectra allow the weaker lines to be visible at the expense of line width. For a molecule such as ammonia, which has a congested spectrum, increased line width can result in a number of blended lines resulting in uncertainty in the position and intensity of individual lines.

The temperatures used for the higher wavenumber region were changed to give a range that suffered less from decomposition of the sample that was identified in the lower wavenumber region at 973 K. For this reason, the maximum temperature used was 900 K, with an additional low temperature spectrum at 400 K.

EXPERIMENTAL

The basic experimental setup was not changed from the lower wavenumber region, although the filter was changed to silicon.

Table 17. Experimental conditions for NH₃ high wavenumber region

| Parameter | Value |
|-------------------------------------|------------------|
| Spectral region (cm ⁻¹) | 4800-9000 |
| Detector | InSb |
| Beamsplitter | CaF ₂ |
| Spectrometer Windows | CaF ₂ |
| Lens | CaF ₂ |
| Filter | Si |
| Scans | 300 |
| Resolution (cm ⁻¹) | 0.01 |
| NH ₃ Pressure (Torr) | 10/100 |
| Zerofilling factor | x 16 |

Transmission spectra were recorded as per Equation 23 and water lines removed as described in Chapter III. An additional interference filter was used for this region to block all wavenumbers below 5000 cm^{-1} . Using WSpectra, lines were picked from $4800\text{--}9000\text{ cm}^{-1}$ for the 10 Torr spectra and from $5500\text{--}9000\text{ cm}^{-1}$ for the 100 Torr spectra. The combination band around 5300 cm^{-1} was not included for line selection for the higher pressure spectra as this region was on the edge of the region and suffers from low signal-to-noise (Figure 49).

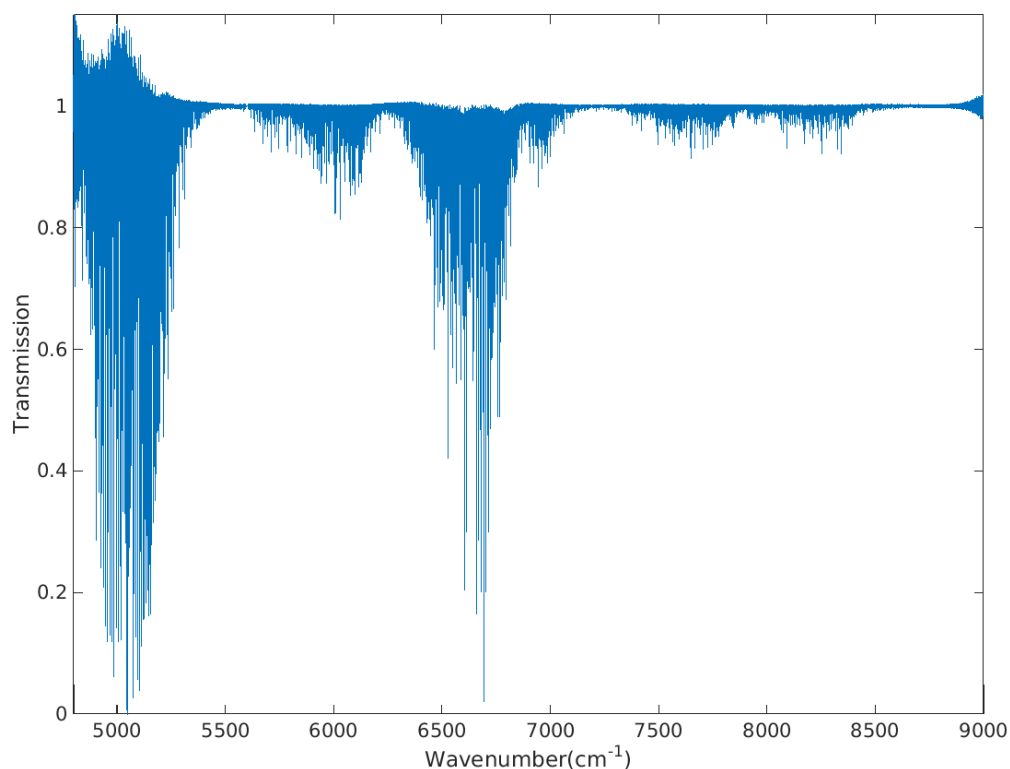


Figure 49. Transmission spectrum of 100 Torr of NH_3 at 700 K in the high wavenumber region. The noise for most of this region is under $\pm 0.2\%$, at 5200 cm^{-1} and below, the noise ranges up to $\pm 15\%$, which combined with high pressure results in lines with poorly determined line positions and intensities.

For the 100 Torr spectra, the low signal-to-noise ratio of this region resulted in larger uncertainty in line intensity and position making analysis difficult and unreliable. Since this band is relatively

strong, the line positions and intensities from the 10 Torr spectra as well as from the edge of the 2400-5500 cm^{-1} spectra are sufficient to provide a suitable line list for this band.

The calibration method for both wavenumber and intensity was the same for the high wavenumber region as for the low wavenumber region. Line intensities are obtained using WSpectra, which applies a non-linear least squares fit, line-by-line, using the exponential of a theoretical Voigt profile. The output of this fit are the raw line intensities (in arbitrary units) which are then calibrated to HITRAN values. These calibration factors are summarized in Table 19. The partition function used for this wavenumber range, detailed in Table 18, is an updated NH_3 partition function from Sousa-Silva (2014).

Table 18. Calibration factors for experimental line positions and intensities for each temperature and pressure in the high wavenumber region.

| Temperature | 10 Torr Pos. | 10 Torr Int. Calib. | 100 Torr Pos. | 100 Torr Int. Calib. |
|--------------------|----------------------|---|----------------------|---|
| (K) | Calib. Factor | Factor ($\times 10^{-21}$ molecule cm^{-1}) | Calib. Factor | Factor ($\times 10^{-21}$ molecule cm^{-1}) |
| 293 | 1.000000081 | 2.14 | 1.000000094 | 1.01 |
| 400 | 1.000000083 | 2.78 | 1.000000096 | 0.99 |
| 500 | 1.000000125 | 3.83 | 1.000000100 | 1.42 |
| 600 | 1.000000116 | 3.53 | 1.000000063 | 1.30 |
| 700 | 1.000000115 | 4.56 | 1.000000090 | 1.29 |
| 800 | 1.000000065 | 7.18 | 1.000000099 | 1.41 |
| 900 | 1.000000109 | 3.10 | 1.000000083 | 1.51 |

Table 19. Partition function for NH₃ (high wavenumber range).

| Temperature (K) | Partition function |
|-----------------|--------------------|
| 293 | 1689.3 |
| 400 | 2778.5 |
| 500 | 4081.7 |
| 600 | 5742.9 |
| 700 | 7860.3 |
| 800 | 10550.0 |
| 900 | 13951.0 |

RESULTS FOR HIGH FREQUENCY REGION

A sample of these spectra (293 K at 10 Torr) is presented in Figure 50. Once calibrated, the line intensities should be same regardless of pressure. As such, a check may be made by plotting the calibrated intensity of a spectrum recorded at 10 Torr against that of a spectrum recorded at 100 Torr (Figure 51). Once a calibrated linelist was obtained for each temperature and pressure, lower state energies could be calculated for this region using Equation 25. The experimental lower state energies obtained are presented in Figure 52 with comparison to HITRAN in the regions possible. The HITRAN linelist for NH₃ is currently limited to 7000 cm⁻¹ making a comparison difficult. From Figure 52 it is clear that this work adds substantially to the measured bands of NH₃ in the near infrared.

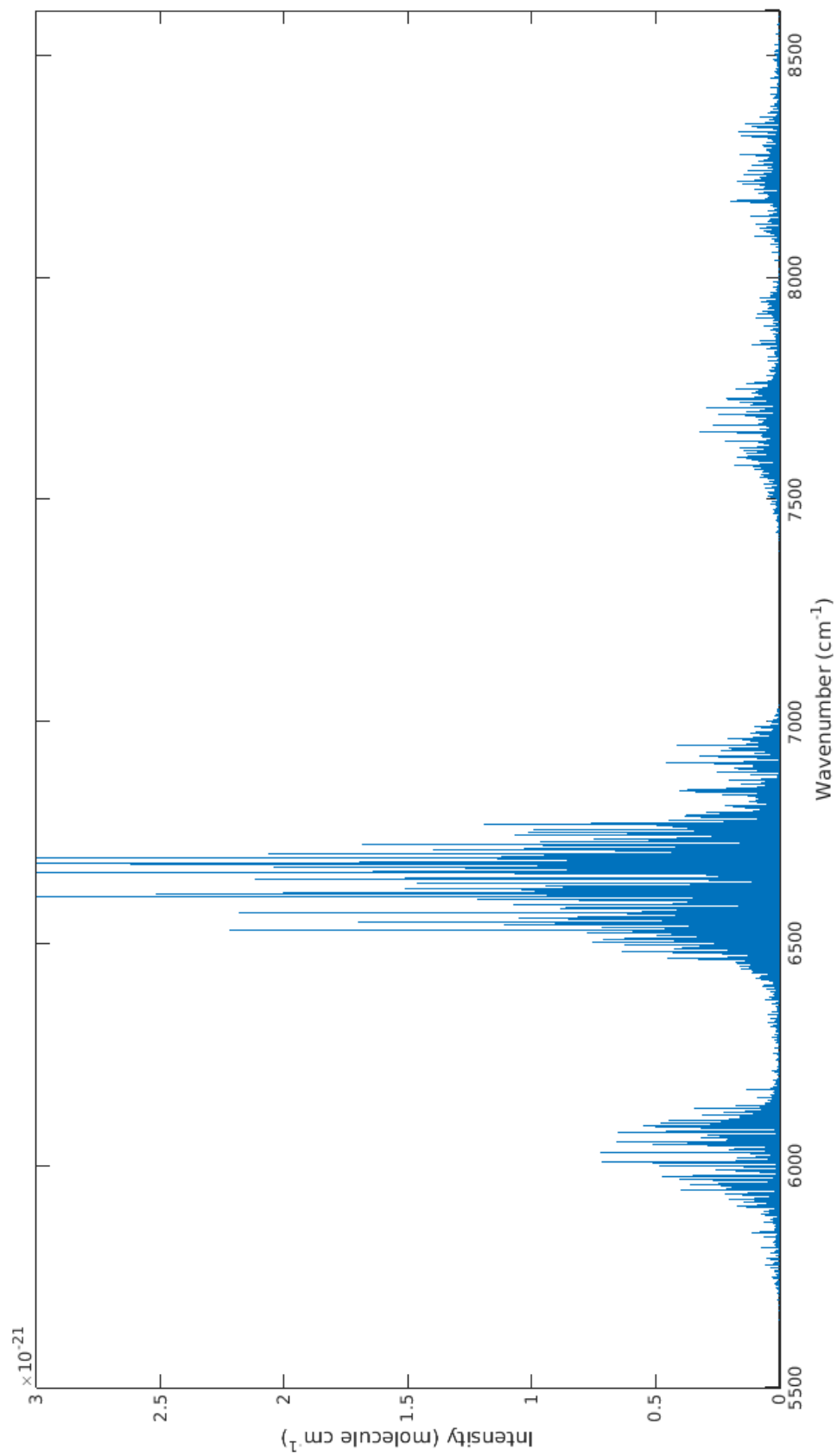


Figure 50. Spectrum of NH₃ at a temperature of 293 K and pressure of 10 Torr. This spectrum has been calibrated for both wavenumber and intensity.

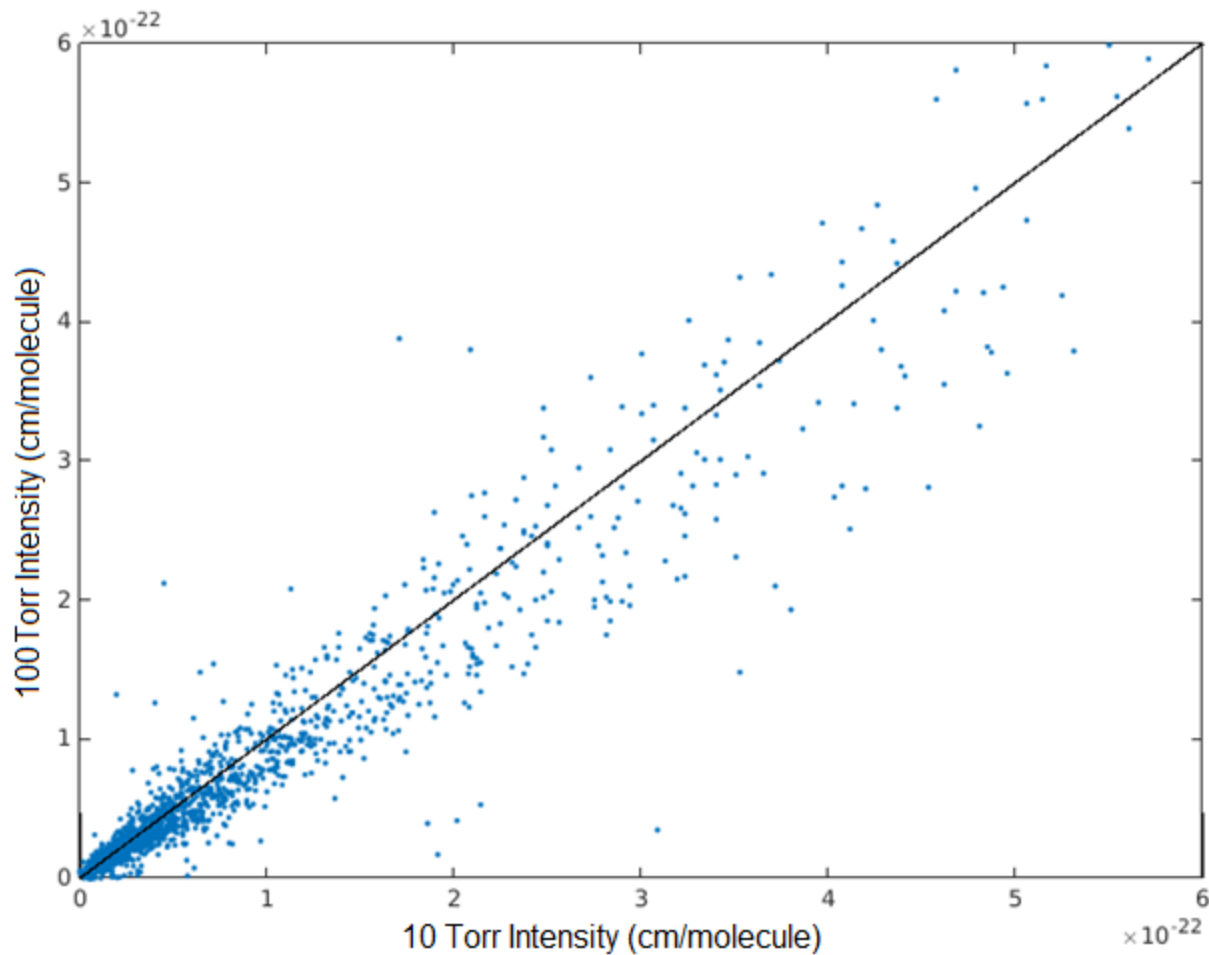


Figure 51. Comparison of calibrated intensities from both pressures and a 1:1 trend line.

The BYTe theoretical linelist extends up to 12000 cm^{-1} , however the accuracy in line position in this region is poor with a claimed accuracy above 5000 cm^{-1} of only 5 cm^{-1} (*Polyansky et al.*, 2016). Such inaccurate data makes quantum assignment very difficult as the density of lines in this region is very high.

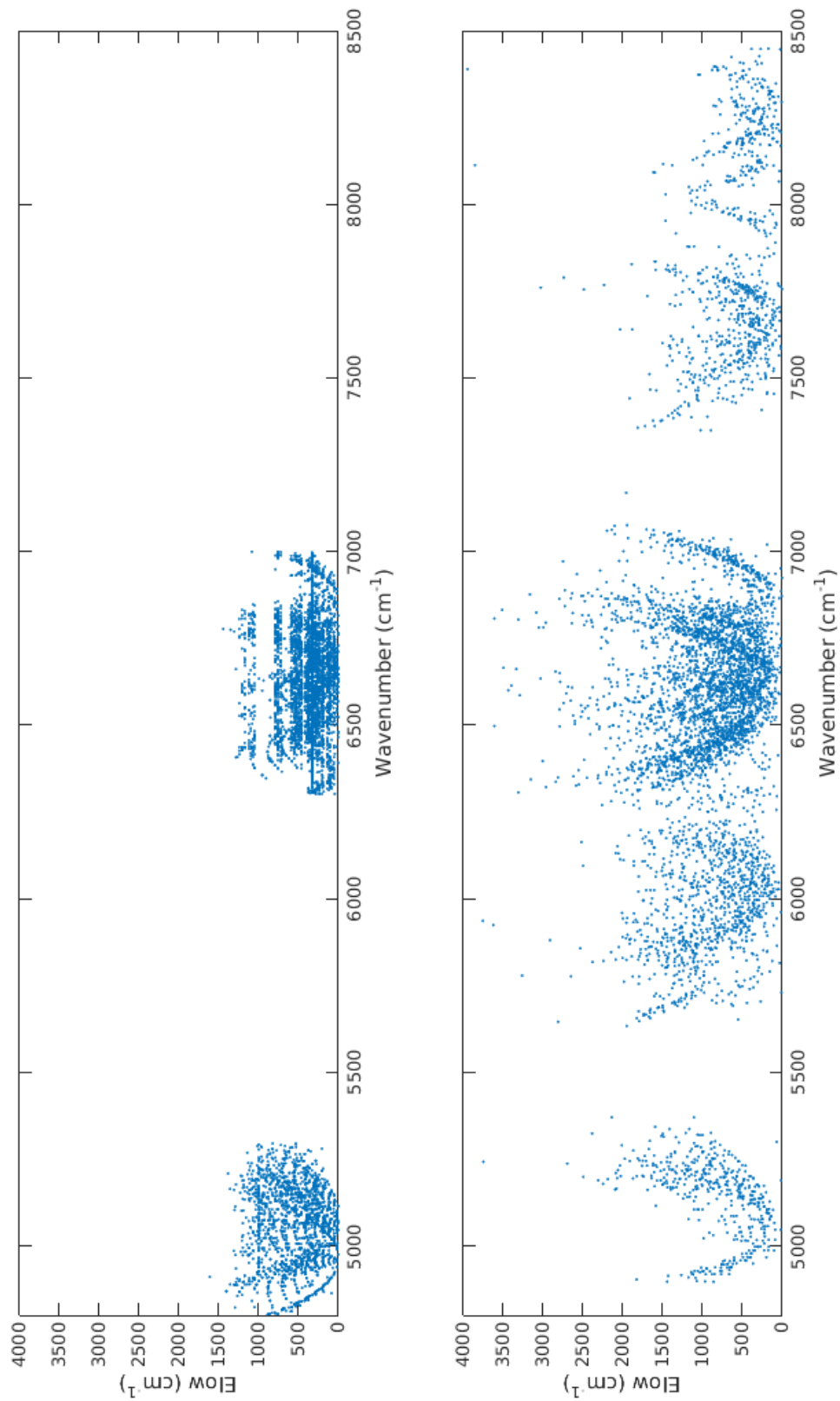


Figure 52. Lower state energy plot of the high wavenumber region (lower) as compared to HITRAN (upper). Note the lack of coverage in the HITRAN database throughout this region and at higher lower state energies.

CONCLUSION

High resolution transmission spectra of ammonia recorded at seven temperatures between 296 K and 973 K were used to calculate lower state energies in the 2400-5500 cm^{-1} region and between 293 K and 900 K in the 4800-9000 cm^{-1} region. These spectra include several hot bands which are not present in HITRAN even at room temperature with tentative assignments of J up to 22. Therefore, this work currently provides the most accurate line list for simulating room temperature (and higher) NH_3 observations in this spectral region. Extrapolating room temperature HITRAN results to higher temperatures results in a substantial decrease in total intensity as the hot bands are not included (Figure 46) and this work provides intensity estimates for the hot bands in this region.

Calculated line lists such as BYTe (*Yurchenko et al.*, 2011) provide more lines than are experimentally observable due weakness of millions of lines in the spectrum and the sensitivity required to measure them. Calculations give a much more complete total intensity sum over multiple bands, however, positions of individual lines in BYTe are less well determined than in the experiment measurements. The lower wavenumber region has been compared to HITRAN and BYTe as there is extensive and accurate coverage for this region. As these databases have low or inaccurate coverage in the higher wavenumber region, limited comparison has been made.

The experimental line lists obtained can be used directly in atmospheric models for brown dwarfs and exoplanets. The line lists can also be used to create template spectra for cross correlation with high resolution spectra of planetary systems. The cross correlation method for detecting molecules on exoplanets, such as those used to detect CO on HD 209458 (*Snellen et al.*, 2010) by analyzing Doppler-shifted spectral features of a transiting exoplanet, require high resolution template spectra

with accurate line positions and intensities. The line lists of this work satisfy both the high temperature and high resolution requirements for current exoplanetary research.

CHAPTER VII

CONCLUSIONS AND FURTHER WORK

This dissertation has detailed the use of high resolution spectroscopy in atmospheric science and presented the first global isotopic measurements of ^{13}CO in the atmosphere, the most complete and accurate experimental spectroscopic studies of hot propane in the 3000 cm^{-1} region and hot ammonia in the $2400\text{-}9000\text{ cm}^{-1}$ region. On Earth, for remote sensing using the ACE-FTS, high resolution data has enabled isotopic fractionation to be measured but the current linelists for ^{13}CO are perhaps the limiting factor in the determination of truly quantitative results. Use of WACCM has enabled comparison with the ACE data. Three different improvements would perhaps result in more reliable results for fractionation. The ACE 3.5 dataset was used in the analysis in Chapter IV. The current 3.6 dataset includes additional data from 2012 to 2017 and the upcoming 4.0 dataset will represent improved data with better retrievals may allow more quantitative results for isotopic fractionation of ^{13}CO and C^{18}O , and may also result in somewhat better results for the fractionation of C^{17}O for which the current dataset is insufficient (Figure 30). In addition, the retrievals process has demonstrated that improved linelists for ^{13}CO are required for more reliable values for the volume mixing ratio profiles; small errors in line intensities can produce large errors in δ -values. Finally, additional validation of ACE retrievals of CO isotopologues are required for a truly quantitative analysis. Comparison with ground based, balloon or other satellite data are required, however such data do not yet exist for all altitudes as they do for isotopologues of other molecules in the ACE dataset, such as CH_4 and N_2O .

The success of high resolution spectroscopic data for analyzing Earth's atmosphere has been established. Since the discovery of exoplanets and brown dwarfs, several molecules have been detected in their atmospheres. With the advent of more advanced astronomical instruments with ever higher resolving power observing these objects, as well as the JIRAM instrument on the Juno satellite, mean that high resolution linelists and cross-sections such as those obtained in this work may now be used to detect yet more molecules or more accurately determine the conditions of these objects. To this end, high resolution cross-sections have been recorded for propane in the C-H stretching region at high temperatures. This molecule is one of a number of hydrocarbons in Jupiter's auroral regions which the JIRAM instrument will study.

Finally, linelists have been recorded for NH_3 in the 2400-9000 cm^{-1} region. NH_3 is a key molecular species in the atmospheres of cool stars and is predicted by a number of thermodynamic models to be present in the atmospheres of exoplanets. Both of these environments exist at elevated temperatures for which room temperature linelists are not sufficient. In addition, *ab initio* linelists for NH_3 do not have the required accuracy for line positions, especially at higher wavenumbers and for the hot bands which become increasingly intense at higher temperatures. As such the data which was collected as described in this dissertation are crucial for the potential detection of NH_3 in exoplanets and for the characterization of Y type brown dwarfs. The accuracy of this data ($\pm 0.005 \text{ cm}^{-1}$ for line position, within a factor of 2 for intensity) is important for inclusion in atmospheric models of exoplanets and brown dwarfs.

Lower state energies allow the extrapolation of line intensity with temperature (Equation 24). The method presented in this dissertation allows the calculation of experimental lower state energies by comparing the strength of a line at multiple temperatures. Experimental lower state energies are useful, but limited. Those obtained here are not of high enough accuracy for quantum number

assignment, which is a strength of the *ab initio* approach. The linelists recorded should be used to constrain the vibrational band centers of higher wavenumber modes, especially combination and hot band modes. A more complete combination of an experimental-theoretical linelist for NH₃ in the infrared is required for the best line by line input data for radiative transfer models. This would involve more quantum number assignment in the lower and higher wavenumber ranges as presented here, including use of combination differences. The linelists obtained should also be extended towards the visible to complete the coverage of high resolution data obtained to match that of the astronomical instruments with the highest resolving power, such as CRIFRES which extends up to 0.95 μm (10530 cm⁻¹). This will require careful selection of experimental conditions as evidenced by issues with pressure broadening in the high wavenumber region.

REFERENCES

- Adriani, A., A. Coradini, G. Filacchione, J. I. Lunine, A. Bini, C. Pasqui, L. Calamai, F. Colosimo, B. M. Dinelli, D. Grassi, G. Magni, M. L. Moriconi, and R. Orosei, JIRAM, the image spectrometer in the near infrared on board the Juno mission to Jupiter, *Astrobiol.*, 8: 613-22, 2008.
- Al Derzi, A.R., T. Furtenbacher, J. Tennyson, S.N. Yurchenko, and Attila G. Császár, MARVEL analysis of the measured high-resolution spectra of $^{14}\text{NH}_3$, *J. Quant. Spectrosc. Radiat. Trans.*, 161: 117-30, 2015.
- Assonov, S. S., C. A. M. Brenninkmeijer, T. J. Schuck, and P. Taylor, Analysis of ^{13}C and ^{18}O isotope data of CO_2 in CARIBIC aircraft samples as tracers of upper troposphere/lower stratosphere mixing and the global carbon cycle, *Atmos. Chem. Phys.*, 10: 8575-99, 2010.
- Barman, T.S., On the Presence of Water and Global Circulation in the Transiting Planet HD 189733b, *Astrophys. J. Lett.*, 676: L61, 2008.
- Barton, E. J., S. N. Yurchenko, J. Tennyson, S. Clausen, and A. Fateev, High-resolution absorption measurements of NH_3 at high temperatures: 2100-5500 cm^{-1} , *J. Quant. Radiat. Trans.*, 189: 60-65, 2016.
- Barton, E. J., S. N. Yurchenko, J. Tennyson, S. Clausen, and A. Fateev, High-resolution absorption measurements of NH_3 at high temperatures: 500–2100 cm^{-1} , *J. Quant. Radiat. Trans.*, 167: 126-34, 2015.
- Batalha, N. M., F. Rowe, S. T. Bryson, T. Barclay, C. J. Burke, D. A. Caldwell, J. L. Christiansen, F. Mullally, S. E. Thompson, T. M. Brown, A. K. Dupree, D. C. Fabrycky, E. B. Ford, J. J. Fortney, R. L. Gilliland, H. Isaacson, D. W. Latham, G. W. Marcy, S. N. Quinn, D. Ragozzine, A. Shporer, W. J. Borucki, D. R. Ciardi, III T. N. Gautier, M. R. Haas, J. M. Jenkins, D. G. Koch, J. J. Lissauer, W. Rapin, G. S. Basri, A. P. Boss, L. A. Buchhave, J. A. Carter, D. Charbonneau, J. Christensen-Dalsgaard, B. D. Clarke, W. D. Cochran, B.-O. Demory, J.-M. Desert, E. Devore, L. R. Doyle, G. A. Esquerdo, M. Everett, F. Fressin, J. C. Geary, F. R. Girouard, A. Gould, J. R. Hall, M. J. Holman, A.W. Howard, S. B. Howell, K. A. Ibrahim, K. Kinemuchi, H. Kjeldsen, T. C. Klaus, J. Li, P. W. Lucas, S. Meibom, R. L. Morris, A. Prša, E. Quintana, D. T. Sanderfer, D. Sasselov,

- S. E. Seader, J. C. Smith, J. H. Steffen, M. Still, M. C. Stumpe, J. C. Tarter, P. Tenenbaum, G. Torres, J. D. Twicken, K. Uddin, J. Van Cleve, L. Walkowicz, and W. F. Welsh, Planetary Candidates Observed by Kepler. III. Analysis of the First 16 Months of Data, *Astrophys. J. Supp. Series*, 204: 24, 2013.
- Beale, C. A., E. M. Buzan, C. D. Boone, and P. F. Bernath, Near-global distribution of CO isotopic fractionation in the Earth's atmosphere, *J. Mol. Spectrosc.*, 323: 59-66, 2016a.
- Beale, C.A., R.J. Hargreaves, and P.F. Bernath, Temperature-dependent high resolution absorption cross sections of propane, *J. Quant. Radiat. Trans.*, 182: 219-24, 2016b.
- Beale, C.A., R.J. Hargreaves, P. Coles, J. Tennyson, and P.F. Bernath. Infrared absorption spectra of hot ammonia, *J. Quant. Radiat. Trans.*, in press.
- Beer, R., M. W. Shephard, S. S. Kulawik, S. A. Clough, A. Eldering, K. W. Bowman, S. P. Sander, B. M. Fisher, V. H. Payne, M. Luo, G. B. Osterman, and J. R. Worden, First satellite observations of lower tropospheric ammonia and methanol, *Geophys. Res. Lett.*, 35: L09801, 2008.
- Bergamaschi, P., R. Hein, C. A. M. Brenninkmeijer, and P. J. Crutzen, Inverse modeling of the global CO cycle: 2. Inversion of $^{13}\text{C}/^{12}\text{C}$ and $^{18}\text{O}/^{16}\text{O}$ isotope ratios, *J. Geophys. Res.: Atmospheres*, 105: 1929-45, 2000.
- Bernath, P. F., C. T. McElroy, M. C. Abrams, C. D. Boone, M. Butler, C. Camy-Peyret, M. Carleer, C. Clerbaux, P. F. Coheur, R. Colin, P. DeCola, M. DeMazière, J. R. Drummond, D. Dufour, W. F. J. Evans, H. Fast, D. Fussen, K. Gilbert, D. E. Jennings, E. J. Llewellyn, R. P. Lowe, E. Mahieu, J. C. McConnell, M. McHugh, S. D. McLeod, R. Michaud, C. Midwinter, R. Nassar, F. Nichitiu, C. Nowlan, C. P. Rinsland, Y. J. Rochon, N. Rowlands, K. Semeniuk, P. Simon, R. Skelton, J. J. Sloan, M. A. Soucy, K. Strong, P. Tremblay, D. Turnbull, K. A. Walker, I. Walkty, D. A. Wardle, V. Wehrle, R. Zander, and J. Zou, Atmospheric Chemistry Experiment (ACE): Mission overview, *Geophys. Res. Lett.*, 32: L15S01, 2005.
- Bernath, P.F., *Spectra of Atoms and Molecules* (Oxford University Press: New York), 2005.
- Bernath, P. F., Molecular opacities for exoplanets, *Philosophical Transactions of the Royal Society A: Mathematical, Physical and Engineering Sciences*, 372: 20130087, 2014.
- Betts, R.A., C.D. Jones, J.R. Knight, R.F. Keeling, and J.J. Kennedy, El Nino and a record CO₂ rise, *Nature Climate Change*, 6: 806-10, 2016.

- Bird, M. K., P. Janardhan, T. L. Wilson, W. K. Huchtmeier, P. Gensheimer, and C. Lemme, K-band Radio Observations of Comet Hale-Bopp: Detections of Ammonia and (Possibly) Water, *Earth, Moon, and Planets*, 78: 21-28, 1997.
- Biver, N., J. Crovisier, D. Bockelée-Morvan, S. Szutowicz, D. C. Lis, P. Hartogh, M. de Val-Borro, R. Moreno, J. Boissier, M. Kidger, M. Küppers, G. Paubert, N. Dello Russo, R. Vervack, H. Weaver, and HsO team, Ammonia and other parent molecules in comet 10P/Tempel 2 from Herschel/HIFI and ground-based radio observations, *Astronomy & Astrophysics*, 539: A68, 2012.
- Boone, C. D., K. A. Walker, and P. F. Bernath, Version 3 Retrievals for the Atmospheric Chemistry Experiment Fourier Transform Spectrometer (ACE-FTS). in P. F. Bernath (ed.), *The Atmospheric Chemistry Experiment ACE at 10: A Solar Occultation Anthology* (A. Deepak Publishing: Hampton, Virginia, USA), 2013.
- Breeze, J. C., C. C. Ferriso, C. B. Ludwig, and W. Malkmus, Temperature Dependence of the Total Integrated Intensity of Vibrational—Rotational Band Systems, *J. Chem. Phys.*, 42: 402-06, 1965.
- Brenninkmeijer, C. A. M., T. Röckmann, M. Bräunlich, P. Jöckel, and P. Bergamaschi, Review of progress in isotope studies of atmospheric carbon monoxide, *Chemosphere - Global Change Science*, 1: 33-52, 1999.
- Brown, L. R., and J. S. Margolis, Empirical line parameters of NH₃ from 4791 to 5294 cm⁻¹, *J. Quant. Radiat. Trans.*, 56: 283-94, 1996.
- Brown, T.M., D.W. Latham, M.E. Everett and G.A. Esquerado, Kepler Input Catalog: Photometric Calibration and Stellar Classification, *Astron. J.*, 142: 112-140, 2011.
- Bruker, *Bruker IFS 125HR User Manual* (Bruker Optik GmbH: Ettlingen, Germany), 2006.
- Burgasser, A.J., T. R. Geballe, S. K. Leggett, J. D. Kirkpatrick, and D. A. Golimowski, A Unified Near-Infrared Spectral Classification Scheme for T Dwarfs, *Astrophys. J.*, 637: 1067, 2006.
- Burrows, A., W. B. Hubbard, J. I. Lunine, and J. Liebert, The theory of brown dwarfs and extrasolar giant planets, *Reviews of Modern Physics*, 73: 719-65, 2001.
- Burrows, A., R. S. Ram, P. Bernath, C. M. Sharp, and J. A. Milsom, New CrH Opacities for the Study of L and Brown Dwarf Atmospheres, *Astrophys. J.*, 577: 986.

- Burrows, A.S. 2014. Spectra as windows into exoplanet atmospheres, *Proceedings of the National Academy of Sciences*, 111: 12601-09, 2002.
- Buzan, E.M., R.J. Hargreaves, and P.F. Bernath, High resolution absorption cross sections for propylene in the 3 μm region at high temperatures, *Molecular Astrophysics*, 3–4: 16-20, 2016.
- Carleer, M.R., "WSpectra: a Windows program to accurately measure the line intensities of high-resolution Fourier transform spectra." In Proceedings of the SPIE 4168: 337-42, 2001.
- Carlson, R., W. Smythe, K. Baines, E. Barbini, K. Becker, R. Burns, S. Calcutt, W. Calvin, R. Clark, G. Danielson, A. Davies, P. Drossart, T. Encrenaz, F. Fanale, J. Granahan, G. Hansen, P. Herrera, C. Hibbitts, J. Hui, P. Irwin, T. Johnson, L. Kamp, H. Kieffer, F. Leader, E. Lellouch, R. Lopes-Gautier, D. Matson, T. McCord, R. Mehlman, A. Ocampo, G. Orton, M. Roos-Serote, M. Segura, J. Shirley, L. Soderblom, A. Stevenson, F. Taylor, J. Torson, A. Weir, and P. Weissman, Near-Infrared Spectroscopy and Spectral Mapping of Jupiter and the Galilean Satellites: Results from Galileos Initial Orbit, *Science*, 274: 385-88, 1996.
- Charbonneau, D., T.M. Brown, D.W. Latham, and M. Mayor, Detection of Planetary Transits Across a Sun-like Star, *Astrophys. J. Letters*, 529: L45, 2000.
- David, Charbonneau, M. Brown Timothy, W. Noyes Robert, and L. Gilliland Ronald, Detection of an Extrasolar Planet Atmosphere, *Astrophys. J.*, 568: 377, 2002.
- Charlson, R. J., S. E. Schwartz, J. M. Hales, R. D. Cess, J. A. Coakley, J. E. Hansen, and D. J. Hofmann, Climate Forcing by Anthropogenic Aerosols, *Science*, 255: 423, 1992.
- Chen, D.-W., K. N. Rao, and R.S. McDowell, Fundamental and overtone bands of isotopic species of carbon monoxide, *J. Mol. Spectrosc.*, 61: 71-78, 1976.
- Cheung, A. C., D. M. Rank, C. H. Townes, D. D. Thornton, and W. J. Welch, Detection of NH_3 Molecules in the Interstellar Medium by Their Microwave Emission, *Physical Review Letters*, 21: 1701-05, 1968.
- Chrystie, R.S. M., E.F. Nasir, and A. Farooq, Propene concentration sensing for combustion gases using quantum-cascade laser absorption near 11 μm , *Applied Physics B*, 120: 317-27, 2015.

- Clerbaux, C., P. F. Coheur, D. Hurtmans, B. Barret, M. Carleer, R. Colin, K. Semeniuk, J. C. McConnell, C. Boone, and P. Bernath, Carbon monoxide distribution from the ACE-FTS solar occultation measurements, *Geophys. Res. Lett.*, 32: L16S01, 2005.
- Clerbaux, C., M. George, S. Turquety, K. A. Walker, B. Barret, P. Bernath, C. Boone, T. Borsdorff, J. P. Cammas, V. Catoire, M. Coffey, P. F. Coheur, M. Deeter, M. De Mazière, J. Drummond, P. Duchatelet, E. Dupuy, R. de Zafra, F. Eddounia, D. P. Edwards, L. Emmons, B. Funke, J. Gille, D. W. T. Griffith, J. Hannigan, F. Hase, M. Höpfner, N. Jones, A. Kagawa, Y. Kasai, I. Kramer, E. Le Flochmoën, N. J. Livesey, M. López-Puertas, M. Luo, E. Mahieu, D. Murtagh, P. Nédélec, A. Pazmino, H. Pumphrey, P. Ricaud, C. P. Rinsland, C. Robert, M. Schneider, C. Senten, G. Stiller, A. Strandberg, K. Strong, R. Sussmann, V. Thouret, J. Urban, and A. Wiacek, CO measurements from the ACE-FTS satellite instrument: data analysis and validation using ground-based, airborne and spaceborne observations, *Atmos. Chem. Phys.*, 8: 2569-94, 2008.
- Conrad, R., and W. Seiler, Influence of the surface microlayer on the flux of nonconservative trace gases (CO, H₂, CH₄, N₂O) across the ocean-atmosphere interface, *J. Atmos. Chem.*, 6: 83-94, 1988.
- Coustenis, A., R.K. Achterberg, B.J. Conrath, D.E. Jennings, A. Marten, D. Gautier, C.A. Nixon, F.M. Flasar, N.A. Teanby, B. Bézard, R.E. Samuelson, R.C. Carlson, E. Lellouch, G.L. Bjoraker, P.N. Romani, F.W. Taylor, P. G. J. Irwin, T. Fouchet, A. Hubert, G.S. Orton, V.G. Kunde, S. Vinatier, J. Mondellini, M.M. Abbas, and R. Courtin, The composition of Titans stratosphere from Cassini/CIRS mid-infrared spectra, *Icarus*, 189: 35-62, 2007.
- Crawford, B., Vibrational Intensities. X. Integration Theorems, *J. Chem. Phys.*, 29: 1042-45, 1958.
- Cushing, M.C., J. D. Kirkpatrick, C.R. Gelino, R.L. Griffith, M.F. Skrutskie, A. Mainzer, K.A. Marsh, C.A. Beichman, A.J. Burgasser, L.A. Prato, R.A. Simcoe, M.S. Marley, D. Saumon, R.S. Freedman, P.R. Eisenhardt, and E.L. Wright, The Discovery of Y Dwarfs using Data from the Wide-field Infrared Survey Explorer (WISE), *Astrophys. J.*, 743: 50, 2011.
- Cushing, M.C., T.L. Roellig, M.S. Marley, D. Saumon, S. K. Leggett, J. D. Kirkpatrick, J.C. Wilson, G. C. Sloan, A.K. Mainzer, J.E. Van Cleve, and J.R. Houck, A Spitzer Infrared Spectrograph Spectral Sequence of M, L, and T Dwarfs, *Astrophys. J.*, 648: 614, 2006.

- de Laat, A. T. J., A. M. S. Gloudemans, H. Schrijver, M. M. P. van den Broek, J. F. Meirink, I. Aben, and M. Krol, Quantitative analysis of SCIAMACHY carbon monoxide total column measurements, *Geophys. Res. Lett.*, 33: L07807, 2006.
- Deeter, M. N., L. K. Emmons, G. L. Francis, D. P. Edwards, J. C. Gille, J. X. Warner, B. Khattatov, D. Ziskin, J. F. Lamarque, S. P. Ho, V. Yudin, J. L. Attié, D. Packman, J. Chen, D. Mao, and James R. Drummond, Operational carbon monoxide retrieval algorithm and selected results for the MOPITT instrument, *J. Geophys. Res.: Atmos.*, 108: 4399, 2003.
- Doskey, P. V., and J. S. Gaffney, Non-methane hydrocarbons in the Arctic atmosphere at Barrow, Alaska, *Geophys. Res. Lett.*, 19: 381-84, 1992.
- Down, M. J., C. Hill, S. N. Yurchenko, J. Tennyson, L. R. Brown, and I. Kleiner. 2013. Re-analysis of ammonia spectra: Updating the HITRAN $^{14}\text{NH}_3$ database, *J. Quant. Radiat. Trans.*, 130: 260-72.
- Dudhia, A. The Reference Forward Model (RFM), *J. Quant. Radiat. Trans.*, 186: 243-53, in press.
- Ebi, K. L., and G. McGregor, Climate change, tropospheric ozone and particulate matter, and health impacts, *Environ. Health Persp.*, 116: 1449-55, 2008.
- Ehhalt, D.H., Gas phase chemistry of the troposphere, *Glob. Asp. Atmos. Chem.*, 6: 21-110, 1999.
- Eiji, T., K. Nobuyuki, S. Masahiro, N. Atsushi, and W. Dibble Robert, In situ measurement of hydrocarbon fuel concentration near a spark plug in an engine cylinder using the 3.392 μm infrared laser absorption method: discussion of applicability with a homogeneous methane-air mixture, *Meas. Sci. Tech.*, 14: 1350, 2003.
- Es-sebbar, E., M. Alrefae, and A. Farooq, Infrared cross-sections and integrated band intensities of propylene: Temperature-dependent studies, *J. Quant. Radiat. Trans.*, 133: 559-69, 2014.
- Etheridge, D. M., L. P. Steele, R. L. Langenfelds, R. J. Francey, J. M. Barnola, and V. I. Morgan, Natural and anthropogenic changes in atmospheric CO_2 over the last 1000 years from air in Antarctic ice and firn, *J. Geophys. Res.: Atmos.*, 101: 4115-28, 1996.
- Falkowski, Paul G., and Matthew J. Oliver, Mix and match: how climate selects phytoplankton, *Nat. Rev. Microbio.*, 5: 813-19, 2007.

- Feilberg, K. L., B. D'Anna, M. S. Johnson, and C. J. Nielsen, Relative Tropospheric Photolysis Rates of HCHO, H¹³CHO, HCH¹⁸O, and DCDO Measured at the European Photoreactor Facility, *J. Phys. Chem. A*, 109: 8314-19, 2005.
- Feilberg, K. L., M. S. Johnson, and C.J. Nielsen, Relative Reaction Rates of HCHO, HCDO, DCDO, H¹³CHO, and HCH¹⁸O with OH, Cl, Br, and NO₃ Radicals, *J. Phys. Chem. A*, 108: 7393-98, 2004.
- Finlayson-Pitts, B. J., and J. N. Pitts, Tropospheric Air Pollution: Ozone, Airborne Toxics, Polycyclic Aromatic Hydrocarbons, and Particles, *Science*, 276: 1045-51, 1997.
- Flaud, J. M., W. J. Lafferty, and M. Herman, First high resolution analysis of the absorption spectrum of propane in the 6.7 μm to 7.5 μm spectral region, *J. Chem. Phys.*, 114: 9361-66, 2001.
- Fletcher, L. N., B. Swinyard, C. Salji, E. Polehampton, T. Fulton, S. Sidher, E. Lellouch, R. Moreno, G. Orton, T. Cavalié, R. Courtin, M. Rengel, H. Sagawa, G. R. Davis, P. Hartogh, D. Naylor, H. Walker, and T. Lim, Sub-millimetre spectroscopy of Saturn's trace gases from Herschel/SPIRE, *Astron. & Astrophys.*, 539: A44, 2012.
- Freedman, R., and W. Kauffmann, *Universe* (W. H. Freeman: New York), 2007.
- Funke, B., M. López-Puertas, M. García-Comas, G. P. Stiller, T. von Clarmann, M. Höpfner, N. Glatthor, U. Grabowski, S. Kellmann, and A. Linden, Carbon monoxide distributions from the upper troposphere to the mesosphere inferred from 4.7 μm non-local thermal equilibrium emissions measured by MIPAS on Envisat, *Atmos. Chem. Phys.*, 9: 2387-411, 2009.
- George, M., C. Clerbaux, D. Hurtmans, S. Turquety, P. F. Coheur, M. Pommier, J. Hadji-Lazaro, D. P. Edwards, H. Worden, M. Luo, C. Rinsland, and W. McMillan, Carbon monoxide distributions from the IASI/METOP mission: evaluation with other space-borne remote sensors, *Atmos. Chem. Phys.*, 9: 8317-30, 2009.
- Gola, A. A., B. D'Anna, K. L. Feilberg, S. R. Sellevåg, L. Bache-Andreassen, and C. J. Nielsen, Kinetic isotope effects in the gas phase reactions of OH and Cl with CH₃Cl, CD₃Cl, and ¹³CH₃Cl, *Atmos. Chem. Phys.*, 5: 2395-402, 2005.
- Gray, R. O. and C. J. Corbally. The calibration of MK spectral classes using spectral synthesis. I. The effective temperature calibration of dwarf stars, *Astron. J.*, 107: 2, 1994.

- Greathouse, T. K., J. H. Lacy, B. Bézard, J. I. Moses, M. J. Richter, and C. Knez, The first detection of propane on Saturn, *Icarus*, 181: 266-71, 2006.
- Grillmair, C. J., A. Burrows, D. Charbonneau, L. Armus, J. Stauffer, V. Meadows, J. van Cleve, K. von Braun, and D. Levine, Strong water absorption in the dayside emission spectrum of the planet HD 189733b, *Nature*, 456: 767-69, 2008.
- Gromov, S., and C. A. M. Brenninkmeijer, An estimation of the $^{18}\text{O}/^{16}\text{O}$ ratio of UT/LMS ozone based on artefact CO in air sampled during CARIBIC flights, *Atmos. Chem. Phys.*, 15: 1901-12, 2015.
- Gros, V., M. Bräunlich, T. Röckmann, P. Jöckel, P. Bergamaschi, C. A. M. Brenninkmeijer, W. Rom, W. Kutschera, A. Kaiser, H. E. Scheel, M. Mandl, J. van der Plicht, and G. Possnert, Detailed analysis of the isotopic composition of CO and characterization of the air masses arriving at Mount Sonnblick (Austrian Alps), *J. Geophys. Res.: Atmospheres*, 106: 3179-93, 2001.
- Gros, V. P. Jöckel, C. A. M. Brenninkmeijer, T. Röckmann, F. Meinhardt, and R. Graul, Characterization of pollution events observed at Schauinsland, Germany, using CO and its stable isotopes, *Atmos. Environ.*, 36: 2831-40, 2002.
- Grosch, A., V. Beushausen, H. Wackerbarth, O. Thiele, T. Berg, and R. Grzeszik, Calibration of mid-infrared transmission measurements for hydrocarbon detection and propane concentration measurements in harsh environments by using a fiber optical sensor, *J. Quant. Radiat. Trans.*, 112: 994-1004, 2011.
- Grosch, A., V. Beushausen, H. Wackerbarth, O. Thiele, and T. Berg, Temperature- and pressure-dependent midinfrared absorption cross sections of gaseous hydrocarbons, *App. Opt.*, 49: 196-203, 2010.
- Haigh, J. D., Climate change 1992. The supplementary report to the IPCC scientific assessment, J. T. Houghton, B. A. Callander and S. K. Varney (eds), Published for the Intergovernmental Panel on Climate Change by Cambridge University Press, (Cambridge), ISBN 0-521-43829-2, *Intern. J. Clim.*, 13: 813-14, 1993.
- Hanel, R., B. Conrath, F. M. Flasar, V. Kunde, W. Maguire, J. Pearl, J. Pirraglia, R. Samuelson, L. Herath, M. Allison, D. Cruikshank, D. Gautier, P. Gierasch, L. Horn, R. Koppany, and C. Ponnampereuma, Infrared Observations of the Saturnian System from Voyager 1, *Science*, 212: 192-200, 1981.

- Hansen, J. E., Sir John Houghton: Global Warming: The Complete Briefing, 2nd edition, *J. Atmos. Chem.*, 30: 409-12, 1998.
- Hargreaves, R. J., P. F. Bernath, J. Bailey, and M. Dulick, Empirical Line Lists and Absorption Cross Sections for Methane at High Temperatures, *Astrophys. J.*, 813: 12, 2015a.
- Hargreaves, R. J., E. Buzan, M. Dulick, and P. F. Bernath, High-resolution absorption cross sections of C₂H₆ at elevated temperatures, *Mol. Astrophys.*, 1: 20-25, 2015b.
- Hargreaves, R. J., K. H. Hinkle, C. W. Bauschlicher Jr, S. Wende, A. Seifahrt, and P.F. Bernath, High-resolution 1.6 μm Spectra of FeH in M and L Dwarfs, *Astron. J.*, 140: 919, 2010.
- Hargreaves, R. J., G. Li, and P. F. Bernath, Hot NH₃ Spectra for Astrophysical Applications, *Astrophys. J.*, 735: 111, 2011.
- Hargreaves, R. J., G. Li, and P. F. Bernath, Ammonia line lists from 1650 to 4000 cm⁻¹, *J. Quant. Radiat. Trans.*, 113: 670-79, 2012.
- Harrison, J. J., and P. F. Bernath, Infrared absorption cross sections for propane (C₃H₈) in the 3 μm region, *J. Quant. Radiat. Trans.*, 111: 1282-88, 2010.
- Ho, P. T. P., and C.H. Townes, Interstellar Ammonia, *Ann. Rev.Astron. Astrophys.*, 21: 239-70, 1983.
- Höpfner, M., R. Volkamer, U. Grabowski, M. Grutter, J. Orphal, G. Stiller, T. von Clarmann, and G. Wetzel, First detection of ammonia (NH₃) in the Asian summer monsoon upper troposphere, *Atmos. Chem. Phys.*, 16: 14357-69, 2016.
- Huang, X., D. W. Schwenke, and T. J. Lee, Rovibrational spectra of ammonia. I. Unprecedented accuracy of a potential energy surface used with nonadiabatic corrections, *J. Chem. Phys.*, 134: 044320, 2011a.
- Huang, X., D. W. Schwenke, and T. J. Lee, Rovibrational spectra of ammonia. II. Detailed analysis, comparison, and prediction of spectroscopic assignments for ¹⁴NH₃, ¹⁵NH₃, and ¹⁴ND₃, *J. Chem. Phys.*, 134: 044321, 2011b.
- Hughes, T. P., A. H. Baird, D. R. Bellwood, M. Card, S. R. Connolly, C. Folke, R. Grosberg, O. Hoegh-Guldberg, J. B. C. Jackson, J. Kleypas, J. M. Lough, P. Marshall, M. Nyström, S. R. Palumbi, J. M. Pandolfi, B. Rosen, and J. Roughgarden, Climate Change, Human Impacts, and the Resilience of Coral Reefs, *Science*, 301: 929-33, 2003.

- Ida, S., and D. N. C. Lin.,. Toward a Deterministic Model of Planetary Formation. III. Mass Distribution of Short-Period Planets around Stars of Various Masses, *Astrophys. J.*, 626: 1045, 2005
- Jacob, D., *Introduction to Atmospheric Chemistry* (Princeton University Press), 1999.
- Jacquinet-Husson, N., R. Armante, N. A. Scott, A. Chédin, L. Crépeau, C. Boutammine, A. Bouhdaoui, C. Crevoisier, V. Capelle, C. Boone, N. Poulet-Crovisier, A. Barbe, D. Chris Benner, V. Boudon, L. R. Brown, J. Buldyreva, A. Campargue, L. H. Coudert, V. M. Devi, M. J. Down, B. J. Drouin, A. Fayt, C. Fittschen, J. M. Flaud, R. R. Gamache, J. J. Harrison, C. Hill, Ø Hodnebrog, S. M. Hu, D. Jacquemart, A. Jolly, E. Jiménez, N. N. Lavrentieva, A. W. Liu, L. Lodi, O. M. Lyulin, S. T. Massie, S. Mikhailenko, H. S. P. Müller, O. V. Naumenko, A. Nikitin, C. J. Nielsen, J. Orphal, V. I. Perevalov, A. Perrin, E. Polovtseva, A. Predoi-Cross, M. Rotger, A. A. Ruth, S. S. Yu, K. Sung, S. A. Tashkun, J. Tennyson, V. I. Tyuterev, J. Vander Auwera, B. A. Voronin, and A. Makie, The 2015 edition of the GEISA spectroscopic database, *J. Mol. Spectrosc.*, 327: 31-72, 2016.
- Jaschek, C., and M. Jaschek.,. *The Classification of Stars* (Cambridge University Press: Cambridge), 1990.
- Jones, A., K. A. Walker, J. J. Jin, J. R. Taylor, C. D. Boone, P. F. Bernath, S. Brohede, G. L. Manney, S. McLeod, R. Hughes, and W. H. Daffer, Technical Note: A trace gas climatology derived from the Atmospheric Chemistry Experiment Fourier Transform Spectrometer (ACE-FTS) data set, *Atmos. Chem. Phys.*, 12: 5207-20, 2012.
- Kabin, K., T. I. Gombosi, D. L. DeZeeuw, and K. G. Powell, Interaction of Mercury with the Solar Wind, *Icarus*, 143: 397-406, 2000.
- Kato, S., Y. Kajii, H. Akimoto, M. Bräunlich, T. Röckmann, and C.A.M. Brenninkmeijer, Observed and modeled seasonal variation of ^{13}C , ^{18}O , and ^{14}C of atmospheric CO at Happo, a remote site in Japan, and a comparison with other records, *J. Geophys. Res.: Atmos.*, 105: 8891-900, 2000.
- Khalil, M. A. K., and R. A. Rasmussen, The global cycle of carbon monoxide: Trends and mass balance, *Chemosphere*, 20: 227-42, 1990.

- Kim, Sang J., and J. Caldwell, The abundance of CH₃D in the atmosphere of Titan, derived from 8- to 14- μ m thermal emission, *Icarus*, 52: 473-82, 1982.
- Kim, Sang J., T. R. Geballe, H. J. Seo, and J. H. Kim, Jupiters hydrocarbon polar brightening: Discovery of 3-micron line emission from south polar CH₄, C₂H₂, and C₂H₆, *Icarus*, 202: 354-57, 2009.
- Kirkpatrick, J. D., I. N. Reid, J. Liebert, R. M. Cutri, B. Nelson, C. A. Beichman, C. C. Dahn, D. G. Monet, J. E. Gizis, and M. F. Skrutskie, Dwarfs Cooler than "M": The Definition of Spectral Type "L" Using Discoveries from the 2-Micron All-Sky Survey (2MASS), *Astrophys. J.*, 519: 802, 1999.
- Kleiner, I., L. R. Brown, G. Tarrago, Q. L. Kou, N. Picqué, G. Guelachvili, V. Dana, and J. Y. Mandin, Positions and Intensities in the 2 $\nu_4/\nu_1/\nu_3$ Vibrational System of ¹⁴NH₃ Near 3 μ m, *J. Mol. Spectrosc.*, 193: 46-71, 1999.
- Klingbeil, A. E., J. B. Jeffries, and R. K. Hanson, Temperature-dependent mid-IR absorption spectra of gaseous hydrocarbons, *J. Quant. Radiat. Trans.*, 107: 407-20, 2007.
- Kolodner, M. A., and P. G. Steffes, The Microwave Absorption and Abundance of Sulfuric Acid Vapor in the Venus Atmosphere Based on New Laboratory Measurements, *Icarus*, 132: 151-69, 1998.
- Krankowsky, D., F. Bartecki, G. G. Klees, K. Mauersberger, K. Schellenbach, and J. Stehr, Measurement of Heavy Isotope Enrichment in Tropospheric Ozone, *Geophys. Res. Lett.*, 22: 1713-16, 1995.
- Kwabia Tchana, F., J. M. Flaud, W. J. Lafferty, L. Manceron, and P. Roy, The first high-resolution analysis of the low-lying ν_9 band of propane, *J. Quant. Radiat. Trans.*, 111: 1277-81, 2010.
- Lamarque, J. F., T. C. Bond, V. Eyring, C. Granier, A. Heil, Z. Klimont, D. Lee, C. Liousse, A. Mieville, B. Owen, M. G. Schultz, D. Shindell, S. J. Smith, E. Stehfest, J. Van Aardenne, O. R. Cooper, M. Kainuma, N. Mahowald, J. R. McConnell, V. Naik, K. Riahi, and D. P. van Vuuren, Historical (1850–2000) gridded anthropogenic and biomass burning emissions of reactive gases and aerosols: methodology and application, *Atmos. Chem. Phys.*, 10: 7017-39, 2010.

- Lämmerzahl, P., T. Röckmann, C.A.M. Brenninkmeijer, D. Krankowsky, and K. Mauersberger, Oxygen isotope composition of stratospheric carbon dioxide, *Geophys. Res. Lett.*, 29: 23-1-23-4, 2002.
- Lebonnois, S., F. Hourdin, V. Eymet, A. Crespin, R. Fournier, and F. Forget, Superrotation of Venus atmosphere analyzed with a full general circulation model, *J. Geophys. Res.: Planets*, 115: E06006, 2010.
- Leggett, S. K., P. Tremblin, D. Saumon, M. S. Marley, V. Morley Caroline, D. S. Amundsen, I. Baraffe, and G. Chabrier, Near-infrared Spectroscopy of the Y0 WISEP J173835.52+273258.9 and the Y1 WISE J035000.32-565830.2: The Importance of Non-equilibrium Chemistry, *Astrophys. J.*, 824: 2, 2016.
- Lide, D. R., Microwave Spectrum, Structure, and Dipole Moment of Propane, *J. Chem. Phys.*, 33: 1514-18, 1960.
- Lieven, C., C. Clerbaux, F. Dentener, D. Hurtmans, and P.-F. Coheur, Global ammonia distribution derived from infrared satellite observations, *Nat. Geo.*, 2: 479-83, 2009.
- Line, M. R., J. Teske, B. Burningham, J. J. Fortney, and M. S. Marley, Uniform Atmospheric Retrieval Analysis of Ultracool Dwarfs. I. Characterizing Benchmarks, Gl 570D and HD 3651B, *Astrophys. J.*, 807: 183, 2015.
- Line, M. R., G. Vasisht, P. Chen, D. Angerhausen, and Y.L. Yung, Thermochemical and Photochemical Kinetics in Cooler Hydrogen-dominated Extrasolar Planets: A Methane-poor GJ436b?, *Astrophys. J.*, 738: 32, 2011.
- Lodders, K., and B. Fegley Jr., Atmospheric Chemistry in Giant Planets, Brown Dwarfs, and Low-Mass Dwarf Stars: I. Carbon, Nitrogen, and Oxygen, *Icarus*, 155: 393-424, 2002.
- Maguire, W. C., R. A. Hanel, D. E. Jennings, V. G. Kunde, and R. E. Samuelson, C₃H₈ and C₃H₄ in Titans atmosphere, *Nature*, 292: 683-86, 1981.
- Mak, J. E., and C. A. M. Brenninkmeijer, Measurement of ¹³CO and C¹⁸O in the free troposphere, *J. Geophys. Res.: Atmos.*, 103: 19347-58, 1998.
- Mak, J. E., G. Kra, T. Sandomenico, and P. Bergamaschi, The seasonally varying isotopic composition of the sources of carbon monoxide at Barbados, West Indies, *J. Geophys. Res.: Atmos.*, 108: 4635, 2003.

- Manning, M. R., C. A. M. Brenninkmeijer, and W. Allan, Atmospheric carbon monoxide budget of the southern hemisphere: Implications of $^{13}\text{C}/^{12}\text{C}$ measurements, *J. Geophys. Res.: Atmos.*, 102: 10673-82, 1997.
- Marley, M. S., and S. K. Leggett, The Future of Ultracool Dwarf Science with JWST. in Harley A. Thronson, Massimo Stiavelli and Alexander Tielens (eds.), *Astrophysics in the Next Decade: The James Webb Space Telescope and Concurrent Facilities* (Springer Netherlands: Dordrecht), 2009.
- Marsh, D. R., M. J. Mills, D. E. Kinnison, J. F. Lamarque, N. Calvo, and L. M. Polvani, Climate Change from 1850 to 2005 Simulated in CESM1(WACCM), *J. Clim.*, 26: 7372-91, 2013.
- Matousek, S., The Juno New Frontiers mission, *Acta Astronautica*, 61: 932-39, 2007.
- Mayor, M., and D. Queloz, A Jupiter-mass companion to a solar-type star, *Nature*, 378: 355-59, 1995.
- McGovern, M. R., K. J. Davy, I. S. McLean, A. J. Burgasser, L. Prato, and P.J. Lowrance, Identifying Young Brown Dwarfs Using Gravity-Sensitive Spectral Features, *Astrophys. J.*, 600: 1020. Mina-Camilde, N., C. Manzanares I, and J.F. Caballero. 1996. Molecular Constants of Carbon Monoxide at $v = 0, 1, 2,$ and 3 : A Vibrational Spectroscopy Experiment in Physical Chemistry, *J. Chem. Educ.*, 73: 804, 2004.
- Nelson, R. M., L. W. Kamp, D. L. Matson, P. G. J. Irwin, K. H. Baines, M. D. Boryta, F. E. Leader, R. Jaumann, W. D. Smythe, C. Sotin, R. N. Clark, D. P. Cruikshank, P. Drossart, J. C. Pearl, B. W. Hapke, J. Lunine, M. Combes, G. Bellucci, J. P. Bibring, F. Capaccioni, P. Cerroni, A. Coradini, V. Formisano, G. Filacchione, R. Y. Langevin, T. B. McCord, V. Mennella, P. D. Nicholson, and B. Sicardy, Saturn's Titan: Surface change, ammonia, and implications for atmospheric and tectonic activity, *Icarus*, 199: 429-41, 2009.
- Niemann, H. B., S. K. Atreya, G. R. Carignan, T. M. Donahue, J. A. Haberman, D. N. Harpold, R. E. Hartle, D. M. Hunten, W. T. Kasprzak, P. R. Mahaffy, T. C. Owen, and N. W. Spencer, Chemical composition measurements of the atmosphere of Jupiter with the Galileo Probe mass spectrometer, *Adv. Space Res.*, 21: 1455-61, 1998.
- Nier, A. O., and M. B. McElroy, Composition and structure of Mars Upper atmosphere: Results from the neutral mass spectrometers on Viking 1 and 2, *J. Geophys. Res.*, 82: 4341-49, 1977.

- Nixon, C. A., D. E. Jennings, B. Bézard, S. Vinatier, N. A. Teanby, K. Sung, T. M. Ansty, P. G. J. Irwin, N. Gorius, V. Cottini, A. Coustenis, and F. M. Flasar, Detection of Propene in Titans Stratosphere, *Astrophys. J. Letters*, 776: L14, 2013.
- Nixon, C. A., N. A. Teanby, S. B. Calcutt, S. Aslam, D. E. Jennings, V. G. Kunde, F. M. Flasar, P. G. Irwin, F. W. Taylor, D. A. Glenar, and M. D. Smith, Infrared limb sounding of Titan with the Cassini Composite InfraRed Spectrometer: effects of the mid-IR detector spatial responses, *App. Opt.*, 48: 1912-25, 2009.
- Novelli, P., and K. Masarie, Atmospheric Carbon Monoxide Dry Air Mole Fractions from the NOAA ESRL Carbon Cycle Cooperative Global Air Sampling Network, 1988-2013, ftp://aftp.cmdl.noaa.gov/data/trace_gases/co/flask/surface/README_surface_flask_co.html. Accessed July 8 2016, 2014.
- Oppenheimer, B. R., S. R. Kulkarni, K. Matthews, and T. Nakajima, Infrared Spectrum of the Cool Brown Dwarf Gl 229B, *Science*, 270: 1478-79, 1995.
- Parrish, D. D, Carbon Monoxide and Light Alkanes as Tropospheric Tracers of Anthropogenic Ozone. in H. Niki and K. H. Becker (eds.), *The Tropospheric Chemistry of Ozone in the Polar Regions* (Springer Berlin Heidelberg), 1993.
- Perrin, A., F. Kwabia-Tchana, J. M. Flaud, L. Manceron, J. Demaison, N. Vogt, P. Groner, and W. J. Lafferty, First high resolution analysis of the ν_{21} band of propane $\text{CH}_3\text{CH}_2\text{CH}_3$ at 921.382 cm^{-1} : Evidence of large amplitude tunneling effects, *J. Mol. Spectrosc.*, 315: 55-62, 2015.
- Polyansky, O. L., R. I. Ovsyannikov, A. A. Kyuberis, L. Lodi, J. Tennyson, A. Yachmenev, S. N. Yurchenko, and N. F. Zobov, Calculation of rotation-vibration energy levels of the ammonia molecule based on an ab initio potential energy surface, *J. Mol. Spectrosc.*, 327: 21-30, 2016.
- Pommier, M., K. S. Law, C. Clerbaux, S. Turquety, D. Hurtmans, J. Hadji-Lazaro, P. F. Coheur, H. Schlager, G. Ancellet, J. D. Paris, P. Nédélec, G. S. Diskin, J. R. Podolske, J. S. Holloway, and P. Bernath, IASI carbon monoxide validation over the Arctic during POLARCAT spring and summer campaigns, *Atmos. Chem. Phys.*, 10: 10655-78, 2010.
- Rebolo, R., M. R. Zapatero Osorio, and E. L. Martin, Discovery of a brown dwarf in the Pleiades star cluster, *Nature*, 377: 129-31, 1995.

- Ricaud, P., D. Alexandre, B. Barret, E. Le Flochmoën, E. Motte, G. Berthet, F. Lefèvre, and D. Murtagh, Measurements of mid-stratospheric formaldehyde from the Odin/SMR instrument, *J. Quant. Radiat. Trans.*, 107: 91-104, 2007.
- Röckmann, T., M. Brass, R. Borchers, and A. Engel, The isotopic composition of methane in the stratosphere: high-altitude balloon sample measurements, *Atmos. Chem. Phys.*, 11: 13287-304, 2011.
- Röckmann, T., C. A. M. Brenninkmeijer, G. Saueressig, P. Bergamaschi, J. N. Crowley, H. Fischer, and P. J. Crutzen, Mass-Independent Oxygen Isotope Fractionation in Atmospheric CO as a Result of the Reaction CO + OH, *Science*, 281: 544-46, 1998.
- Röckmann, T., P. Jöckel, V. Gros, M. Bräunlich, G. Possnert, and C. A. M. Brenninkmeijer, Using ^{14}C , ^{13}C , ^{18}O and ^{17}O isotopic variations to provide insights into the high northern latitude surface CO inventory, *Atmos. Chem. Phys.*, 2: 147-59, 2002.
- Röckmann, T., and C. A. M. Brenninkmeijer, CO and CO₂ isotopic composition in Spitsbergen during the 1995 ARCTOC campaign, *Tellus B: Chem. Phys. Meteorol.*, 49: 455-65, 1997.
- Roe, H. G., T. K. Greathouse, M. J. Richter, and J. H. Lacy, Propane on Titan, *Astrophys. J. Letters*, 597: L65, 2003.
- Rothman, L. S., I. E. Gordon, Y. Babikov, A. Barbe, D. Chris Benner, P. F. Bernath, M. Birk, L. Bizzocchi, V. Boudon, L. R. Brown, A. Campargue, K. Chance, E. A. Cohen, L. H. Coudert, V. M. Devi, B. J. Drouin, A. Fayt, J. M. Flaud, R. R. Gamache, J. J. Harrison, J. M. Hartmann, C. Hill, J. T. Hodges, D. Jacquemart, A. Jolly, J. Lamouroux, R. J. Le Roy, G. Li, D. A. Long, O. M. Lyulin, C. J. Mackie, S. T. Massie, S. Mikhailenko, H. S. P. Müller, O. V. Naumenko, A. V. Nikitin, J. Orphal, V. Perevalov, A. Perrin, E. R. Polovtseva, C. Richard, M. A. H. Smith, E. Starikova, K. Sung, S. Tashkun, J. Tennyson, G. C. Toon, V. I. Tyuterev, and G. Wagner, The HITRAN2012 molecular spectroscopic database, *J. Quant. Radiat. Trans.*, 130: 4-50, 2013.
- Rothman, L. S., D. Jacquemart, A. Barbe, D. Chris Benner, M. Birk, L. R. Brown, M. R. Carleer, C. Chackerian Jr, K. Chance, L. H. Coudert, V. Dana, V. M. Devi, J. M. Flaud, R. R. Gamache, A. Goldman, J. M. Hartmann, K. W. Jucks, A. G. Maki, J. Y. Mandin, S. T. Massie, J. Orphal, A. Perrin, C. P. Rinsland, M. A. H. Smith, J. Tennyson, R. N. Tolchenov, R. A. Toth, J. Vander Auwera, P. Varanasi, and G. Wagner, The HITRAN 2004 molecular spectroscopic database, *J. Quant. Radiat. Trans.*, 96: 139-204, 2005.

- Sabine, C. L., R. A. Feely, N. Gruber, R. M. Key, K. Lee, J. L. Bullister, R. Wanninkhof, C. S. Wong, D. W. R. Wallace, B. Tilbrook, F. J. Millero, T. Peng, A. Kozyr, T. Ono, and A. F. Rios, The Oceanic Sink for Anthropogenic CO₂, *Science*, 305: 367-71, 2004.
- Sahlberg, A., J. Zhou, M. Aldén, and Z. Li, Investigation of ro-vibrational spectra of small hydrocarbons at elevated temperatures using infrared degenerate four-wave mixing, *J. Raman Spectrosc.*, 47: 1130-1139, 2016.
- Sander, S. P., J. Abbatt, J. R. Barker, J. B. Burkholder, R. R. Friedl, D. M. Golden, R. E. Huie, C. E. Kolb, M. J. Kurylo, G. K. Moortgat, V. L. Orkin, and P. H. Wine, Chemical Kinetics and Photochemical Data for Use in Atmospheric Studies, Evaluation No. 17. In *JPL Publication 10-6*. Jet Propulsion Laboratory, Pasadena, 2011.
- Schmidt, J. A., M. S. Johnson, and R. Schinke, Carbon dioxide photolysis from 150 to 210 nm: Singlet and triplet channel dynamics, UV-spectrum, and isotope effects, *PNAS*, 110: 17691-96, 2013.
- Sharpe, S. W., T. J. Johnson, R. L. Sams, P. M. Chu, G. C. Rhoderick, and P. A. Johnson, Gas-Phase Databases for Quantitative Infrared Spectroscopy, *App. Spectrosc.*, 58: 1452-61, 2004.
- Sheese, P. E., C. D. Boone, and K. A. Walker, Detecting physically unrealistic outliers in ACE-FTS atmospheric measurements, *Atmos. Meas. Tech.*, 8: 741-50, 2015.
- Shimanouchi, T., *Tables of Molecular Vibrational Frequencies Consolidated Volume I* (National Bureau of Standards), 1972.
- Snellen, I. A. G., R. J. de Kok, E. J. W. de Mooij, and S. Albrecht, The orbital motion, absolute mass and high-altitude winds of exoplanet HD 209458b, *Nature*, 465: 1049-51, 2010.
- Sousa-Silva, C., N. Hesketh, S. N. Yurchenko, C. Hill, and J. Tennyson, High temperature partition functions and thermodynamic data for ammonia and phosphine, *J. Quant. Radiat. Trans.*, 142: 66-74, 2014.
- Steffen, W., P. J. Crutzen, and J. R. McNeill, The Anthropocene: Are Humans Now Overwhelming the Great Forces of Nature, *AMBIO: J. Hum. Environ.*, 36: 614-21, 2007.
- Strobel, D. F., Aeronomy of the major planets: Photochemistry of ammonia and hydrocarbons, *Reviews of Geophysics*, 13: 372-82, 1975.
- Sung, K., G. C. Toon, A. W. Mantz, and M. A. H. Smith, FT-IR measurements of cold C₃H₈ cross sections at 7–15 μ m for Titan atmosphere, *Icarus*, 226: 1499-513, 2013.

- Swain, M. R., G. Tinetti, G. Vasisht, P. Deroo, C. Griffith, J. Bouwman, Pin Chen, Y. Yung, A. Burrows, L. R. Brown, J. Matthews, J. F. Rowe, R. Kuschnig, and D. Angerhausen. 2009. Water, Methane, and Carbon Dioxide Present in the Dayside Spectrum of the Exoplanet HD 209458b, *Astrophys. J.*, 704: 1616.
- Swain, M. R., G. Vasisht, G. Tinetti, J. Bouwman, Pin Chen, Y. Yung, D. Deming, and P. Deroo, Molecular Signatures in the Near-Infrared Dayside Spectrum of HD 189733b, *Astrophys. J. Letters*, 690: L114, 2009.
- Swain, M. R., G. Vasisht, and G. Tinetti, The presence of methane in the atmosphere of an extrasolar planet, *Nature*, 452: 329-31, 2008.
- Tarasova, O. A., C. A. M. Brenninkmeijer, S. S. Assonov, N. F. Elansky, T. Röckmann, and M. A. Sofiev, Atmospheric CO along the Trans-Siberian Railroad and River Ob: source identification using isotope analysis, *J. Atmos. Chem.*, 57: 135-52, 2007.
- Terezchuk, K. A., D. P. Moore, J. J. Harrison, C. D. Boone, M. Park, J. J. Remedios, W. J. Randel, and P. F. Bernath, Observations of peroxyacetyl nitrate (PAN) in the upper troposphere by the Atmospheric Chemistry Experiment-Fourier Transform Spectrometer (ACE-FTS), *Atmos. Chem. Phys.*, 13: 5601-13, 2013.
- Thiemens, H., T. L. Jackson, and A. M. Brenninkmeijer, Observation of a mass independent oxygen isotopic composition in terrestrial stratospheric CO₂, the link to ozone chemistry, and the possible occurrence in the Martian atmosphere, *Geophys. Res. Lett.*, 22: 255-57, 1995.
- Thiemens, M. H., T. Jackson, E. C. Zipf, P. W. Erdman, and C. van Egmond, Carbon Dioxide and Oxygen Isotope Anomalies in the Mesosphere and Stratosphere, *Science*, 270: 969, 1995.
- Thommes, E. W., M. J. Duncan, and H. F. Levison, The Formation of Uranus and Neptune among Jupiter and Saturn, *Astron. J.*, 123: 2862, 2002.
- Tokunaga, A. T., A. Storrs, S. C. Beck, E. Serabyn, and E. E. Bloemhof, The Detection of C₃H₈ (Propane) on Jupiter. *Bull. Americ. Astron. Soc.*, 15: 832, 1983.
- Velazco, V., S. W. Wood, M. Sinnhuber, I. Kramer, N. B. Jones, Y. Kasai, J. Notholt, T. Warneke, T. Blumenstock, F. Hase, F. J. Murcray, and O. Schrems, Annual variation of strato-mesospheric carbon monoxide measured by ground-based Fourier transform infrared spectrometry, *Atmos. Chem. Phys.*, 7: 1305-12, 2007.

- Venot, O., E. Hébrard, M. Agúndez, M. Dobrijevic, F. Selsis, F. Hersant, N. Iro, and R. Bounaceur, A chemical model for the atmosphere of hot Jupiters, *Astron. & Astrophys.*, 546: A43, 2012.
- Venot, O., E. Hébrard, M. Agúndez, L. Decin, and R. Bounaceur, New chemical scheme for studying carbon-rich exoplanet atmospheres, *Astron. & Astrophys.*, 577: A33, 2015.
- Verronen, P. T., M. E. Andersson, D. R. Marsh, T. Kovács, and J. M. C. Plane, WACCM-D Whole Atmosphere Community Climate Model with D-region ion chemistry, *J. Adv. Model. Earth Sys.*, 8: 954-75, 2016.
- Vigouroux, C., F. Hendrick, T. Stavrakou, B. Dils, I. De Smedt, C. Hermans, A. Merlaud, F. Scolas, C. Senten, G. Vanhaelewyn, S. Fally, M. Carleer, J. M. Metzger, J. F. Müller, M. Van Roozendael, and M. De Mazière, Ground-based FTIR and MAX-DOAS observations of formaldehyde at Réunion Island and comparisons with satellite and model data, *Atmos. Chem. Phys.*, 9: 9523-44, 2009.
- von Bobruzki, K., C. F. Braban, D. Famulari, S. K. Jones, T. Blackall, T. E. L. Smith, M. Blom, H. Coe, M. Gallagher, M. Ghalaieny, M. R. McGillen, C. J. Percival, J. D. Whitehead, R. Ellis, J. Murphy, A. Mohacsi, A. Pogany, H. Junninen, S. Rantanen, M. A. Sutton, and E. Nemitz, Field inter-comparison of eleven atmospheric ammonia measurement techniques, *Atmos. Meas. Tech.*, 3: 91-112, 2010.
- Walkty, I., and K. Kohut, SCISAT-1 Spacecraft. in P. Bernath (ed.), *The Atmospheric Chemistry Experiment ACE at 10: A Solar Occultation Anthology* (A. Deepak Publishing: Hampton, VA), 2013.
- Wang, Z., J. Chappellaz, P. Martinerie, K. Park, V. Petrenko, E. Witrant, L. K. Emmons, T. Blunier, C. A. M. Brenninkmeijer, and J. E. Mak, The isotopic record of Northern Hemisphere atmospheric carbon monoxide since 1950: implications for the CO budget, *Atmos. Chem. Phys.*, 12: 4365-77, 2012.
- Waymark, C. K. Walker, C. D. Boone, E. Dupuy, and P. F. Bernath, "Validation of the ACE-FTS Version 3.0 Dataset Against Other Satellite Instrument Datasets." In *Imag. Appl. Opt.*, FMB4. Toronto: Optical Society of America, 2011.
- Weidenschilling, S. J., and J. S. Lewis, Atmospheric and cloud structures of the Jovian planets, *Icarus*, 20: 465-76, 1973.

- Weiss, L. M. and G. W. Marcy, The Mass-Radius Relation for 65 Exoplanets Smaller than 4 Earth Radii, *Astrophys. J. Letters*, 783: L6, 2014.
- Wildt, R., Ultrarote Absorptionsbande in den Spektren der Grossen Planeten, *Naturwissenschaften*, 19: 109-10, 1931.
- Yoshino, K., J. R. Esmond, Y. Sun, W. H. Parkinson, K. Ito, and T. Matsui, Absorption cross section measurements of carbon dioxide in the wavelength region 118.7–175.5 nm and the temperature dependence, *J. Quant. Radiat. Trans.*, 55: 53-60, 1996.
- Yurchenko, S. N., R. J. Barber, and J. Tennyson, A variationally computed line list for hot NH₃, *Month. Not. Royal Astron. Soc.*, 413: 1828-34, 2011.

VITA

CHRISTOPHER ANDREW BEALE

Department of Ocean, Earth & Atmospheric Sciences
406 Oceanography & Physical Sciences Building
Norfolk, VA 23529

EDUCATION

Ph.D. in Oceanography – Old Dominion University, 2011-2017

M.Sc. in Physics (by research) – The University of York, UK. Graduation date, January 20th
2012

B.Sc. in Physics with Astrophysics – The University of York, UK. Graduation date, July 14th
2010

EMPLOYMENT

Aug 2013-May 2017, Graduate Research Assistant, Department of Chemistry & Biochemistry,
Old Dominion University, Norfolk, VA.

Aug 2011-Aug 2013, Graduate Teaching Assistant, Department of Chemistry & Biochemistry,
Old Dominion University, Norfolk, VA.

SELECT PUBLICATIONS

Beale, C. A., E. M. Buzan, C. D. Boone, and P. F. Bernath. 2016a. Near-global distribution of
CO isotopic fractionation in the Earth's atmosphere, *J. Mol. Spectrosc.*, 323: 59-66.

Beale, C.A., R.J. Hargreaves, and P.F. Bernath. 2016b. Temperature-dependent high resolution
absorption cross sections of propane, *J. Quant. Radiat. Trans.*, 182: 219-24.

Beale, C.A., R.J. Hargreaves, P. Coles, J. Tennyson, and P.F. Bernath. Infrared absorption
spectra of hot ammonia, *J. Quant. Radiat. Trans.*, in press.